ARISTOTLE UNIVERSITY OF THESSALONIKI
POLYTECHNIC UNIVERSITY
MECHANICAL ENGINEERING DEPARTMENT
MACHINE DYNAMICS LABORATORY

DIPLOMA THESIS

AEROELASTIC ANALYSIS OF A TURBOPROP AIRCRAFT PROPELLER AND STABILITY ANALYSIS FOR THE «WHIRL FLUTTER» AEROELASTIC PHENOMENON

DIOGENIS TSICHLAKIS

STUDENT ID: 6216

Supervisor : PROFESSOR NATSIAVAS SOTIRIOS

Thessaloniki, September 2022

The word "scientist" comes from the verb "επίσταμαι" (ἐπ- + ἵσταμαι), which means "to know well," "to understand with certainty." As engineering scientists, we are obligated to deeply understand the fundamental laws of nature and, building upon them, to genuinely solve real physical problems.

Unknown X.

Abstract

This thesis aims to analyze the aeroelasticity of a turboprop propeller and the parametric study of the propeller's stability with respect to the dynamic aeroelastic phenomenon "Whirl Flutter". Specifically, in chapter two, after designing the three-dimensional model of the propeller, the important loads and phenomena that develop during operation are described and are also the ones that we will study in the rest of the analysis.

Having presented the basic concepts and characteristics of turboprop propellers, we proceed to the third chapter where the fluid mechanics problem is solved in order to calculate the force and moment responses and the pressure distribution for the propeller. These loads are analyzed in the frequency domain by applying "Fourier analysis" and the significant influence of the harmonic components for the structure's stress are observed.

After presenting the basic concepts concerning the fluid-mechanical nature of the problem, the elasticity of the structure is introduced. The aeroelastic problem is solved in chapter four and the influence of the operating conditions (rotation and flight speed) on the characteristics of the physical eigenmodes/eigenfrequencies are observed. Furthermore, the different orders of magnitude of the deformations, stresses, and displacements of the structure in the different directions are observed and the internal damping is introduced in the system due to the aerodynamic loads, which end up acting as a periodic excitation force in the steady state. At the end of chapter four, a comparison is made between the amplitudes of oscillation of the harmonic components of the forces and moments which have been calculated by the fluid mechanics problem in chapter three and those that have been calculated in the analysis of chapter four. The different distributions of the pressure coefficient for the same cross sections between the two problems are also compared.

In the last part of this thesis, the model is modified and the stability limits for the gyroscopic phenomenon "Whirl Flutter" is studied. This phenomenon occurs when the engines support on the wing is considered elastic. More specifically, the system equations are carried out using Lagrange's equations, where the aerodynamic loads are calculated based on the "Strip Theory". Applying then the method of eigenmodes gives us the stability and instability regions (Whirl Flutter, Static Divergence). By altering then different parameters the stability diagrams are obtained. In addition, we present the propeller hub's response diagrams, when the propeller operates in stability region, neutral stability, "Whirl Flutter" instability and "Static Divergence" instability.

In this thesis, the model was design with the use of the computer aided design (CAD) software "Inventor", provided by Autodesk. The fluid-mechanical and aeroelastic simulations were carried out with the use of Fluent and Mechanical by ANSYS. The study of the stability phenomenon was carried out using independent code created in Matlab.

Table of Contents

Abstract iii

1. INTRODUCTION 1

1.1 Interaction Between Fluid and Structure 1

1.2 Aeroelastic Phenomena 2

1.3 Purpose of the Thesis and Chapter Contents 5

2. DESIGN AND PRINCIPLES OF PROPELLER OPERATION 7

2.1 Propeller and Design Criteria 7

2.1.1 Interpretation of Aircraft Propeller 7

2.1.2 Design Criteria 7

2.2 Design of the Propeller 8

2.3 Operation and Developed Forces on the Propeller 11

2.3.1 Basic Loads and Geometric Parameters 11

2.3.2 Secondary Phenomena – Harmonic Loads 14

3. FLUID MECHANICS PROPELLER ANALYSIS 21

3.1 Formulation of Equations and Numerical Methods 21

3.1.1 Formulation of Equations URANS 21

3.1.2 Turbulence Model SST k -ω 28

3.1.3 Numerical Solution Methodology 29

3.2 Fourier Transform and Signal Analysis 33

3.2.1 Fourier Transform 33

3.2.2 Discrete Fourier Transform and FFT 34

3.3 Introduction to Software and Discretization 35

3.3.1 Grid Independence and Quality check 37

3.4 CFD Solution results 38

3.4.1 Comparison Experimental – Computational Results 38

3.4.2 Simulation Conditions 40

3.4.3 Load response and Spectral analysis 42

3.4.4 Pressure Distribution 45

4. AEROELASTIC ANALYSIS OF THE PROPELLER 47

4.1 Description of the Problem and Deformable Bodies 47

4.2 Aeroelasticity 48

4.3 Rotational Beam 51

4.3.1 Campbell Diagram 57
4.4 Formulation of equations 57
4.4.1 Three-dimensional elasticity theory for Rotating Structures 58
4.4.2 Propeller's Equations 61
4.4.3 Fluid Equations 65
4.5 Numerical Methods and Co – Simulation 66
4.6 Discretization 69
4.7 Results 71
4.7.1 Modal Analysis and Campbell diagram 71
4.7.2 Load response and Fourier analysis 73
4.7.3 Structural Response 76
4.8 Comparison FSI – CFD 79
5. PPARAMETRIC STABILITY ANALYSIS - WHIRL FLUTTER 82
5.1 Gyroscopic Phenomena and Analytical Dynamics 82
5.2 Whirl Flutter and excited loads 87
5.2.1 Whirl Flutter Phenomenon 87
5.2.2 Propeller's loads analysis 90
5.3 Formulation of the system's equations 91
5.3.1 Equations of Motion – Lagrange 91
5.3.2 Aerodynamic loads - Strip Theory 94
5.4 Solution – Non-symmetric Matrices 102
5.5 Results 106
6. CONCLUSIONS 114
BIBLIOGRAPHY 116

1. INTRODUCTION

In the introductory chapter, an overview of the scientific fields we will work on is presented in this thesis. Initially, the definitions and concepts of the field of aeroelasticity and instability phenomena are concisely presented, along with historical references. Subsequently, we mention the elements of each chapter, which will be presented in the main body of the thesis.

1.1 Interaction Between Fluid and Structure

Throughout history, curiosity and the need for achieving higher goals, inherent in us as humans, have driven us towards progress and today's accomplishments. Apart from searching for new technologies and means, a significant part of the scientific community is engaged in optimizing those we already possess. Therefore, we are in a constant search for more accurate processes capable of accurately modeling our physical problems.

One extensive family of systems that has garnered considerable interest from the scientific community in recent years is the Fluid-Structure Interaction (FSI) systems. By studying an FSI system, we find the separate subsystems of the structure and the fluid coupled into a complex problem. As a result, the solution of the former is influenced by the solution of the latter, leading to the incorporation of the dual nature of the studied system (fluid-structure) into a common problem. Figure 1.1 illustrates some typical applications in which the interaction between the fluid and the structure is crucial for approaching reality. As engineers, our goal is to understand the behavior and phenomena that develop in such systems, either to avoid phenomena like flutter and instability or to exploit them (e.g., energy harvesting from FSI systems).

A subdivision of this family of systems, when the fluid involved is air, involves aeroelastic problems. Aeroelasticity is a relatively new branch of applied mechanics that studies the interaction between air (fluid) and the structure. Specifically, it deals with the interaction of aerodynamic, elastic, and inertial forces. In simpler terms, when an increase in aerodynamic loads affects the structure in such a way that the structure, in turn, increases the aerodynamic loads acting on it, then we have an aeroelastic problem. The exchange of information between these two subsystems proves significant and ultimately needs to be considered for accurate modeling.

In their broader scope today, aeroelastic studies focus on aircraft due to their more intense interaction, leading to higher loads. However, these studies also find applications in terrestrial and marine structures (skyscrapers, cars, watercraft, etc.).

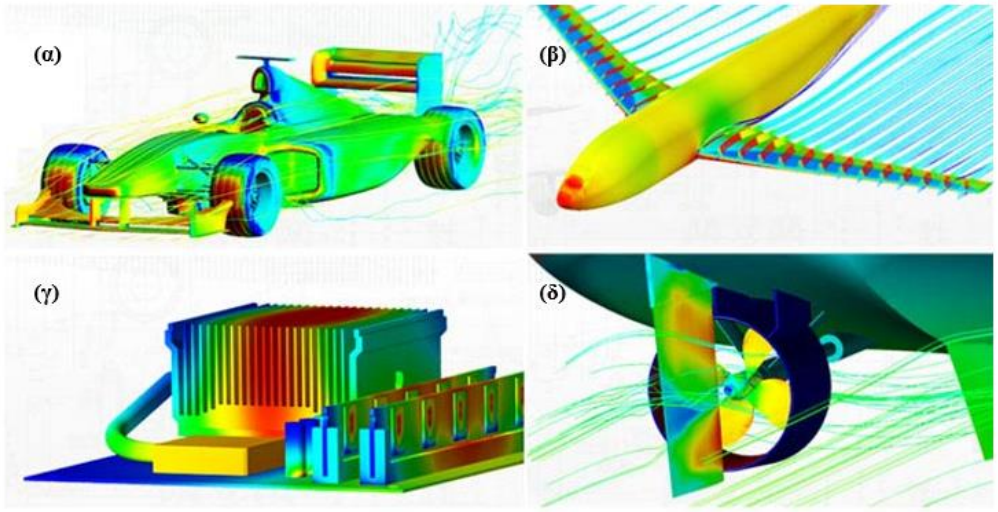

Figure 1. 1. Systems FSI (a) Racing car (b) Aircraft (c) Microchip cooling (d) Propeller of a marine vessel

The science of aeroelasticity, we could say, is an improvement in the accuracy of the solution, as it brings the analysis methods closer to the real problem by introducing the interaction between the two. The theory and physics behind the problem were well-known long before they found application in real systems since the available computational resources at the beginning of the aeroelasticity field were not sufficient to provide adequate results for realistic models. With the evolution of the means we have at our disposal now (computers) and the continuous expansion of knowledge and methodologies in the separate subsystems (fluid-structure), our obligation as engineers is to construct more efficient and safer systems, relying on fundamental physical principles and utilizing new technologies.

A comprehensive description and analysis of the different fields that converge in aeroelastic studies are carried out in the 4th chapter, where their application is also demonstrated.

1.2 Aeroelastic Phenomena

The main objective in the application of aeroelastic analysis is to determine the phenomena resulting from the interaction of the two systems. Most catastrophic accidents observed in aircraft are attributed to such phenomena. Aeroelastic phenomena can be classified into static and dynamic aeroelastic phenomena, depending on the characteristics that interact between the two subsystems. For example, in static aeroelastic phenomena, we have an interaction between non-transient aerodynamic loads and the elastic properties of the structure, while in dynamic phenomena, inertial properties also come into play.

Aeroelasticity constitutes a significant part of the history of aircraft. The Wright brothers in 1903, for the aircraft Wright Flyer depicted in Figure 1.2a, managed to fly the aircraft after solving the problem of lateral control, which is considered their greatest achievement and the first powered flight in aviation history. In reality, slightly earlier in 1903, Samuel Langley attempted to fly his airplane (Figure 1.2b) twice, launching it from the top of a houseboat. Due to significant elasticity

and loads on the wings and their interaction, this led to the failure of the airplane. The destruction of this aircraft is considered the first aeroelastic phenomenon with catastrophic consequences.

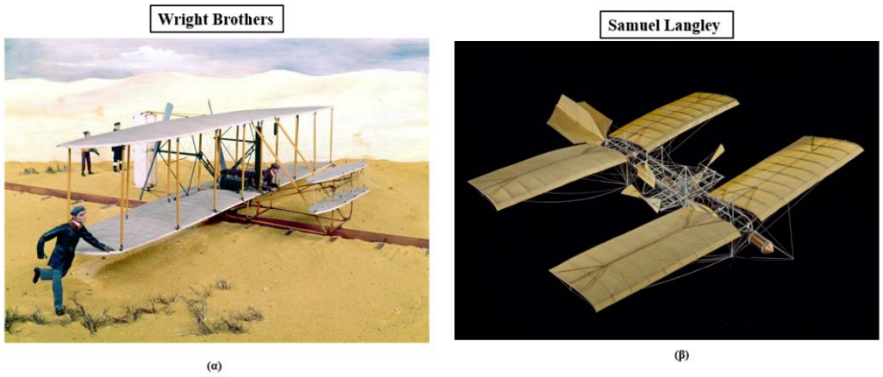

Figure 1. 2. Powered aircraft (a) Wright brothers and (b) Samuel Langley.

Until the time of writing this specific work, the most significant mapped static and dynamic aeroelastic phenomena observed in aircraft are presented in Table 1.1. It is emphasized that the phenomena listed in the table refer to the current time, as historically proven, these phenomena unfortunately become known and analyzed only after some construction failure occurs due to them. The first complete recording of the appearance of an aeroelastic phenomenon, specifically flutter with destructive character, was in 1916 for the bomber aircraft "Handley Page O/400." Violent oscillations occurred in the tail of the aircraft due to lack of stability in the power transmission elements. Nevertheless, designing with the aim of smoothing out and avoiding aeroelastic phenomena became a necessary precondition for certifying aircraft during World War I and remains an essential part of the design phase for new constructions until today.

Table 1. 1. Aeroelastic Phenomena

Στατικά αεροελαστικά φαινόμενα	Δυναμικά αεροελαστικά φαινόμενα
Torsional Divergence	Flutter
Control surface reversion	Buffeting
Static Equlibrium for deformable aircraft	Aeroelastic response on dynamic loading
	Maneuvrability and dynamic equlibrium
	Aero -servoelasticity

Among the above, the dominant phenomenon affecting the structural integrity has been proven to be flutter, compared to the others. A variation of this phenomenon, which occurs in aircraft propellers, is known as whirl flutter (WF), and in this study, a parametric analysis is conducted to find the stability boundaries of the structure. WF, also known as gyroscopic flutter, is a dynamic aeroelastic stability phenomenon that can occur due to the elastic interaction between the engine and propeller in aircraft. Such a system is depicted in Figure 1.3a. Because of the additional degrees of freedom introduced by the elastic coupling and the gyroscopic effect caused by the large rotating masses of the propellers, there is a coupling of the independent modes of the system, leading to complex responses of the structure. If this motion cannot be damped out by structural or aerodynamic damping, the system enters an unstable state, resulting in structural failure. Figure 1.3b shows various forms of structural failure due to WF. In this figure, the Beechcraft 1900C aircraft is depicted. A comprehensive analysis and detailed formulation of equations for WF and the phenomena affecting it will be carried out in Chapter 5.

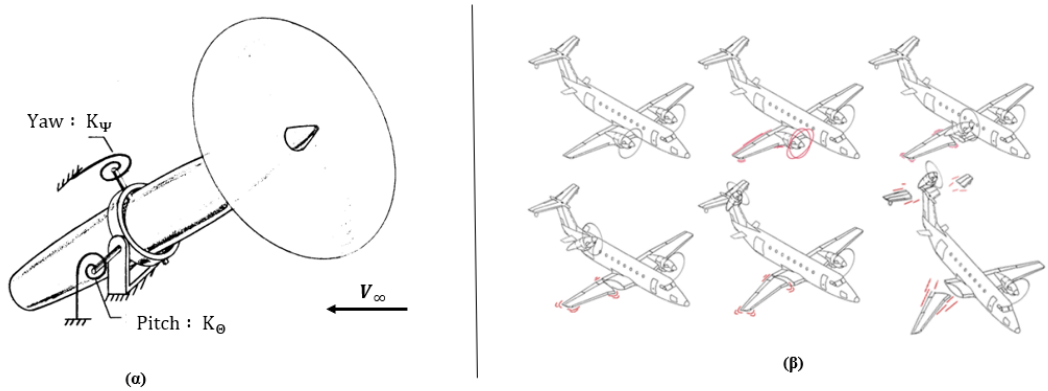

Figure 1.3. (a) Propeller-engine system with elastic coupling in 2 directions (Yaw ψ - Pitch θ). (b) Types of failure due to Whirl Flutter.

The scientific community showed practical interest in this phenomenon following two fatal accidents of Lockheed L-188 C Electra II passenger aircraft (Figure 1.4a) in 1959 and 1960. To investigate the cause of these accidents, experiments were conducted in the NASA Langley transonic wind tunnel. The results of the experiments revealed that the accidents were caused by the high rotational speeds of the propeller and the large oscillations, in the form of elliptical motion, induced by the propeller on the wing in combination with the loose coupling of the engine. This led to the detachment of the wing from the main body of the aircraft. Despite the mapping and study of the Whirl Flutter phenomenon, more aircraft were led to destruction in the following years due to this issue, such as the Beechcraft 1900C passenger aircraft (Figure 1.4b) in 1991 and the Grumman Turbo Mallard GF73T passenger aircraft (Figure 1.4c) in 2005. A more detailed presentation of the destruction of the aforementioned aircraft due to Whirl Flutter can be found in reference [9]. The uncertainty regarding the aeroelastic behavior exhibited by structures and the consequences it may have on their integrity highlights the complexity and significance of the of aeroelasticity field.

Figure 1.4. Passenger aircraft: (a) Lockheed L-188 C Electra I, (b) Beechcraft 1900C, (c) Grumman Turbo Mallard GF73T.

Elliptical whirl flutter can specifically occur in turboprop aircraft, helicopters, and aircraft with tilt-rotors (tilt-rotor aircraft). Among these three different systems where whirl flutter may arise, we will focus on turboprop aircraft (Figure 1.4), as the other two involve exceptional complexity (elasticity, complex rotational field) and significant computational challenges, which go beyond the scope of this thesis.

1.3 Purpose of the Thesis and Chapter Contents

In this thesis, an aeroelastic analysis is conducted on the turboprop aircraft propeller, and a parametric study of the propeller-engine system is performed to find the stability boundaries of the Whirl Flutter phenomenon. Our aim is to observe and interpret all the complex phenomena that occur in systems like ours using theoretical tools and professional software, rather than finding solutions for specific problems (e.g., designing a more efficient propeller or increasing safety factors in operating ranges). The work presented in this thesis constitutes a comprehensive problem. We begin with the design of the propeller, using real geometric dimensions for the blades, which are specific to turboprop propeller-engine systems. We present the design criteria, the operational mode, and the significant dynamic loads that develop during operation due to interaction with the air, and these loads are the main sources of stress on the structure.

In Chapter 2, the fluid mechanics problem for the rotating propeller is solved. Specifically, we first formulate the URANS (Unsteady Reynolds-Averaged Navier-Stokes) equations for the rotational field and present the solution methodologies for these equations. Next, we introduce the Fourier transformation and the Fast Fourier Transform (FFT) algorithm. FFT is a mathematical tool that we will later use to analyze our results. We then define and discretize the computational domain, and the solution is compared with experimental results for model validation. Chapter 3 is concluded by presenting the response diagrams of forces and moments acting on the hub and the distribution of the pressure coefficient on the propeller for different simulation sets. Furthermore, the content of forces and moments applied to the propeller is presented in the frequency domain. We dedicate a whole chapter to solving the fluid mechanics problem without referring to the structure to gradually introduce the complex aeroelastic model of the next chapter for better understanding.

In Chapter 4, we introduce the deformability of the propeller and solve the aeroelastic interaction problem between the propeller and the fluid. Initially, we present the concepts of deformability and aeroelasticity. Then, we formulate the equations for a rotating beam to understand the forces governing such problems and their contribution to the final structural matrices. The rotating beam can be considered as a simplification of the propeller, replacing each blade with a beam. Additionally, we discuss the use and significance of the Campbell diagram, which we will construct for our system in the results. After presenting the fundamental theoretical concepts, we proceed to formulate the equations for the entire structure since the equations governing the rotational field remain the same as in Chapter 3. For the propeller, we establish the three-dimensional theory of elasticity for a rotating infinitesimal element and formulate the motion and elasticity equations relating displacements, rotations, and strains. The overall matrices for the entire structure are generated using the Galerkin method and shape functions for three-dimensional finite elements (FEM). We continue by presenting the principles of co-simulation and the Gauss-Seidel algorithm, which we will use to exchange information between subsystems. Additionally, we present the numerical methods used to solve the equations of the propeller. In the final part of the chapter, we discretize the propeller and initially present the results of the solution, later comparing them with the solutions from the fluid mechanics analysis in Chapter 3.

In Chapter 5, the last chapter of the thesis, we perform the parametric study of the stability boundaries for the "Whirl Flutter" phenomenon. For our model in this chapter, we maintain the propeller we designed and simulate the other engine components as a compact solid cylinder, with the possibility of adjusting its length. Initially, we present the theoretical aspects of gyroscopic phenomena, which will be necessary to interpret the Whirl Flutter phenomenon. Subsequently, we thoroughly analyze the Whirl Flutter phenomenon and formulate the system's equations in detail. For the equation formulation, we use the Lagrange equations, while the extraction of the equations for the aerodynamic loads is performed using the Strip Theory. In the final part of the theory, we present the process of solving the non-symmetric matrices that arise for calculating the stability boundaries and the system's response. We conclude with presenting diagrams for the stability boundaries under various parameter changes, as well as diagrams showing the hub's trajectory in the regions of stability, boundary stability, instability, and static divergence.

For this thesis, the Inventor software by Autodesk was used for propeller design. The solution of the rotational field, the construction of the structural model, and their co-simulation were performed using ANSYS software, specifically Fluent, Mechanical, and Workbench, respectively. For the last chapter, the solution of the analytical equations of the system was achieved using custom code in the Matlab programming language.

2. DESIGN AND PRINCIPLES OF PROPELLER OPERATION

In this chapter, we perform the design of our model based on the constraints and requirements that must be met for systems like ours. As mentioned in the previous section, for this particular thesis, our model consists of a propeller used in aircraft equipped with turboprop engines. We first present the design of the propeller and the objectives we aim to achieve. Then, we delve into the operational principles and the key parameters that will be of interest to us.

The propeller design process involves determining the optimal dimensions, blade shape, and other relevant factors to ensure efficient performance and meet the specific requirements of the aircraft. We use the Autodesk Inventor software to create the propeller designs.

The primary goal of this chapter is to develop a well-designed propeller model that fulfills the necessary criteria for a turboprop aircraft, taking into account factors like thrust generation, aerodynamic efficiency, and structural integrity.

By employing the appropriate design principles and software tools, we aim to create a propeller that not only provides the required performance characteristics but also ensures safety and reliability during its operation in turboprop aircraft.

2.1 Propeller and Design Criteria

2.1.1 Interpretation of Aircraft Propeller

The propeller is a device that converts mechanical energy into thrust, which is responsible for the movement of the vehicle it is attached to. It consists of one or more aerodynamic surfaces known as blades. Each blade of a propeller operates like a rotating wing of an aircraft, generating forces on its cross-sections due to its shape. The cross-sectional shapes of the blades are composed of airfoils, and as a result, the rotating propellers produce a combined thrust and torque, overcoming the resistance of the vehicle and propelling it forward. Propellers are the most commonly used means of thrust generation for general aviation aircraft today.

Propellers provide a highly efficient way to produce thrust by accelerating a mass of air. Generally, the greater the acceleration, the more chemical energy (fuel) needs to be converted into mechanical energy by the engine. Therefore, propeller-driven thrust consumes much less fuel compared to other methods, making it the most fuel-efficient means of generating thrust. Additionally, the design and maintenance of propellers have lower costs compared to jet engines. For this reason, in low-cost aircraft, propellers are the optimal choice. For more detailed information on the design and operation of propellers, please refer to the referenced document **Σφάλμα! Το αρχείο προέλευσης της αναφοράς δεν βρέθηκε.**.

2.1.2 Design Criteria

Before proceeding with the design, we need to define the constraints and objectives for the propeller. The propeller to be incorporated into our model must satisfy certain essential criteria

used in real aviation applications and meet the requirements to observe all the phenomena studied in this thesis.

The propeller blades are connected to a central hub, which in turn is attached to the engine's reduction gearbox. As the propeller utilizes the geometry of its sections to generate forces, we understand that the design and characteristics of the propeller significantly affect the generated loads and, consequently, the phenomena that occur during its operation. The complete analysis of all the forces developed in the propeller will be conducted during the description of its operation later on.

Our goal in this thesis is to monitor the interaction of the structure with the fluid and analyze aeroelastic instability phenomena. Therefore, we aim to design a propeller that fulfills all the basic requirements applicable to real-world scenarios and consider the characteristics necessary for our model to produce distinct results for the studied phenomena.

Additionally, since computational fluid dynamics (CFD) results require experimental verification (wind tunnel tests), we need to design a propeller with geometric characteristics similar to an experimentally validated propeller. This will enable us to use dimensionless coefficients to validate our computational model.

Thus, we conclude that we need a large-scale construction that provides us with distinct data on variations during interaction with the fluid. Moreover, the geometric dimensions of this propeller should be obtained from an experimentally validated model with available test results.

2.2 Design of the Propeller

After communicating with the authors of reference [14], they provided us with the diagrams of the geometric dimensions presented in Figure 2.1. These values refer to a propeller designed for use in high altitudes (stratosphere) and intended for the KFG-series airship. The publication also includes results obtained from experiments conducted on the propeller in a wind tunnel, which will be used to validate our computational model in the next chapter.

The parameters depicted in the diagram are as follows:

R: Propeller Blade Radius

r: Distance of section from the hub

D: Total Propeller Diameter

b: Airfoil Chord

h: Airfoil Thickness at the corresponding section

p: Airfoil Pitch Angle

These geometric dimensions are represented in the two-dimensional drawing of an airfoil in Figure 2.2. For this particular propeller, the root section of the blade features a Clark Y 11.7% airfoil, and the tip section has an R.A.F 6 airfoil.

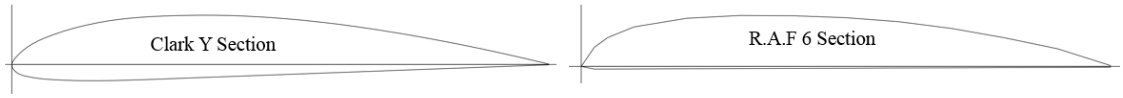

The percentage 11.7 refers to the ratio of the maximum thickness to the chord length of the airfoil. These two types of airfoils, the Clark Y 11.7% and the R.A.F 6, are the basic ones used in aircraft propellers up to the present day.

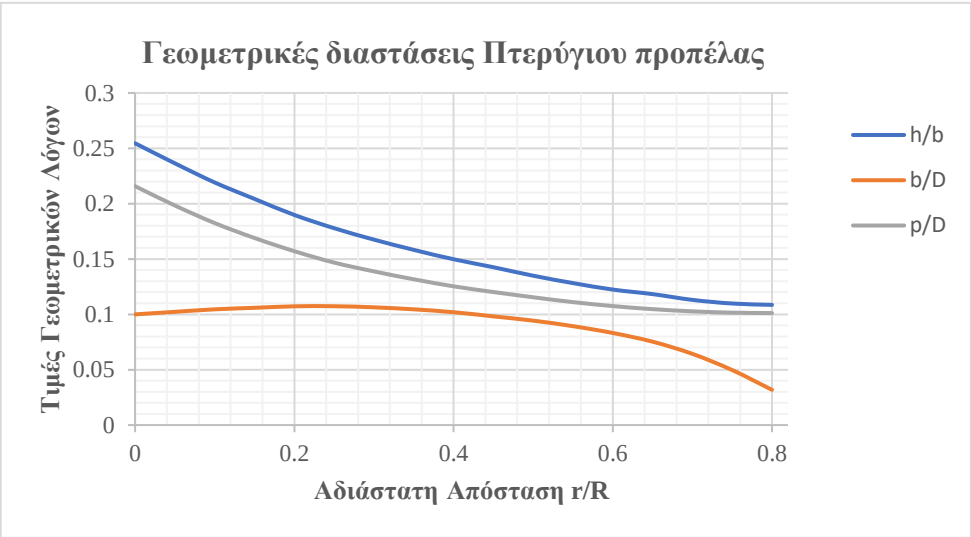

Figure 2.1. The geometric dimensions along the length of the propeller blade.

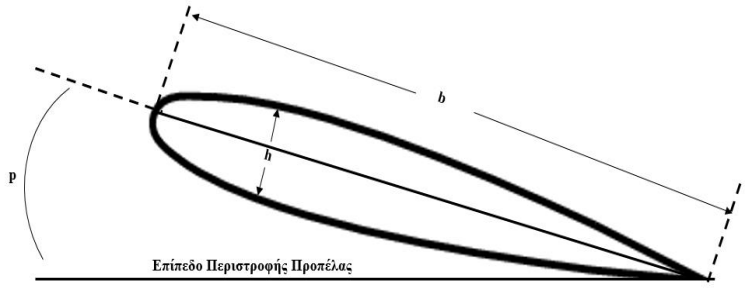

Figure 2.2. Characteristics of the airfoil.

In Figure 2.1, we observe that the pitch angle varies for each section of the propeller blade, resulting in a helical shape of the blade from the root to the tip. This helical shape is characteristic of aircraft propellers. It is due to the fact that, during the rotation of the propeller, the sections farther from the hub move faster than the sections closer to the hub. If the propeller had the same pitch angle for all sections, at high flight speeds (high RPM), we would have negative pitch angles for the sections near the hub, due to distortion and relative angle of attack of the propeller. This would lead to significant differences in forces on different sections or even loss of support at the tips of the blades. The different pitch angles result in approximately the same relative velocity for the different

sections of the blade, and as a result, the distribution of loads on the blades approaches a more uniform distribution.

One important aspect to consider is the selection of the overall diameter for the propeller. Depending on the conditions we choose to simulate in our model (aircraft speed, rotational speed of the propeller), the diameter of the propeller should be such that it does not create regions at the blade tips with supersonic speeds. For this reason, and due to the simulation conditions that we will use in the subsequent chapters of the analysis, we choose a total propeller diameter of 2.2 meters. This dimension is sufficient to provide satisfactory gyroscopic loads for observing the instability phenomena we are interested in, within reasonable operating ranges.

We decide to use a propeller with 2 blades. In Figure 2.3, a two-dimensional diagram of the propeller is presented along with some basic dimensions. Additionally, in the same diagram, we can distinguish the four cross-sections along the length of the propeller blade, where we can see the different characteristics (pitch angle, thickness, etc.) of the airfoil sections. We observe that a spherical shape is given to the hub from the leading edge side facing the airflow, in order to minimize the resistance introduced by the flow field.

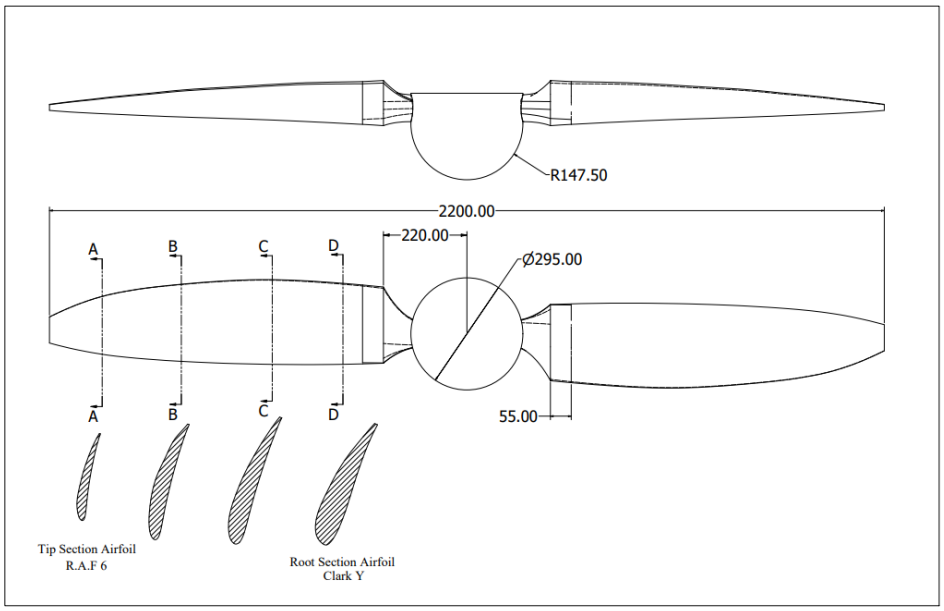

Figure 2.3. Two-dimensional diagram of the propeller and basic dimensions.

For our propeller, we choose aluminum alloy as the material, which is the most commonly used material in the industry for propeller construction. It is considered a good choice due to its low weight, high strength-to-weight ratio, and low cost. However, with the advancement of analysis methods, propellers are now also constructed from composite materials, allowing us to tailor specific properties to certain regions and directions while maintaining desirable mechanical properties and low manufacturing costs. The mechanical properties of the chosen aluminum alloy are presented in Table 2.1.

Using this material, the total weight of the propeller is calculated as $m_p = 58.581\ kg$ through the design software Inventor. Figure 2.4 depicts the three-dimensional model of our propeller. With the complete design of the propeller and its defined characteristics, we proceed with the description of its operation.

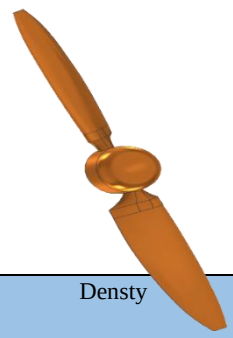

Figure 2.4. 3D Propeller's design in Inventor enviroment

Table 2. 1 Mechanical Properties for aluminum alloy

Densty	$\rho = 2770 \left[\frac{kg}{m^3}\right]$
Young 's Modulus	$E = 71\ [GPa]$
Poisson's Ratio	$\nu = 0.33$
yield strength	$\sigma_\delta = 280 \left[\frac{N}{mm^2}\right]$
maximum tensile strength	$\sigma_o = 310 \left[\frac{N}{mm^2}\right]$

2.3 Operation and Developed Forces on the Propeller

2.3.1 Basic Loads and Geometric Parameters

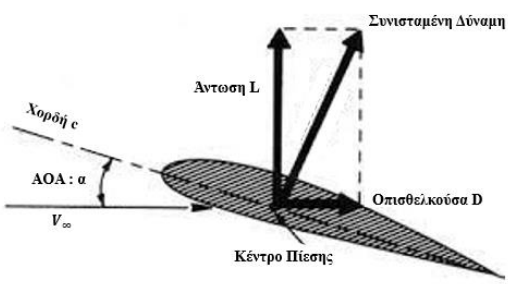

Σχήμα 2.5. Σκαρίφημα αεροτομής και βασικά μεγέθη

In this section, we describe the operation and the forces developed in the propeller. Initially, to represent the basic quantities, we start with the concept of a classic aircraft wing airfoil. In Figure 2.5, we see the cross-section of a general type of airfoil. The geometry of the airfoil results in different pressures on its upper and lower surfaces. This pressure difference creates a resultant force at the center of pressure of the airfoil. This force is divided into two components: lift (L), perpendicular to the direction of the free airflow, and drag (D), parallel to it. The main factor affecting the magnitude of these forces is the angle of attack (AOA), which is the angle formed between the direction of the free airflow and the chord of the airfoil. Additionally, the shear stresses that develop between the airfoil surface and the air within the boundary layer also have a minor contribution to these two components. The boundary layer is a very thin region on the airfoil surface characterized by high turbulence levels, high velocity variations, or even flow separation. The boundary layer is the primary difficulty in solving the flow fields, and all the continuously evolving new theories aim to

express the turbulence phenomena within it. More about the boundary layer models (turbulence models) will be presented in the next chapter.

Now specifically, the propeller, as we mentioned, can be regarded as a rotating aircraft wing with different angles of attack for its airfoils at each section. This rotational motion results in the development of forces along the length of each blade. Thus, the propeller generates, similar to a simple airfoil, lift and thrust forces at each section. However, since the directions of these forces are perpendicular and parallel to the direction of the rotational plane, respectively, it is more logical to express the resultant force in the direction perpendicular to the rotational plane (Thrust T) and parallel to the rotational plane (Torque M).

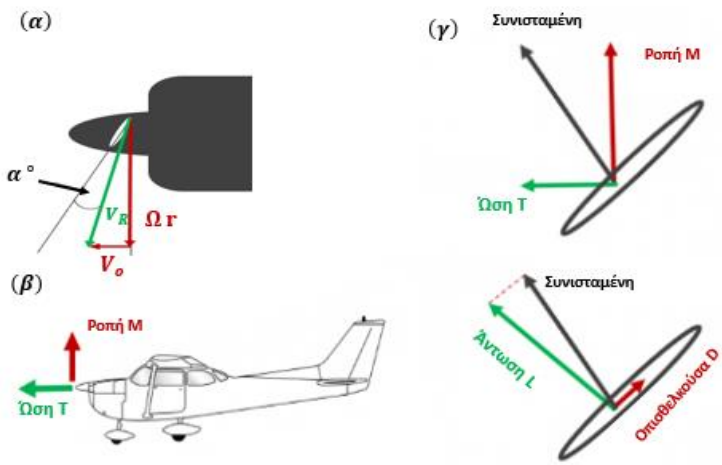

Figure 2.6(α) illustrates the velocities, (β) the forces on the propeller, and (γ) the forces at different cross-sections of the propeller blades.

By vectorially summing up these forces along the length of the propeller blades, we obtain the total Thrust and Torque of the propeller, with Thrust being the force that propels the aircraft through the air. The resulting forces are presented in Figures 2.6β and 2.6γ. Figure 2.6α illustrates the different velocities contributing to the relative resultant velocity and the angle of attack observed by an observer on the propeller blade.

In Figure 2.7, the characteristics of the airfoil of the propeller blade at a random distance from the hub (r, %R) are presented for both stationary and moving aircraft. Figure 2.7α shows the airfoil at zero flight speed, while Figure 2.7β displays it for different flight speeds. The variables and their definitions are also indicated. On the upper airfoil in the figure, the blue vector (Ωr)corresponds to the incoming flow as observed by an observer on the blade, considering the aircraft's zero airspeed. Thus, the angle of attack depends solely on the rotational speed of the propeller. However, for a non-zero aircraft speed V_o, the observer perceives a relative velocity $V_R = \sqrt{V_0^2 + (\Omega r)^2}$ which is the vector sum of the rotational speed of the propeller and the aircraft speed. The angle a_{ZL} represents the angle between the airfoil chord and the direction of zero lift for that specific airfoil. In the context of 3D bodies, measuring the angle of attack a from the a_ZL direction is more convenient because, based on this convention, when a=0°, we can infer zero lift.

The angle β represents the pitch angle of the propeller and is usually defined at 75% of the blade radius for variable-pitch propellers. For the propeller to produce forward thrust, the angle of attack between the chord and the relative airflow (V_o) must be positive. If, at any section, the angle a is less than zero, then the thrust direction is reversed for that particular section, resulting in an uneven thrust distribution along the blade. To have a positive angle of attack everywhere, an appropriate propeller pitch angle (β) must be chosen.

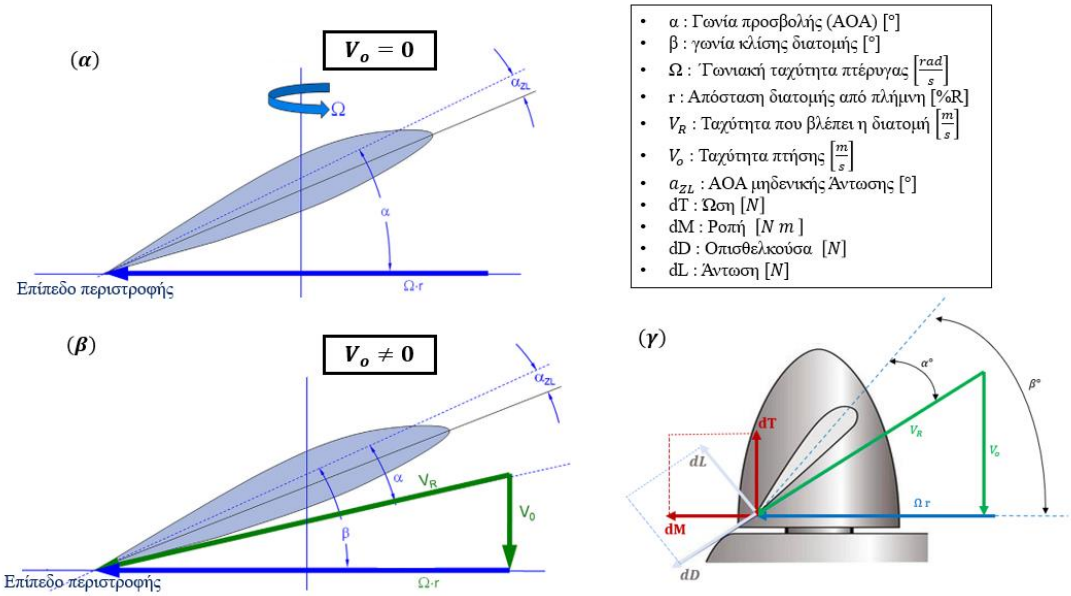

Figure 2.7 presents the geometric characteristics of the wing airfoil. In the upper image, it represents the airfoil for zero flight speed (stationary condition), while in the lower image, it represents the airfoil at a different flight speed.

In this section, we describe the method of operation and the developed forces acting on the propeller. Initially, we start with the concept of a classical aircraft wing airfoil. In Figure 2.5, a general airfoil is depicted. The geometry of the airfoil results in different pressures on its upper and lower surfaces, creating a pressure difference that generates a resultant force at the center of pressure of the airfoil. This force is resolved into components, lift (L) perpendicular to the free-stream velocity direction and drag (D) parallel to it. Another contributing factor to these components is the shear stress between the airfoil surface and the airflow, which occurs within the boundary layer. The boundary layer is a thin region on the airfoil surface characterized by high turbulence levels, velocity fluctuations, or flow separation. It serves as the transitional region between the surface of the structure and the undisturbed flow. The boundary layer represents the primary challenge in resolving the aerodynamic fields, and various theories have been developed to describe the turbulence phenomena within it. More about boundary layer models (turbulence models) will be presented in the next chapter.

Specifically, for the propeller, it can be considered as a rotating aircraft wing with different angles of attack for each cross-section. This rotational motion results in developing forces along each blade. Thus, the propeller generates lift and drag forces at each cross-section, similar to a standard airfoil. However, due to the parallel and perpendicular directions of these forces with respect to the free-stream velocity, it is more convenient to express the component perpendicular to the rotation plane as Thrust (T) and the component parallel to it as Torque (M).

By summing up these forces along the blade sections, we obtain the total Thrust and Torque of the propeller, with Thrust being the force that propels the aircraft forward through the air. The developed forces are shown in Figure 2.6(b) and 2.6(c).

In Figure 2.7, the characteristics of the airfoil on the propeller blade at different radial positions (r, %R) are presented for both stationary and moving vehicles. In Figure 2.7(a), the airfoil is depicted at zero flight speed, while in Figure 2.7(b), it is shown for a non-zero flight speed. Additionally, various variables and their definitions are provided. The blue vector (Ωr) on the upper airfoil in the figure corresponds to the incoming flow, as observed by an observer on the blade, for zero aircraft speed. Thus, the angle of attack depends solely on the propeller's rotational speed. However, for a non-zero aircraft speed V_o , the observer sees a velocity given by the vector sum of the rotational speed of the propeller and the aircraft speed $V_R = \sqrt{V_0^2 + (\Omega r)^2}$. This relative velocity is used to calculate the angle of attack a_{ZL} . For 3D bodies, it is more convenient to measure the angle of attack a with respect to a_{ZL}because, under this convention, a=0° corresponds to zero lift.

The pitch angle β represents the inclination angle of the propeller and is typically defined at 75% of the blade radius for propellers with a variable pitch β. To generate thrust from the propeller with a forward direction, the angle of attack between the chord and the relative airflow (V_o) must be positive. If the angle α is less than zero at any cross-section, it results in opposite thrust for that specific section, leading to an uneven distribution of thrust along the blade. To maintain a positive angle of attack everywhere, a suitable pitch angle β should be selected.

To calculate these forces, several methodologies can be employed. The "Blade Element Theory" uses non-dimensional coefficients of lift and drag to calculate differential thrust and torque, integrating them along the entire blade surface to determine the resultant forces. Another method is the "Integral Momentum Theorem," which mathematically formulates the continuity equation of the fluid flow and is based on the principle that the rate of change of momentum within a control volume moving with the flow is equal to the sum of the surface and internal forces acting on the fluid. These methodologies can provide satisfactory accuracy in calculating the forces of interest.

In this thesis, numerical methods are used in Chapters 3 (CFD) and 4 (FSI) to compute the fluid flow field (velocities and pressures) to subsequently obtain forces and moments through integration over the respective surfaces. In Chapter 5, where stability is studied, the aerodynamic forces are analytically computed based on the "Strip Theory," where each blade is divided into elemental sections, and local forces are calculated and summed to find the resultant quantities. These methodologies and equations applied will be presented in detail in their respective chapters.

2.3.2 Secondary Phenomena – Harmonic Loads

During the operation of the propeller, in addition to the distributions of lift and thrust forces that generate the propeller's overall thrust and torque, the propeller is also subjected to dynamic loads known as "nP loads" (1P, 2P, 3P, etc.). The factor "P" refers to the number of repetitions of the loading for one revolution of the propeller. These cyclic loads are the primary sources of loading for turboprop engines, and their study is essential for both the durability of the construction (fatigue resistance) and the integrity of the components (gearbox, engine, or blade). Engine manufacturers aim to limit the magnitude of these loads within the engine and aircraft's operating range (rotational speed, flight speed, altitude, etc.) and avoid resonance with the structural frequencies.

These loads primarily occur during take-off, turns, and maneuvers of the aircraft. In Figure 2.8, an aircraft is depicted in a take-off condition with the propeller's roto tube. The roto tube is a conceptual tube of vortex lines with a diameter approximately equal to the propeller's diameter, encompassing the airflow passing through the propeller. In this diagram, we observe that an angle is formed between the direction of the generated thrust and the flight path. This angle leads to the development of the dynamic propeller loads.

Understanding and analyzing these dynamic loads are crucial for designing robust propellers and ensuring their reliable performance and safety during flight operations. Proper consideration of these loads allows engineers to optimize the propeller's design, material selection, and operating conditions for enhanced performance and longevity.

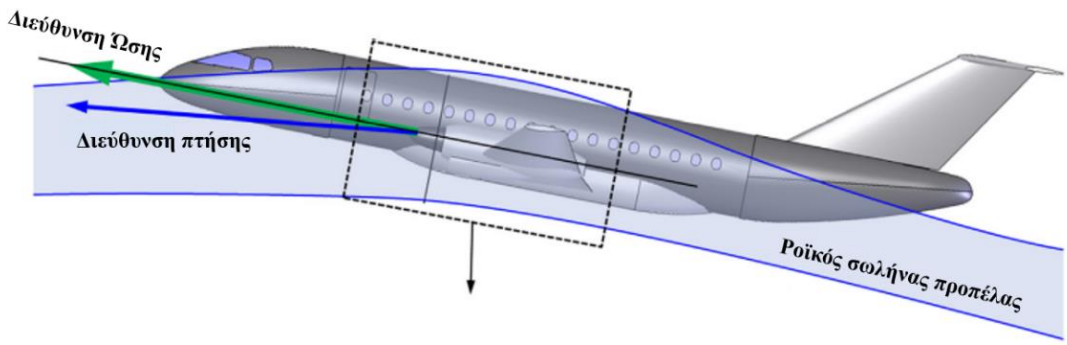

Figure 2.8 depicts the propeller's roto tube of an aircraft during take-off.

In Figure 2.9, three different views of an engine in take-off condition (e.g., an aircraft similar to Figure 2.8) are depicted. Using this diagram and the indicated dimensions, we will analyze the dynamic loads developed on the propeller.

Among the dynamic nP loads mentioned earlier, the most significant are the 1P loads (occurring per one rotation of the propeller). The term 0P refers to the static loads, while nP (where n=2, 3, 4, etc.) represents the harmonic components of the total load. These harmonic loads exert cyclic stresses on the propeller's blades with frequencies that are integer multiples of the propeller rotation frequency. The nP loads in the x and z directions act in the plane of the propeller rotation, leading to the bending of the shaft that connects the propeller to the gearbox. The importance of these loads lies in their much larger amplitude compared to other harmonic components in the plane of rotation.

Due to the angle psi (Figure 2.9a) between the axis of propeller rotation and the flight direction, there is a difference in the relative angle of attack seen by blades 1 and 5 of the propeller (Figure 2.9b). Blade 1, which is ascending, experiences a reduced angle alpha, while blade 5, which is descending, experiences an increased angle alpha. In the upper and lower blades (vertical position), the angle of attack is the same. Because of this, each blade of the propeller undergoes a sinusoidal variation in load during each rotation. The difference in load between blades 1 and 5 results in the development of a constant vertical force (1P lift) as shown in the front view of the engine. Additionally, the difference in lift between the two blades results in the development of a torque (1P torque) as shown in the side view of the engine. The nP loads represent the harmonic components of the total loads, and their frequencies, as mentioned before, are integer multiples of the propeller rotation frequency.

It's worth noting that the frequencies of the 1P, 2P, etc., components refer to the loads exerted on individual blades of the propeller. As we have two symmetric blades in our propeller, the larger

amplitudes will appear in the 2P components since the phenomenon described above will repeat itself once for each blade in each rotation of the propeller. The analysis we will conduct to calculate the harmonic components, their significance, and behavior is based on reference [13], where these loads are computed for a Prop-Fan engine. Furthermore, a more concise study of the harmonic components in an aircraft propeller is presented in reference [12].

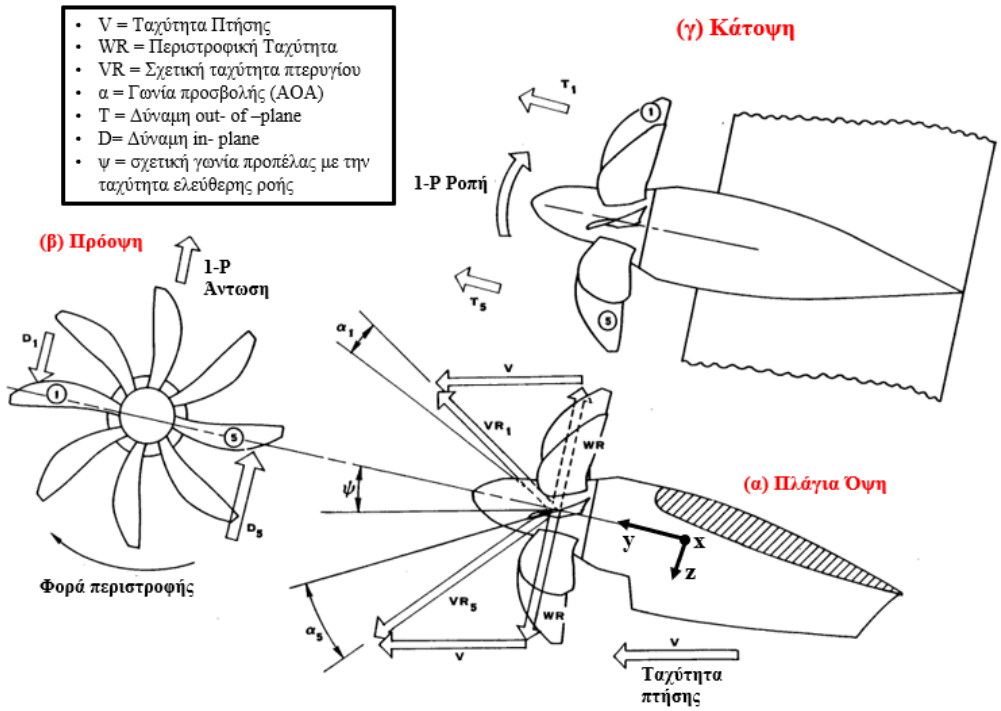

Figure 2.9 depicts different views of an engine in take-off condition and the essential parameters describing the P loads.

Figure 2.10 illustrates an example of cyclic loads with the static solution that commonly occurs in classic propeller applications. In Figure 2.10a, we observe the response of the total load developed during flight as a function of time, while in Figure 2.10b, we see the response of the 1P load for one period and its differentiation after adding higher-order harmonic components.

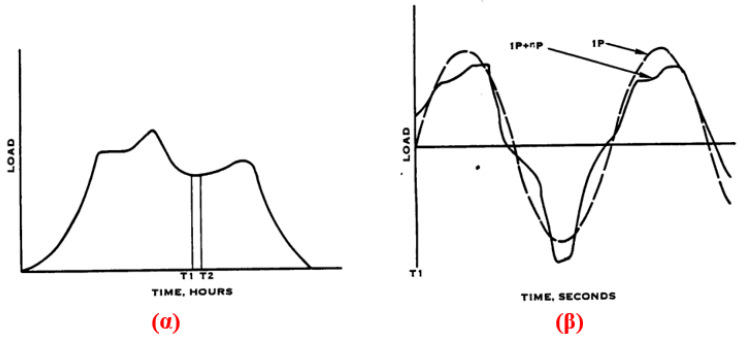

Σχήμα 2.10 Αρμονικές Συνιστώσες φόρτισης

The extraction and calculation of the harmonic components of the total load are performed using the Fourier transform and the Fast Fourier Transform (FFT) algorithm. The Fourier transform is a purely mathematical tool, which will be presented in detail in the next chapter.

2.4 Dimensionless coefficients and Mathematical notations

In this section, we define basic equations and mathematical notations that will be essential for interpreting the results and formulating the equations. In fluid mechanics problems, it is common practice to use dimensionless numbers to describe the characteristics of the flow. These dimensionless coefficients are derived through dimensional analysis applied to the specific problem at hand. By utilizing these coefficients, we can compare flow fields and their results for different systems. These dimensionless numbers reduce the number of variables needed to describe a system, thereby reducing the volume of experimental data required to correlate physical phenomena. Additionally, they allow us to study a problem in its dimensionless equivalent, scaled appropriately. Next, we present the fundamental dimensionless coefficients that we will use to describe our results, based on reference [7]

Mach Number $\boldsymbol{Ma} = \frac{\boldsymbol{V}}{\boldsymbol{c}}$. This number represents the ratio of the flow velocity to the speed of sound, denoted as 'c' [m/s]. The value of the Mach number, Ma, characterizes the flow as subsonic (Ma < 1), transonic (0.8 < Ma < 1.2), supersonic (Ma > 1.2), or hypersonic (Ma > 5). Additionally, for values of Ma > 0.3, the flow is considered compressible. Depending on the value of the Mach number, different flow phenomena can occur in our flow.

Reynolds Number $\boldsymbol{Re} = \frac{\boldsymbol{\rho V D}}{\boldsymbol{\mu}}$. Where ρ [kg/m^3] is the density, V [m/s] is the flow velocity, D [m] is a characteristic length of our flow, and μ [kg/(m s)] is the dynamic viscosity of the flow. The Reynolds number is the ratio of inertial forces to viscous forces. We use the Reynolds number, Re, to characterize the flow as laminar, transitional, or turbulent. The ranges of values for each characterization depend on the specific problem we are studying.

The dimensionless coefficients of forces and moments are obtained by dividing the respective force and moment by the product of density, velocity, and a characteristic length. Specifically, the coefficients we are interested in for the propeller are as follows.

- Thrust Coefficient $C_T = \frac{T}{\rho n^2 D^4}$
- Moment Coefficient $C_M = \frac{M}{\rho n^2 D^5}$

Where T, M, n, and D represent the thrust, torque, propeller revolutions, and its diameter, respectively.

- Dynamic Pressure $q_\infty = \frac{1}{2}\rho V_R^2 \ \ [Pa]$
- $V_R = \sqrt{V_0^2 + (\Omega r)^2}$
- Lift Coefficient $C_L = \frac{L}{q_\infty S}$

- Drag Coefficient $C_D = \frac{D}{q_\infty S}$
- Pressure Coefficient $C_p = \frac{p_1 - p_\infty}{q_\infty}$

Where L and D in [N] represent the lift and drag, respectively, S is a characteristic dimension, V_R is the relative velocity at the point being calculated, and $(p_1 - p_\infty)$ is the relative pressure at the point being calculated, measured in Pa (pascals).

- Power Coefficient $C_{Power} = \frac{Power}{\rho n^3 D^5}$

Where Power [Watt], is the Power that ends up to the propeller.

- Propeller Advance Ratio $J = \frac{V_\infty}{nD}$

The parameter J, or Advance Ratio, is essential in the presentation of the results. Its significance lies in the fact that for the same J value, regardless of the flow velocity or the rotational speed of the propeller, the propeller sees the same angle of attack (AOA) at the cross-sections of its blades.

In the derivation of the equations, we will be using some fundamental mathematical concepts and symbols, which are presented below based on references [4], [5], [7].

Tensors

The n-th order tensor is a set of N^n quantities that are transformed from one system x_i to x_i' using a transformation rule depending on the order n. The transformations are defined as follows:

n	Order	Transformation
0	Scalar α	$a(x_i') = a(x_i)$
1	Vector x_i	$x_i' = a_{ij}x_j$
2	Tensor T_{ij}	$T_{ij}' = a_{ik}a_{jl}T_{kl}$

The tensor represents a quantity with physical significance that exists independently of the reference system we use. The matrix quantifies the tensor with respect to a specific reference system. The values of the matrix depend on the specific coordinate system and change systematically if the reference system changes. In general, for tensors, it can be shown that:

$$A' = RAR^T$$

Here, R is the coordinate transformation matrix (rotation matrix) between two systems with different orientations. Additionally, the components of a vector transform as follows:

$$x_i' = a_{ij}\, x_j$$

$$Where\ x_j = a_{ij}\, x_i'$$

Substituting this into the equation gives:

$$x_j = a_{ij}\, a_{il}\, x_l$$

This equation is valid only if:

$$a_{ij}\, a_{il} \;=\; \delta_{jl}$$

For transformations that satisfy the above condition, we say they are orthogonal transformations. Tensors that satisfy orthogonal transformations are called Cartesian tensors. These tensors express physical quantities, and their values depend on the reference system. However, the invariant characteristics of these quantities remain constant. For example, a vector may have different coordinates in different reference systems, but its length remains constant.

Grad - Div - Curl

For Scalar, Vector and Tensor field we use the following notations :

1. Scalar field : $\Phi = \Phi(x,t), \quad \Phi = \Phi(\underline{x},t)$
2. Vector field : $v_i = v_i(x_i,t), \;\; \underline{v} = \underline{v}(\underline{x},t)$
3. Tensor Field : $T_{ij} = T_{ij}(x_i,t), \;\; \underline{T} = \underline{T}(\underline{x},t)$

Essentially, the scalar field represents a numerical value, the vector field is a vector, and the tensor field is a matrix.

The differential operator ∇ is called the del or Nabla operator and is defined as:

$$\nabla = \underline{e}_i \frac{\partial}{\partial x_i}$$

The differential operator Δ is called Laplacian operator and is defined as:

$$\Delta = \nabla \cdot \nabla = \frac{\partial}{\partial x_i} \cdot \frac{\partial}{\partial x_i}$$

The basic different operators that we use for scalar and vectorial domains are the following :

$$grad\, \Phi = \nabla\, \Phi = \Phi_i \underline{e}_i \quad (Vector)$$

$$div\, \underline{v} = \nabla\, \underline{v} = v_{i,i} \quad (Scalar)$$

$$curl\, \underline{v} = \nabla \times \underline{v} = \varepsilon_{ijk} v_{k,j} \quad (Vector)$$

With $curl$, Indicates the rotation or vorticity of the flow. Generally, similar rules apply to tensors.

Divergence Theorem

For a volume V with boundary A, the following integral transformation applies to the first-order tensor (vector) $\underline{g}$:

$$\int_V div\left(\underline{g}\right) dV = \int_V \nabla\left(\underline{g}\right) dV = \int_A \underline{n} \cdot \underline{g}\, dA$$

Where $\underline{n}$ is the unit normal vector on the boundary A. The divergence theorem tells us that the integral of the divergence (div) of $\underline{g}$ over the volume dV is equal to the outward flux of a vector field $\underline{g}$ through a closed surface with boundary dA.

Physical – Computational domain

Another distinction we will be concerned with in the next chapters is the differentiation between the Natural and Computational space of each problem. The definition of the Natural space is easy to understand. The Natural space includes our system, whether it is a construction or even a fluid. Visually, for most problems, the human mind automatically defines the Natural space, in which the problem is defined, and recognizes the conditions at the boundaries that accompany it.

On the other hand, the concept of the computational field, especially when our system includes fluid, is not so clear-cut. For instance, in a construction, the field in which we solve and define our equations consists of the space covered by the construction itself, and the boundaries of our space are defined by the surface of the construction. However, when dealing with fluids, we need to define our computational field and then subsequently define the boundary conditions within this space.

So, by definition, we could say that a computational field is the space with known conditions at its boundaries, in which the equations expressing the system are defined and solved. For example, when applying Computational Fluid Dynamics (CFD) methods, it's necessary to define the control volume (computational field) in which, after discretization, we will solve the equations to compute the variables of the fluid field. When choosing the geometry and dimensions of this volume, each engineer should rely on their fluid mechanics knowledge and their understanding of the nature of the problem.

3. FLUID MECHANICS PROPELLER ANALYSIS

In Chapter 3, we consider our propeller as solid. This assumption simplifies our analysis but reduces the accuracy of our results. One might wonder why we introduce this simplification. In complex systems like ours, where intricate phenomena develop, treating the propeller as solid allows us to conduct a preliminary study of the system. This initial study provides us with information that revolves around the solutions of the more accurate model. A more detailed explanation of the differences between deformable and solid bodies will be presented in Chapter 4, where our propeller model is considered deformable.

The goal of this chapter is to introduce the fundamental principles governing aircraft propellers and the phenomena associated with them. This serves as a stepping stone to more complex concepts to be presented in Chapter 4. Our primary objective is to provide an initial overview and derive results that will later be compared with the more accurate results from the fluid-structure interaction solution presented at the end of Chapter 4.

In this chapter, we exclusively focus on the fluid mechanics aspect of the propeller. To structure the text, we begin with a presentation of the theory, derive the equations, describe the solution methods, and provide all the necessary tools for interpreting our results. After covering the entire theoretical portion, we introduce the relevant software and present our findings.

3.1 Formulation of Equations and Numerical Methods

When we refer to solving the fluid field, we mean calculating variables such as velocity, pressure, density, temperature, etc. To calculate these quantities, we first need to formulate the equations that describe our fluid field. After formulating these equations, we then invoke simplifying models that make it feasible to solve the equations. In their complete form, especially for complex geometries, finding a solution (either numerical or analytical) is not feasible using today's computational resources.

Once the equations are formulated, this section concludes with the numerical methods we employ to solve these equations. The formulation of these equations is done based on reference [8].

3.1.1 Formulation of Equations URANS

The equations governing the fluid field, in whatever form they may appear, are based on three fundamental physical principles:

1) Mass is conserved.

2) Newton's second law, **F=ma.**

3) Energy is conserved.

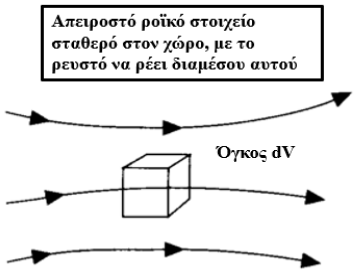

figure 3. 1 Static infinitesimal fluid element

Applying each one of these principles to an appropriate model provides us with a set of equations. We begin with the assumption of an infinitesimal fluid element, which remains fixed in space while the fluid flows through it, as shown in Figure 3.1. Choosing this model for formulating the equations of the fluid field leads to the conservative form of the equations. By applying the above principles one by one, we obtain the equations of our field:

1) Mass is conserved → Continuity Equation
2) $\mathbf{F} = \mathbf{ma}$ → Momentum equation (Navier – Stokes equations)
3) Energy is conserved → Energy equation.

Continuity Equation

In Figure 3.2, the quantities of the fluid element and mass flows through it are presented with respect to a Cartesian coordinate system. Mass flow is defined as the product of velocity and density, giving us mass flow per unit surface area (ρu, ρv, ρw). All quantities of the fluid field have spatial and temporal dependence.

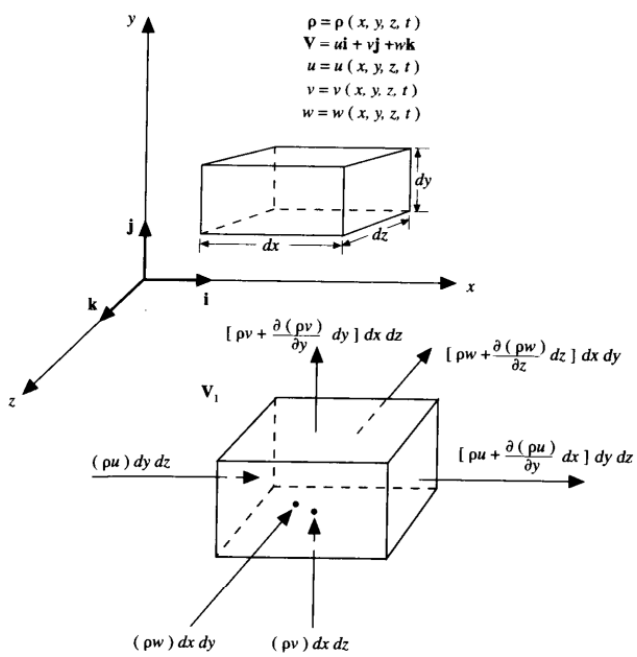

Σχήμα 3. 2 infinitesimal fluid element Model and mass flow through the element's surface.

By subtracting the quantities that enter and exit the element, we calculate the mass flow through the element in the same direction. For example, in the x-direction:

$$\left[\rho u + \frac{\partial(\rho u)}{\partial y} dx\right] dydz - (\rho u) dydz = \frac{\partial(\rho u)}{\partial y} dxdydz$$

Summing up the flows for all three directions, we have:

$$Total\ mass\ Flow = \left[\frac{\partial(\rho u)}{\partial x} + \frac{\partial(\rho v)}{\partial y} + \frac{\partial(\rho w)}{\partial z}\right] dxdydz \ \ (\mathbf{3.1})$$

The rate of change of mass inside the element is defined as the rate of change of the element's density multiplied by its volume. Therefore, we have:

$$Mass\ rate\ of\ change\ for\ element = \frac{\partial(\rho)}{\partial t}(dxdydz) \ \ (\mathbf{3.2})$$

We equate equations (3.1) and (3.2) and express the partial derivatives in a compact form using the divergence operator div(∇) for the term $\rho\underline{V}$:

$$\nabla() = \left(\frac{\partial}{\partial x} + \frac{\partial}{\partial y} + \frac{\partial}{\partial z}\right)$$

We get:

$$\frac{\partial(\rho)}{\partial t} + \nabla\left(\rho\underline{V}\right) = 0 \ \ (\mathbf{3.3})$$

This equation is a partial differential equation and represents the conservative form of the continuity equation for the fluid field.

<u>Momentum equation (Navier – Stokes)</u>

In Figure 3.3, the fluid element is shown along with all the shear stresses and pressures (normal stresses) acting on it in all directions. The forces acting on the element consist of surface forces, as depicted in the diagram, and internal forces f (such as gravitational, centrifugal, and electrical forces) that act from a distance. The internal forces can be written per unit mass as:

$$Internal\ body\ forces\ x = f_x\rho(dxdydz)\ (\mathbf{3.4})$$

Similarly, by summing the surface forces acting in the x-direction, as shown in the diagram, we have:

$$Surface\ forces = \left[-\frac{\partial p}{\partial x} + \frac{\partial \tau_{xx}}{\partial x} + \frac{\partial \tau_{yx}}{\partial y} + \frac{\partial \tau_{zx}}{\partial z}\right] dxdydz\ (\mathbf{3.5})$$

Also, the mass of the element is given by the relation: ($m\ = \rho dxdydz$) **(3.6).** Therefore, we need to calculate the acceleration term in the second law of Newton. Using the divergence theorem for vector quantities, we have for the x-direction:

$$\rho\ a = \frac{\partial(\rho u)}{\partial t} + \ \nabla\left(\rho u\underline{V}\right)\ (\mathbf{3.7})$$

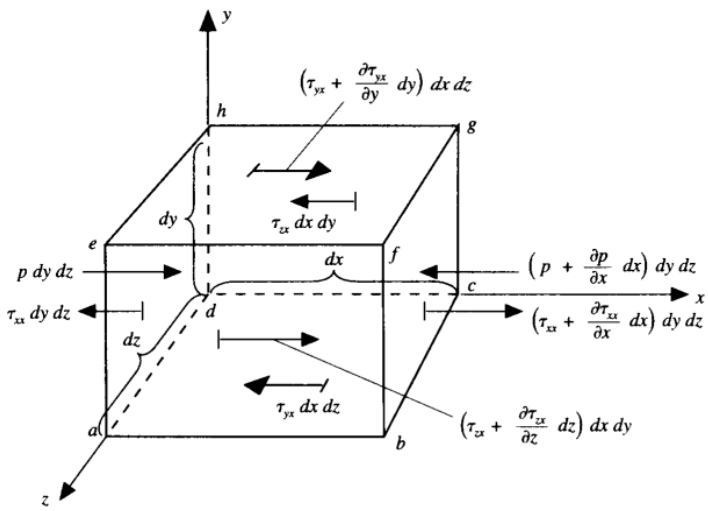

Σχήμα 3. 3 Force diagram for infinitesimal, steady in space, fluid element.

Introducing equations (3.4) to (3.7) into the second law of Newton ($F = ma$) gives us the momentum equation for the x-direction. Applying the same procedure for the other two directions, we obtain the conservative form of the Navier-Stokes equations in their full form for all three directions:

$$\begin{cases} \dfrac{\partial(\rho u)}{\partial t} + \nabla\left(\rho u \underline{V}\right) = -\dfrac{\partial p}{\partial x} + \dfrac{\partial \tau_{xx}}{\partial x} + \dfrac{\partial \tau_{yx}}{\partial y} + \dfrac{\partial \tau_{zx}}{\partial z} + \rho f_x \\ \dfrac{\partial(\rho v)}{\partial t} + \nabla\left(\rho v \underline{V}\right) = -\dfrac{\partial p}{\partial y} + \dfrac{\partial \tau_{xy}}{\partial x} + \dfrac{\partial \tau_{yy}}{\partial y} + \dfrac{\partial \tau_{zy}}{\partial z} + \rho f_y \\ \dfrac{\partial(\rho w)}{\partial t} + \nabla\left(\rho w \underline{V}\right) = -\dfrac{\partial p}{\partial z} + \dfrac{\partial \tau_{xz}}{\partial x} + \dfrac{\partial \tau_{yz}}{\partial y} + \dfrac{\partial \tau_{zz}}{\partial z} + \rho f_z \end{cases}$$

According to Newton, the shear stresses that appear in these equations are proportional to the rate of change of the strains, where strain is defined as the velocity gradient. Thus, they can be expressed as:

$$\tau_{xx} = \lambda\nabla\left(\underline{V}\right) + 2\mu\frac{\partial u}{\partial x}, \tau_{yy} = \lambda\nabla\left(\underline{V}\right) + 2\mu\frac{\partial v}{\partial y}, \tau_{zz} = \lambda\nabla\left(\underline{V}\right) + 2\mu\frac{\partial w}{\partial z}$$

$$\tau_{xy} = \tau_{yx} = \mu\left[\frac{\partial v}{\partial x} + \frac{\partial u}{\partial y}\right], \tau_{xz} = \tau_{zx} = \mu\left[\frac{\partial u}{\partial z} + \frac{\partial w}{\partial x}\right], \tau_{yz} = \tau_{zy} = \mu\left[\frac{\partial w}{\partial y} + \frac{\partial v}{\partial z}\right]$$

Where μ is the dynamic viscosity of the fluid and λ is the second viscosity coefficient. According to Stokes' hypothesis, λ is equal to -2/3μ. Substituting the expressions for the shear stresses into the Navier-Stokes equations and writing the resulting system in a compact form, we have:

$$\frac{\partial}{\partial t}\left(\rho\underline{V}\right) + \nabla\left(\rho\underline{V}\,\underline{V}\right) = -\nabla \mathrm{p} + \nabla(\bar{\bar{\tau}}) + \underline{F} \quad (\mathbf{3.8})$$

Where p is the static pressure, V is the velocity vector of the fluid, ρ is the density of the fluid, $\underline{F}$ is the vector of internal forces, and $\bar{\bar{\tau}}$ is the stress tensor.

Energy Equation

For systems that do not include energy diffusion, thermal diffusion, chemical changes, and compressibility effects, the continuity and momentum equations derived so far are capable of calculating the quantities of the fluid flow field. However, for our system, due to the high rotational speeds of the propeller, there are regions on its blades that exhibit compressible flow Mach numbers. ($M = \frac{V}{a}$,). For Mach numbers smaller than 0.3, the flow can be considered entirely incompressible, while for Mach numbers greater than 0.3, we need to include the energy equation in the solution. Applying the third fundamental principle for an infinitesimal fluid element at rest in space, we can express the energy conservation balance as follows:

$$\mathrm{A} = \mathrm{B} + C$$

Where :

A= $Rate\ of\ energy\ change\ inside\ the\ fluid\ element$

B= $Heat\ flow\ through\ the\ element$

C= $Rate\ of\ change\ of\ work\ due\ to\ internal\ and\ surface\ forces$

We are dealing with the above terms one by one. For our system, the term of heat flow is zero (B=0), as there is no source of heat transfer, and furthermore, the values of the Mach number above the propeller are less than 5. Initially, for term C, the work generated by the internal forces of the particles for a fluid element moving at velocity $\underline{V}$, arises from the relationship: $\rho \underline{f}\ \underline{V}(dxdydz)$ $(\mathbf{3.9})$**.** For the surface forces, the rate of change of work in the three directions is equal to the resultant force times the velocity in each respective direction. Thus, for the x-direction, we have:

$$C_x = \left[-\frac{\partial(up)}{\partial x} + \frac{\partial(u\tau_{xx})}{\partial x} + \frac{\partial(u\tau_{yx})}{\partial y} + \frac{\partial(u\tau_{zx})}{\partial z}\right] dxdydz \ \ (\mathbf{3.10})$$

The equations for the other two directions are calculated in the same way. The rate of change in energy within the element (A) involves contributions from both internal (e) and kinetic energy $\left(\frac{V^2}{2}\right)$. Therefore, the energy per unit mass contained within the infinitesimal element is equal to the sum of these two quantities.

$$A_1 = \frac{\partial}{\partial t}\left(\rho\left(e + \frac{V^2}{2}\right)\right)(dxdydz)\ (\mathbf{3.11})$$

The mass entering the element adds an amount of energy, and the mass leaving it subtracts. Thus, the flow of energy in the x direction from the surfaces of the element is given by:

$$A_{2x} = \rho\frac{\partial u}{\partial x}\ (dxdydz)\left(e + \frac{V^2}{2}\right)$$

For 3 dimension becomes: $A_2 = +\nabla\left[\rho\left(e + \frac{V^2}{2}\right)\underline{V}\right]$

So : $A = A1 + A2 = \frac{\partial}{\partial t}\left(\rho\left(e + \frac{V^2}{2}\right)\right) + \nabla\left[\rho\left(e + \frac{V^2}{2}\right)\underline{V}\right]$ $(\mathbf{3.12})$

By incorporating equations (3.9) to (3.12) into the energy balance A = B + C, we obtain the conservative energy equation in vector form :

$$\frac{\partial}{\partial t}\left(\rho\left(e + \frac{V^2}{2}\right)\right) + \nabla\left[\rho\left(e + \frac{V^2}{2}\right)\underline{V}\right] = -\nabla[\underline{V}\,p] + \nabla[\bar{\bar{\tau}}\underline{V}] + \rho\underline{f}\,\underline{V} \quad (\mathbf{3.13})$$

These equations, which include the continuity equation (3.3), momentum equation (3.8), and energy equation (3.13), in their complete forms, constitute the non-steady-state equations of the fluid field. A more detailed description of the derivation of these equations and the different models used to generate them can be found in reference [8].

These equations can only be solved for very simple problems with straightforward geometries. When dealing with flows of high Reynolds numbers and significant turbulence, it becomes impossible to solve the above equations. Turbulent flows manifest on very small spatial scales. Approximately, we consider that the smallest turbulence scale is 10^9 times smaller than the largest dimension of the system. If the dimensions of our system are measured in meters, this means that we would need 10^{12} grid elements to describe the problem. We understand that, from a computational perspective with today's data, this is impossible for a computer when seeking a solution for a transient phenomenon (time-dependent).

An alternative method can be used to make these equations solvable, such that the small scales of turbulence don't need to be computed directly. The "Favre-Averaging" or "Compressible Reynolds-Averaging" method introduces additional terms for turbulence into the equations, transforming them into a solvable set of equations. After applying this method, the resulting equations are referred to as "Unsteady Compressible Reynolds-Averaged Navier-Stokes (URANS) equations."

This approach is particularly useful for dealing with turbulent flows, where the small-scale turbulence is complex and computationally intensive to calculate directly. Instead, turbulence is modeled through additional terms, making it more manageable for numerical simulations.

From experiments, we have observed that the velocities within a flow field exhibit variations around a mean value. The spatially dependent mean values of velocity, often considered in fluid dynamics, are represented as $\overline{u}(x,y,z)$, $\overline{v}(x,y,z)$, $\overline{w}(x,y,z)$ and the fluctuations, which are considered to carry both temporal and spatial dependencies of the field, are represented as $u'(x,y,z,t), v'(x,y,z,t), w'(x,y,z,t)$. These fluctuations refer to the deviations of each variable from its mean value. The mean values are initially taken as time-averaged values:

$$\tilde{u}(x,y,z) = \lim_{\Delta t \to \infty} \frac{1}{\Delta t}\int_T^{T+\Delta T} u(x,y,z,t)\ dt$$

$$\tilde{\rho}(x,y,z) = \lim_{\Delta t \to \infty} \frac{1}{\Delta t}\int_T^{T+\Delta T} \rho(x,y,z,t)\ dt$$

$$\widetilde{\rho u}(x,y,z) = \lim_{\Delta t \to \infty} \frac{1}{\Delta t}\int_T^{T+\Delta T} \rho(x,y,z,t)u(x,y,z,t)\ dt$$

Next, we introduce a density-weighted mean:

$$\overline{u} = \frac{\widetilde{\rho u}}{\tilde{\rho}}$$

Applying the same procedure to all 3 velocity components we have:

$$u(x,y,z,t) = \overline{u}(x,y,z) + \mathrm{u}'(x,y,z,t)$$

$$v(x,y,z,t) = \overline{v}(x,y,z) + v'(x,y,z,t)$$

$$w(x,y,z,t) + \overline{w}(x,y,z) + w'(x,y,z,t)$$

The same logic is applied to pressure, density, and all scalar quantities, denoted as φ, of the flow field:

$$\tilde{\varphi} = \lim_{\Delta t \to \infty} \frac{1}{\Delta t} \int_{T}^{T+\Delta T} \varphi \ dt$$

$$\overline{\varphi} = \frac{\widetilde{\rho\varphi}}{\tilde{\rho}}$$

$$\varphi = \overline{\varphi} + \varphi'$$

Substituting these expressions into the continuity and momentum equations yields:

$$\textit{Εξίσωση Συνέχειας}: \ \frac{\partial \overline{\rho}}{\partial t} + \nabla\left(\overline{\rho}\,\underline{V}\right) = 0 \quad (\mathbf{3.14})$$

Momentum equation :

$$\frac{\partial(\overline{\rho}\,\overline{u})}{\partial t} + \nabla\left(\overline{\rho}\,\overline{u}\underline{V}\right) = -\frac{\partial \overline{p}}{\partial x} + \nabla(\mu\,\nabla\,\overline{u}) + \left[-\frac{\partial\overline{\left(\overline{\rho}\,u'^{2}\right)}}{\partial x} - \frac{\partial\overline{(\overline{\rho}\,u'v')}}{\partial y} - \frac{\partial\overline{(\overline{\rho}\,u'w')}}{\partial z}\right] + F_x \quad (\mathbf{3.15})$$

$$\frac{\partial(\overline{\rho}\,\overline{v})}{\partial t} + \nabla\left(\overline{\rho}\,\overline{v}\underline{V}\right) = -\frac{\partial \overline{p}}{\partial y} + \nabla(\mu\,\nabla\,\overline{v}) + \left[-\frac{\partial\overline{(\overline{\rho}\,u'v')}}{\partial x} - \frac{\partial\overline{\left(\overline{\rho}\,v'^{2}\right)}}{\partial y} - \frac{\partial\overline{(\overline{\rho}\,v'w')}}{\partial z}\right] + F_y \quad (\mathbf{3.16})$$

$$\frac{\partial(\overline{\rho}\,\overline{w})}{\partial t} + \nabla\left(\overline{\rho}\,\overline{w}\underline{V}\right) = -\frac{\partial \overline{p}}{\partial z} + \nabla(\mu\,\nabla\,\overline{w}) + \left[-\frac{\partial\overline{(\overline{\rho}\,u'w')}}{\partial x} - \frac{\partial\overline{(\overline{\rho}\,w'v')}}{\partial y} - \frac{\partial\overline{\left(\overline{\rho}\,w'^{2}\right)}}{\partial z}\right] + F_z \quad (\mathbf{3.17})$$

For problems with a low Mach number (M < 1), according to reference [16], there is no need to solve the energy equation, as the influence of compressibility is taken into account within the equations due to the weighted average with respect to density. Equations (3.14) - (3.17) are considered sufficient to compute the flow field and consider compressibility effects. Using index notation for the above equations, we obtain the system of equations (I):

$$\begin{cases} \dfrac{\partial \overline{\rho}}{\partial t} + \dfrac{\partial}{\partial x_i}(\overline{\rho}\, u_i) = 0 \\ \dfrac{\partial(\overline{\rho}\, u_i)}{\partial t} + \dfrac{\partial}{\partial x_i}(\overline{\rho}\, u_i u_j) = -\dfrac{\partial \overline{p}}{\partial x_i} + \dfrac{\partial}{\partial x_i}\left(\mu\left(\dfrac{\partial u_i}{\partial x_j} + \dfrac{\partial u_j}{\partial x_i} - \dfrac{2}{3}\delta_{ij}\dfrac{\partial u_i}{\partial x_i}\right)\right) + \dfrac{\partial}{\partial x_j}\left(-\rho\overline{u_i' u_j'}\right) + F_i \end{cases} \quad (\boldsymbol{I})$$

Where $i, j = 1, 2, 3$, with correspondence to the Cartesian coordinate system where $1 = x, 2 = y$, and $3 = z$, and using the notation $(\overline{u_i'\, u_j'})$, we refer to the Reynolds stress tensor, which has the form:

$$\overline{u_i' u_j'} = \begin{bmatrix} \overline{u_1' u_1'} & \overline{u_1' u_2'} & \overline{u_1' u_3'} \\ \overline{u_2' u_1'} & \overline{u_2' u_2'} & \overline{u_2' u_3'} \\ \overline{u_3' u_1'} & \overline{u_3' u_2'} & \overline{u_3' u_3'} \end{bmatrix}$$

3.1.2 Turbulence Model SST k -ω

At this point, it is necessary to define a model capable of describing the turbulence variables in the URANS equations. The new terms in the above equations (u_i', u_j') represent turbulence phenomena. These stresses, according to the Boussinesq hypothesis, are related to the gradient of the mean velocity, which is given by the equation:

$$\rho\overline{u_i' u_j'} = \mu_t\left(\frac{\partial u_i}{\partial x_j} + \frac{\partial u_j}{\partial x_i}\right) - \frac{2}{3}\left(\rho k + \mu_t \frac{\partial u_k}{\partial x_k}\right)\delta_{ij}$$

Where μ_t is the turbulent viscosity and k is the turbulent kinetic energy. The benefit of expressing the stresses with this assumption is the low computational cost associated with calculating the μ_t term. This assumption can be applied to the SST k-ω turbulence model (Shear Stress Transport model).

The advantages of the SST k-ω model lie in its ability to express large pressure gradient differences within the flow field and the detachment of the flow from walls. A necessary condition for the correct functioning of the model is the proper discretization and the small y^+ number at the walls. More details about this number will be presented during the discretization of the flow field.

The SST k-ω model uses a blending function to ensure a gradual transition from the classical k-ω model near the walls to the high Reynolds number k-ε model in the farther parts of the boundary layer. The model consists of 2 equations, which complement the URANS equations using turbulence viscosity and calculate the transport phenomena due to the principal shear stresses. These two equations are:

$$\frac{\partial}{\partial t}(\rho k) + \frac{\partial}{\partial x_i}(\rho k u_i) = \frac{\partial}{\partial x_j}\left(\Gamma_k \frac{\partial k}{\partial x_j}\right) + G_k - Y_k + S_k$$

$$\frac{\partial}{\partial t}(\rho \omega) + \frac{\partial}{\partial x_i}(\rho \omega u_i) = \frac{\partial}{\partial x_j}\left(\Gamma_\omega \frac{\partial \omega}{\partial x_j}\right) + G_\omega - Y_\omega - D_\omega + S_k$$

- G_k : The generation of turbulent kinetic energy k due to the velocity gradient.
- G_ω: $The\ generation\ of\ specific\ turbulent\ dissipation\ \omega\ due\ to\ the\ velocity\ gradient.$

- Γ_k and Γ_ω: $Coefficients\ of\ turbulent\ kinetic\ energy\ k\ and\ turbulent\ dissipation\ \omega\ diffusion.$
- Υ_k and Υ_ω: $Turbulent\ diffusion\ of\ k\ and\ \omega.$
- D_ω: $Secondary\ diffusion\ term.$
- S_k: $Uncertain\ source\ terms.$

Now, we have completed the formulation of the equations necessary for the computation of the turbulent field and the representation of turbulent flow characteristics. This system consists of the URANS equations and the turbulence model equations. In the next subsection, we present the numerical methods we will use to solve these equations.

3.1.3 Numerical Solution Methodology

For the numerical solution of the unsteady Reynolds-Averaged Navier-Stokes equations, we employ the Finite Volume Method (FVM). In regions of the grid that exhibit relative motion between them (such as a rotating propeller mesh), we introduce the 'Sliding Mesh' method into the FVM equations. Subsequently, these two approaches are presented separately, using an application example for each method.

<u>Finite Volume Method (FVM)</u>

The Finite Volume Method (FVM) is a discretization method used for the approximate numerical solution of one or a system of partial differential equations (PDEs) that express conservation or equilibrium of one or more quantities. To apply the method, we first construct a spatial grid consisting of elements called control volumes. More information about the characteristics of these elements will be presented in Section 3.5. The discretization of PDEs in each control volume yields a balance equation for each volume. The entire system of equilibrium equations is then spatially discretized with respect to the unknowns we are seeking, aiming to compute the variables at the surfaces of each control volume.

The main challenge faced is spatial discretization of fluxes at the boundaries of control volumes. Flow is defined as any phenomenon that crosses a surface (e.g., mass flow across ($x\ = \rho\ u\ dxdydz$)). The difference between the FVM and the Finite Difference Method (FDM) is that in FVM, discretization is done on the equilibrium equations (after integration), whereas in FDM, it is directly done on the PDEs. After discretization, the resulting system consists of temporal derivatives and linear or non-linear algebraic equations, which can be solved either analytically or using iterative methods (linear or non-linear problems). The system of discretized equations depends on the characteristics of the engineering problem at hand.

The URANS equations and the turbulence model equations can be written for a general variable φ, which can represent all the quantities of the Navier–Stokes equations, the turbulence model equations, and all the properties added by the Finite Volume Method. To understand the application of the FVM, we apply it to the general form of the conservation equation (the general statement of the continuity equation) for the scalar quantity φ:

$$\frac{\partial(\rho\varphi)}{\partial t} + \nabla\left(\rho\varphi\underline{u}\right) = \nabla\left(\Gamma_\varphi \nabla\varphi\right) + S_\varphi$$

By integrating this equation over an arbitrary control volume of our grid, we obtain:

$$\int_{CV} \frac{\partial \rho\varphi}{\partial t} dV + \oint \rho\varphi \underline{u}\, \underline{dA} = \oint \Gamma_\varphi \nabla\varphi \underline{dA} + \int_{CV} S_\varphi dV = 0 \quad (\mathbf{3.18})$$

Where :

- ρ = density
- u = 3 dimensional velocity vector
- A = Surface vector
- $\Gamma_\varphi, S_\varphi$ = Diffusion term and source term of φ per unit volume.
- $\nabla\varphi$ = Slope φ
- CV = control volume

The equation (3.18) is applied to each control volume within the computational domain. After solving the integrals, the spatially discretized equations we obtain are in the form:

$$\frac{\partial \rho\varphi}{\partial t} V + \sum_f^N \rho_f \underline{u_f} \varphi_f \underline{A_f} = \sum_f^N \Gamma_\varphi \nabla \varphi_f \underline{A_f} + S_\varphi V \quad (\mathbf{3.19})$$

Where :

- N = the number of surfaces surrounding the control volume element.
- φ_f = φ value transmitted through surface f
- $\rho_f \underline{u_f}\, \underline{A_f}$ = mass flow through surface f (convection term)
- $\left|\underline{A_f}\right|$ = area of surface f
- $\nabla \varphi_f$ = φ slope on the surface f
- V = element's volume

The process of calculating the time derivative, as distinguished in this equation, will be calculated later. Equation (3.19) includes the unknown scalar quantity φ at the center of the element, as well as the unknown values of various quantities on the neighboring surfaces f that define the element. This equation is generally nonlinear. The goal of spatial discretization is to interpolate the values of the variable φ at the centers of volume elements so that we can calculate the values of the variable on the surfaces of the volume (φ_f). Before we proceed to the discretization schemes, it should be noted that the gradients of the quantities in the field ∇φ at the center of the volume element, which appear in the equations, are calculated using the 'Green-Gauss' theorem. According to this theorem, the gradients are calculated from the equation:

$$\nabla\varphi = \frac{1}{V} \sum_f \underline{\varphi_f}\, \underline{A_f}$$

The sum includes all the surfaces of the volume element, and the term φ_f on the surfaces is calculated using the discretization methods presented below.

- **Spatial Discretization**

We use a second-order upwind scheme for the convection terms $\left(\rho_f \, \underline{u_f} \, \varphi_f \, \underline{A_f}\right)$. The forward direction is defined in the direction of the normal velocity component on the specific surface (2nd order upwind). For the diffusion terms $\left(\Gamma_\varphi \, \nabla \, \varphi_f \, \underline{A_f}\right)$, we discretize using central finite differences, which always have second-order accuracy. The equations for the discretization of these terms are as follows:

For the convection terms, we expand the variable at the center of the control volume in a Taylor series:$\varphi_{f,SOU} = \varphi + \nabla\varphi \, \underline{r}$

Where :

- $\varphi \; and \; \nabla\varphi$ = Value φ and slope φ in the center of the volume element.
- $\underline{r}$ = displacement vector, starting at element's center with direction to the surface that we want to calculate the term φ_f
- SOU = Second Order Upwind

For the diffusion terms:

$$\varphi_{f,CD} = \frac{1}{2}(\varphi_0 + \varphi_1) + \frac{1}{2}\left(\nabla\varphi_0 \underline{r}_0 + \nabla\varphi_1 \underline{r}_1\right)$$

The terms in the above equation have the same interpretation as in the previous discretization scheme, with the difference being that the subscripts 0 and 1 refer to the two surfaces where we apply the central difference.

- **Spatial Discretization**

For the temporal derivatives that appear in equation (3.19), we apply a second-order discretization scheme based on the following formula:

$$\frac{\partial\varphi}{\partial t} = \frac{3\varphi^{n+1} - 4\varphi^n + \varphi^{n-1}}{2\Delta t}$$

We get : $\frac{3\varphi^{n+1} - 4\varphi^n + \varphi^{n-1}}{2\Delta t} = F(\varphi)$

Where the function F includes all the terms from spatial discretization. The remaining step is to determine for which time step we will compute the quantities of the function F. We apply an implicit time integration method. Thus, the function F is calculated for the time step n+1:

$$\frac{3\varphi^{n+1} - 4\varphi^n + \varphi^{n-1}}{2\Delta t} = F(\varphi^{n+1}) \quad (\mathbf{3.20})$$

The equation (3.20), since it includes terms for the time step (n+1), is solved iteratively for each time step, and then we proceed to the next time step. The advantage of using a fully implicit discretization scheme is that during our numerical solution, regardless of the choice of the time step, the solution remains numerically stable. Different discretization schemes, both in time and

space, as well as a description of the advantages of each scheme, can be found in references [8] and [16].

Sliding Mesh Method

There are various methods that can be used to solve the flow field in regions of a computational domain where relative motion exists between the grids. These methods include the 'Single Rotating Frame,' 'Multiple Rotating Frame,' and 'Sliding Mesh Method.'

For the first two methods ('Single Rotating Frame' and 'Multiple Rotating Frame'), there is no relative motion between different control volumes within the computational domain, but coordinate systems can be moving. The variables are computed with respect to the rotating coordinate systems, and appropriate terms representing the hypothetical grid motion are introduced. These approaches are suitable for fast solutions, particularly for steady-state simulations, but are less effective for transient phenomena because they cannot predict non-steady behaviors between the relatively moving control volumes.

For higher accuracy, the third method involves relative rotation between different control volume grids. The computed variables are then expressed in an inertial coordinate system. This method is typically used to calculate transient phenomena and quantities between moving surfaces.

The 'Sliding Mesh' method is one of the many techniques used to calculate non-steady flow fields, especially when you want to observe the response of field variables. In this method, the solution is periodically expressed, with a period related to the velocity of the moving grids in our system, which, for example, could be the rotational speed of a propeller. To illustrate this, consider the continuity equation for dynamically changing grids (moving in time). The equation for an arbitrary scalar variable φ of the flow field is:

$$\frac{d}{dt}\int_V \rho\varphi dV + \int_{\partial V} \rho\varphi\left(\underline{u} - \underline{u_m}\right)\underline{dA} = \int_{\partial V} \Gamma\nabla\varphi\underline{dA} + \int_V S_\varphi dV$$

We observe that the differentiation of this equation, compared to the one presented in the Finite Volume Method (FVM) application, lies in the grid velocity term $\underline{u_m}$. The time derivative of the integral in the above equation is replaced by a first order backward finite difference.

$$\frac{d}{dt}\int_V \rho\varphi dV = \frac{[(\rho\varphi)^{n+1} - (\rho\varphi)^n]V}{\Delta t}$$

Where :

- V = arbitrary control volume
- $\underline{u}$ = flow velocity
- $\underline{u_m}$ = moving grid's velocity
- Γ, S_φ = diffusion and source term respectively, for our system $S_\varphi = 0$
- $\partial V =$ Volume's V border

The n and n+1 represent the quantities at the time instances n and n+1, respectively. The above equation is applied to all the volume elements (control volumes) of the grid that move at different

velocities compared to the inertial coordinate system. The spatial discretization of the equations is performed using the same procedure as mentioned in the previous section.

The 'Sliding Mesh' method is considered a specific case of dynamically moving grids, where all individual cells (control volumes) can move solidly with respect to each other in contact regions. By 'solid,' we mean that one mesh does not overlap with another, and there is continuity in the distribution of mesh nodes; two nodes that are adjacent remain adjacent.

As a conclusion of the formulation of the system equations and solution methodologies, it should be noted that to improve the calculation speed of the flow field, a relaxation process is employed. Specifically, for each quantity calculated using the presented procedures (e.g., φ), we apply an iterative process to enhance the solution in the form:

$$\varphi^{n+1} = \varphi^{n} + \omega\left(\overline{\varphi}_{i,j}^{n+1} - \varphi^{n}\right)$$

Where n is the iteration step, ω is the relaxation coefficient (ω<1), and ¯φ_(i,j)^(n+1) is the mean value for the quantity φ of the control volumes surrounding the central control volume for which we are calculating φ.

3.2 Fourier Transform and Signal Analysis

It is important, as we mentioned in Chapter 2, to calculate the harmonic components of the propeller forces, as they are of great significance for the lifespan of the construction as well as our entire engine. The results we obtain from solving the system are in the form of signals at discrete time intervals. To analyze signals and extract their harmonic characteristics (amplitude and frequency), we use the Fourier transform. Specifically, since we are dealing with discrete times, we use the discrete Fourier transform. In this section, we present the theory of the Fourier transform and two methods used for its numerical solution. These methods are the discrete Fourier transform and the fast Fourier transform (FFT). The equations and theory presented in this section are based on reference [2].

3.2.1 Fourier Transform

The Fourier transform is an integral transform that takes us from the time domain to the frequency domain for time-dependent functions. Through this process, a time-dependent function is analyzed into components with amplitude and phase dependent on the respective frequencies (harmonics 1P, 2P, etc.). We consider a periodic function $f(t) = f(t+T)$ with a fundamental frequency $\Omega = \frac{2\pi}{T}$. According to the theory of Fourier, this function can be expressed as an infinite series of sines and cosines. Exploiting Euler's identity $e^{i\varphi} = cos(\varphi) + sin(\varphi)$, each term in the infinite series can be written in its complex form as:

$$f(t) = \sum_{n=-\infty}^{\infty} f_n e^{in\Omega t} \quad (\mathbf{3.21}), \quad \mu\varepsilon\, f_n = \frac{1}{T}\int_{-\frac{T}{2}}^{\frac{T}{2}} f(t) e^{in\Omega t} dt \quad (\mathbf{3.22})$$

In cases where the function f(t) is not periodic, we consider that equations (3.21) and (3.22) hold as T→∞, with the fundamental frequency ν approaching 0. Thus, the term $n\Omega$ for n→∞ becomes a

continuous variable, denoted as ω. Now, by setting the fundamental frequency equal to the finite value of a very small interval Δω, equation (3.22) becomes:

$$f_n \rightarrow \frac{\Delta\omega}{2\pi}\int_{-\infty}^{\infty} f(t)e^{i\omega t}dt = \frac{\Delta\omega}{2\pi}F(\omega)$$

Where

$$\mathrm{F}(\omega) = \int_{-\infty}^{\infty} f(t)e^{i\omega t}dt \quad (\mathbf{3.23})$$

This equation represents the Fourier transform of the function f(t). By applying the same procedure to equation (3.21), we get:

$$f(t) = \frac{1}{2\pi}\int_{-\infty}^{\infty} F(\omega)e^{i\omega t}d\omega \quad (\mathbf{3.24})$$

This equation represents the inverse Fourier transform of f(t), and together with equation (3.23), they are called the Fourier transform pair equations.

A fundamental criterion for the existence of the Fourier transform is that the integral $\int_{-\infty}^{\infty}|f(t)|dt$ converges to a finite value. Additionally, f(t) must have a finite number of extrema within each interval and should not exhibit infinite discontinuities. An additional important property of the Fourier transform is that for an even function f(t), the Fourier transform is an even function and contains only cosine terms, while for an odd f(t), the Fourier transform is an odd function and contains only sine terms.

Furthermore, because the Fourier transform in the general case is a complex function, we can write:

$F(\omega) = Re(\omega) + iIm(\omega) = A(\omega)e^{i\theta(\omega)}$

όπου : $Re(\omega) = \int_{-\infty}^{\infty} f(t)\cos(\omega t)\,dt \quad \kappa\alpha\iota \quad Im(\omega) = \int_{-\infty}^{\infty} f(t)\sin(\omega t)\,dt$

το εύρος της συνάρτησης $A(\omega) = \sqrt{R(\omega)^2 + Im(\omega)^2}$

η φάση $\theta(\omega) = \tan^{-1}\left(\frac{Im(\omega)}{Re(\omega)}\right)$.

3.2.2 Discrete Fourier Transform and FFT

The analytical calculation of the equations of the Fourier transform is difficult, and even more challenging is the computation of the complex integrals that appear in the inverse transform (3.24). Additionally, because the response of the forces we obtain is not a continuous function of time but discrete values in time, the computation of the Fourier transform is done numerically. For numerical solving, the discrete Fourier transform is initially defined, and then the Fast Fourier Transform (FFT) algorithm is applied to accelerate our calculations.

To define the discrete Fourier transform, essentially, we convert integrals into sums. Specifically, we divide our time interval into N equally spaced intervals with a time step of Δt. Thus, we have time $t_m = m\Delta t$, where m = 1...N, and the value for the function $f_m = f(t_m)$. We also define the

total duration of measurements as $T = N\Delta t$ and the period $\Omega = \frac{2\pi}{T}$. Applying these differences to equation (3.23), we have:

$$F_n = F(n\Omega) = \sum_{m=1}^{N} f(t_m) e^{-i(n\Omega)(m\Delta t)} \Delta t \Rightarrow$$

$$\Rightarrow F_n = \Delta t \sum_{m=1}^{N} f_m e^{-\frac{2i\pi mn}{N}} \quad (\mathbf{3.25}), \qquad \mu\varepsilon \ n = 1,2 \dots N$$

The equation (3.25) represents the discrete Fourier transform. Following the same procedure, we obtain the discrete inverse Fourier transform:

$$F_m = \frac{1}{T} \sum_{n=1}^{N} F_n e^{-\frac{2i\pi mn}{N}} \quad (\mathbf{3.26}), \qquad \mu\varepsilon \ m = 1..N,$$

The FFT (Fast Fourier Transformation) algorithm leads us to avoid certain calculations by exploiting the periodicity of the function $e^{i\theta}$. Specifically, we express equations (3.25) and (3.26) in the form:

$$A_m = \sum_{n=1}^{N} B_n W_N^{mn} \ , \ \mu\varepsilon \ \ W_N = e^{-\frac{2i\pi}{N}} \ (\mathbf{3.27})$$

From this equation, we see that N multiplications and N additions of complex numbers are required. Thus, the calculation of all A_m values requires N^2 multiplications. However, by observing the periodicity of the function W_N, we significantly reduce the number of calculations. Specifically, for N data points, $M = \frac{N}{2} log_{2(N)}$ operations are required. For example, for N = 512 data points, initially, N^2 = 262144 multiplications are needed, but with the application of the FFT algorithm, only M = 2304 multiplications are required.

The Fourier transform and the FFT algorithm constitute a mathematical tool that we will use to extract harmonic components when presenting the results. After completing the study of the Fourier transform, we proceed to introduce the model into the software and discretize the field.

3.3 Introduction to Software and Discretization

As we have seen in the equation formulation, the equations of the fluid field are solved numerically. Therefore, the first step we need to take is to define our computational domain and the discretization method. Subsequently, we can perform a grid independence study and conduct a "quality check" for the grid.

Proper and accurate discretization plays a fundamental role in the precision and correctness of our results. A sparse grid with a small number of elements may significantly deviate from the exact solution, fail to converge, or provide a solution with substantial discrepancies. On the other hand, a very dense grid with a large number of elements does not necessarily guarantee good accuracy.

The goal is to construct a grid that is discretized with attention to points of interest and to use grid control criteria that inform us about the quality of the grid we have. This process is further analyzed below.

The grid construction is performed using ANSYS meshing software, and more information about grid elements and discretization methods can be found in the discretization reports [15], [16].

We divide our computational domain into two cylindrical control volumes that surround the propeller. The dimensions of these cylindrical control volumes are chosen to be sufficiently large so as not to affect our solution, including the values of the free flow and the conditions at the inlet and outlet. In the left image of Figure 3.4, the division of the fluid domain into the stationary and rotating control volumes is illustrated. Additionally, we can observe the coordinate system and the dimensions of the grid. In the middle image of Figure 3.4, an image from the grid generation environment of ANSYS is presented. The coordinate system is defined so that the propeller rotates about the y-axis with positive angular velocity. In this image, the two control volumes are in cross-section, and we can discern both the grid elements that discretize our domain and the contact surfaces between the rotating and stationary volumes. In the right image, a detailed view of the discretization around the propeller blades is shown, where we have the highest concentration of elements due to the complex curvature and small dimensions of the edges.

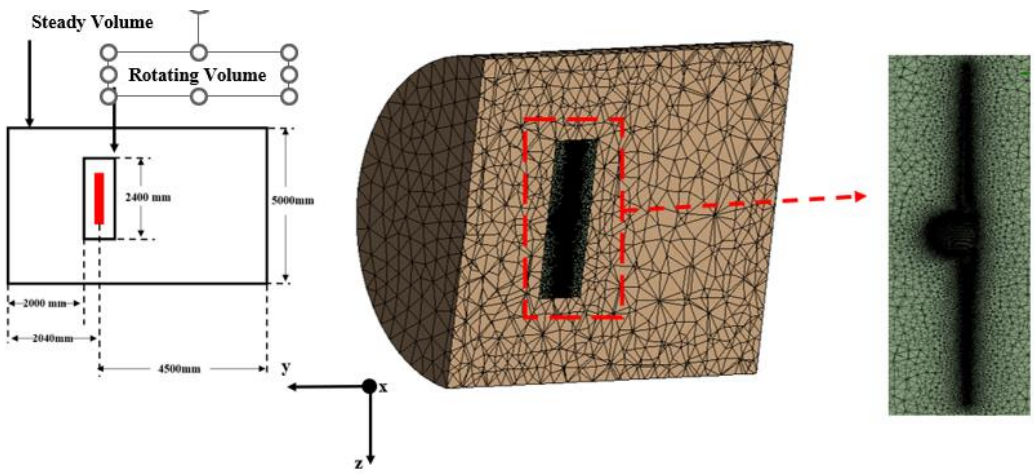

Figure 3. 4 Spatial Discretization grid for the fluid domain

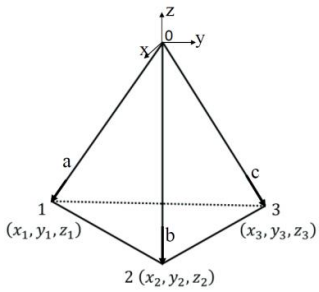

Σχήμα 3. 5 Linear tetrahedral element with 4 nodes

We use linear tetrahedral elements as our discretization elements. The shape of these tetrahedra is presented in Figure 3.5. The term "linear" refers to the number of nodes that the element has along each edge. For linear tetrahedra, we have nodes only at the corners of the element, so we have a total of 4 nodes. The choice of these elements over others (e.g., hexahedra) was primarily made for their ability to discretize complex geometries, thus providing good accuracy. While these elements may not give us a uniformly distributed grid and may increase computational times due to the higher number of elements required, they were the only suitable solution for modeling our geometry because of the small surface area at the "Trailing Edge" of the blades and the abrupt curvatures near the hub of the propeller.

3.3.1 Grid Independence and Quality check

Table 3.1 presents the values of thrust and torque that we calculate for the propeller under two different simulation conditions (flight speed and propeller rotational speed) and for five different mesh sizes. We observe that, as the number of elements increases, for both sets of simulation values, the solution converges to the same value, both for thrust and torque. Since we want our solutions to be satisfactory while also reducing computational costs as much as possible, we choose the third mesh with 1.5 million elements.

Computational cost will play a significant role in the analysis of fluid-structure interaction in Chapter 4, where computational times are particularly long. Therefore, we aim to reduce them through all possible means. The characteristics of the mesh that we will retain for fluid dynamics calculations are presented in Table 3.2.

Table 3. 1 Propeller's Thrust and Moment for 5 grids with different dimensions

GRID INDEPENDANCE							
V/n	15 [m/s] / 1538 [rpm]			V/n	8 [m/s] / 1034 [rpm]		
Grid	Element Num.	Thrust [N]	Moment [Nm]	Grid	Element Num.	Thrust [N]	Moment [Nm]
1	6.00E+05	178.55	36.3	1	6.00E+05	73.6	13.4
2	1.10E+06	205.33	41.98	2	1.10E+06	105.32	19.87
3	1.50E+06	222.13	44	3	1.50E+06	107	20.142
4	2.80E+06	222.07	44.31	4	2.80E+06	108.6	20.92
5	3.70E+06	221.95	44.65	5	3.70E+06	108.01	20.22

Table 3. 2. Number of Nodes and Number of tetrahedral elements for the grid

Nodes Number	$25\ 10^4$
Elements Number	$1.5\ 10^6$

In Table 3.3, you can find the quality coefficients for the mesh quality criteria for the element with the worst behavior regarding each criterion. Specifically, orthogonality of the mesh is defined as the ratio of the angle formed by two neighboring surfaces to an optimal angle. The best quality for this criterion is represented by the value 1. Aspect ratio is defined as how much the elements deviate from having the same length on all sides. Skewness measures how close the mesh elements are to the ideal shape.

In Figure 3.6, the levels of mesh quality are presented for the orthogonality and aspect ratio criteria. We can see that we achieve a good value for both the orthogonality and aspect ratio criteria. For the aspect ratio, the range of values is from 1 to 100, with 1 being the optimal value. Thus, for the value of 8 that we have, we can see that we have achieved good performance for this criterion as well. It's worth noting that the concentration of elements with lower values in Table 3.3 is approximately 2000-3000, which is about 0.3% of the total number of elements. Therefore, we can conclude that the mesh is capable of providing us with good solutions.

Table 3. 3 Quality check criteria values for the grid

Criterion	Value
Orthogonality	Min =0.315

Aspect Ratio	Max = 8
Skewness	Max = 0.65

Figure 3. 6 Grid quality criterion values

Having now formulated the fluid mechanics equations and discretized our computational domain, we can proceed with presenting the results.

3.4 CFD Solution results

As mentioned previously, the primary goal of analyzing the solid propeller model is to monitor the differences in the solution compared to the model in the next chapter. Therefore, in this section, we present and briefly discuss the results, which will be compared with the analysis in Chapter 4. We will present, for four different sets of simulation values, the developing loads and their characteristics in the frequency domain. Additionally, we present the pressure coefficient distributions at a position on the propeller blades for each set of values. The solution of the fluid field is carried out using ANSYS' Fluent software.

3.4.1 Comparison Experimental – Computational Results

Computational Fluid Dynamics (CFD) results require experimental validation to confirm the simulation parameters, design, and algorithms used to solve the flow field. When comparing numerical and experimental solutions, we do not expect identical results but rather small deviations between them. Only then can we conclude that our model is capable of producing good solutions. The comparison is made between simulation conditions that are "simpler" than the conditions introduced for the model analysis.

The experimental data presented here were obtained from reference [14]. This reference, from which the design geometry of the propeller was derived, is related to simulations for a flight altitude of 18 kilometers. The properties of the air at this altitude were extracted from property tables and are presented in Table 3.4. Figures 3.7 and 3.8 show the values for thrust coefficient and power coefficient as a function of the advance ratio for different simulation conditions of airspeed $V_\infty \left[\frac{m}{s}\right]$ and rotational speed n[rpm]. In the labels of these figures, Exp. (Experimental) defines the experimental values for the corresponding velocity. The equations for calculating the dimensionless coefficients and the advance ratio J were presented in section 2.4. Furthermore, Figure 3.9 provides comparison diagrams for thrust (3.9α) and torque (3.9β) generated for different propeller rotational speeds at a free-stream velocity of V_∞ =15 [m/s]. From these four diagrams, we confirm the

functionality of our model, as the errors are evidently minimal. Table 3.5 presents the values of the root mean square error (RMS) for the dimensionless coefficient values for the three free-stream velocities. The root mean square error is defined as.

$$RMS = \sqrt{\frac{\sum_{i=1}^{n}(x_i - y_i)^2}{n}}\ , \qquad where\ n : values\ number$$

With $x_i\ and\ y_i$ representing the experimental and computed values for the same conditions, respectively, we can observe that the largest error is on the order of 0.5%. Larger deviations in values occur at low values of the advance ratio J. In general, however, we can conclude that our model provides satisfactory results, and the errors in comparison are reasonably small.

Table 3. 4 Air properties for altitude = 18 km

Density	$\rho = 0.131266\ \left[\frac{kg}{m^3}\right]$	Temperature	$T = 216.65\ [K]$
Dynamic viscosity	$\mu = 1.422\ 10^{-5}\ \left[\frac{kg}{ms}\right]$	Specific Heat Ratio	$k = 1.4$
Total Pressure	$P = 0.948\ 10^4\ [Pa]$	Sound Velocity	$a = 295.1\ \left[\frac{m}{s}\right]$

Table 3. 5 Root Mean Square error for experimental values model

Value Divergence (RMS)		
V	C_T	C_{Power}
8	0.45435%	0.2191%
12.5	0.3542%	0.10439%
15	0.2483%	0.1502%

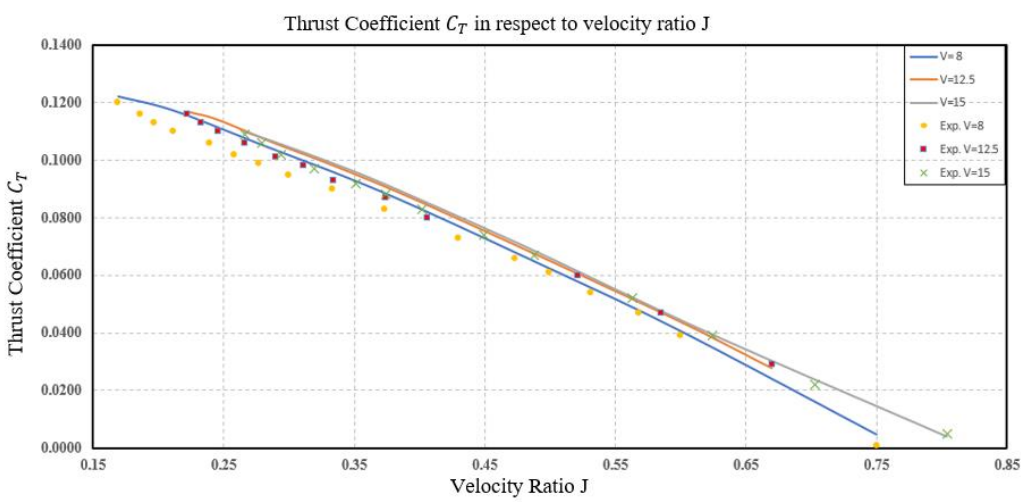

Figure 3.7 Comparison of Experimental Values with Model Values for the Thrust Coefficient as a Function of the Advance Ratio J.

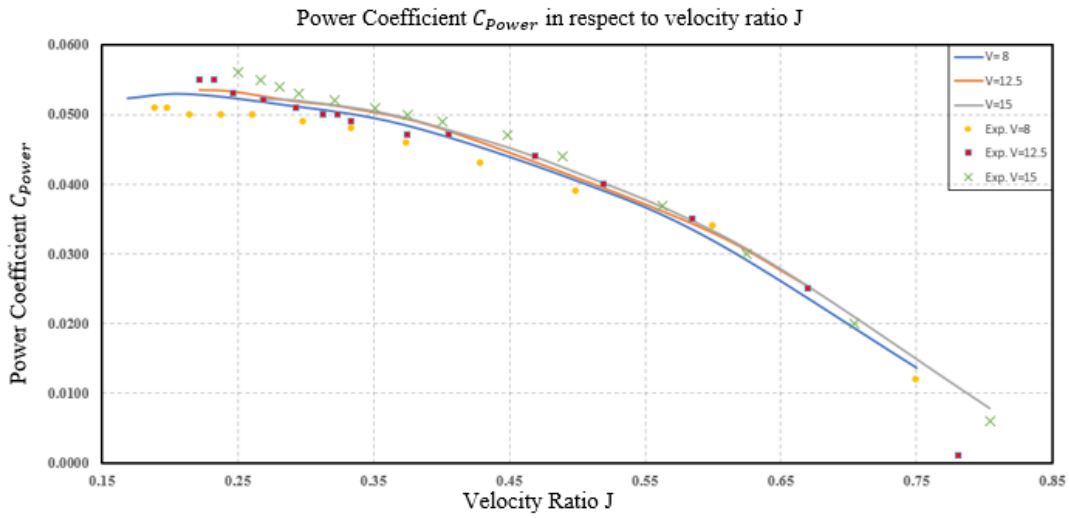

Figure 3.8 Comparison Experimental results versus model results for the power coefficient in respect to velocity ratio J.

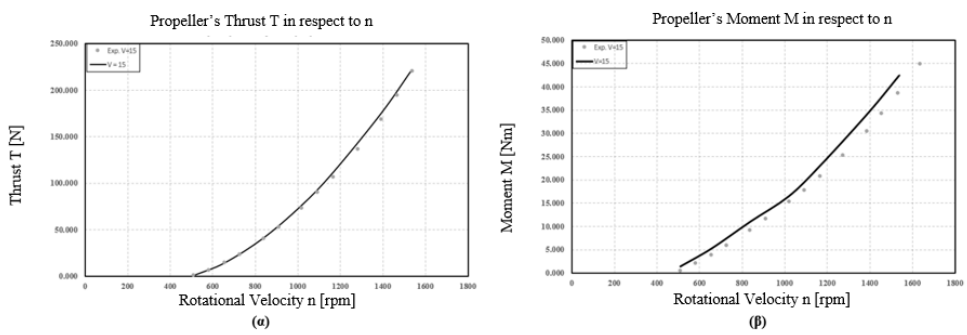

Figure 3. 9 Comparison experimental Results and Computational results Thrust(a) and Moment(β) in respect to propeller's rotational velocity n.

3.4.2 Simulation Conditions

Having validated our computational model, we proceed to define the conditions for which we will solve the flow field. During aircraft flight, the takeoff condition is considered the most demanding. This is due to the higher power provided by the engine (approximately 90% of maximum) and the higher rotational speeds of the propeller. Therefore, during takeoff, we also have the highest dynamic loads on our structure. For these reasons, we choose to solve our model under takeoff conditions.

"For turboprop aircraft with propellers of our dimensions, takeoff occurs at speeds of approximately 45 [m/s] - 60 [m/s]. In addition, the rotational speeds of these engines during takeoff vary widely depending on the aircraft's weight and the number of engines it has. One criterion

mentioned in Chapter 2 and in the introductory part of this chapter was the tip speed of the propellers, which is obtained from the $equation\, V_{R,Tip} = \sqrt{V_0^2 + (\Omega R)^2}$. The choice of sets of values for the simulations should give us such a speed so as not to create areas with Ma>1. Finally, regarding the pitch angle (β) of the propeller, we know that for high rotational speeds (takeoff condition), this angle is small, while for low speeds (flight condition) the angle is larger. Based on all of the above, we choose the 4 sets of values presented in Table 3.6. Because the aircraft is in a takeoff condition, the calculations will be made for flight conditions at sea level. Table 3.7 presents the physical properties of the air at sea level.

Table 3. 6 Value set for operation conditions (Simulation conditions).

	Set 1	Set 2	Set 3	Set 4
Aircraft's velocity	$V = 20\ \left[\frac{m}{s}\right]$	$V = 30\ \left[\frac{m}{s}\right]$	$V = 20\ \left[\frac{m}{s}\right]$	$V = 30\ \left[\frac{m}{s}\right]$
Propeller's rotational speed	$n = 1500[rpm]$	$n = 1500[rpm]$	$n = 2000[rpm]$	$n = 2000[rpm]$
Pitch angle	$\beta = 10°$	$\beta = 10°$	$\beta = 10°$	$\beta = 10°$
Aircraft's Angle of attack (take – off)	$\alpha = 10°$	$\alpha = 10°$	$\alpha = 10°$	$\alpha = 10°$

Table 3. 7 Air properties above sea level

Density	$\rho = 1.225\ \left[\frac{kg}{m^3}\right]$	Temperature	$T = 288.15\ [K]$
Dynamic viscosity	$\mu = 1.789\ 10^{-5}\ \left[\frac{kg}{ms}\right]$	Specific Heat Ratio	$k = 1.401$
Total pressure	$P = 1.013\ 10^5\ [Pa]$	Sound velocity	$a = 304.3\ \left[\frac{m}{s}\right]$

We calculate the J ratio and the Mach number at the tip of the blades for the above sets based on the equations:

$$J = \frac{V_\infty}{nD} \quad , \quad Ma_{Tip} = \frac{V_{R,Tip}}{\alpha} = \frac{\sqrt{V_0^2 + (\Omega R)^2}}{\alpha}$$

- Set 1 : $J = 0.363, \quad Ma_{Tip} = 0.5111$
- Set 2 : $J = 0.545, \quad Ma_{Tip} = 0.5153$
- Set 3 : $J = 0.2727, \quad Ma_{Tip} = 0.6795$
- Set 4: $J = 0.409, \quad Ma_{Tip} = 0.6827$

From these values, we observe that the restriction Ma < 1 is satisfied for all sets of values. Additionally, by examining the coordinates axis of Figures 3.7 to 3.9, which were presented earlier, the calculated values for J fall within the ranges that yield good results from the computational model. Subsequently, for these sets of values, we present the responses of the forces and torques acting on the propeller and analyze them in the frequency domain. Furthermore, we present the distribution of the pressure coefficient at a section of the blades for each set, at a distance of r = 0.75R from the hub of the propeller.

3.4.3 Load response and Spectral analysis

The axis of rotation of the propeller is the y-axis with a positive angular velocity (counterclockwise), the z-axis is directed from the base of the blades towards the tip, and its positive direction is downwards (gravity direction), and the x-axis is positioned in such a way that the right-hand rule is satisfied. The coordinate system is located at the center of the propeller hub, so the forces acting in the plane of the propeller are in the x and z directions. To perform the simulation for the transient phenomenon, we initially solve for the steady state until convergence is achieved (approximately 550 iterations). Then, we perform the transient analysis, starting with a large time step until we reach the step at which we will present our results. Specifically, for all sets of values, the results are presented for a time step such that the propeller rotates by 18° at each step. Thus, for a complete rotation of the propeller, we need 20 time steps.

Initially, in Figure 3.10, we observe the thrust diagrams for the last 3 rotations of the propeller, for each set of values. From this figure, we confirm the convergence of our solution. In Figures 3.11 to 3.14, the responses for each set of values are presented. Specifically, in each figure, we see the response of thrust T, torque about the y-axis, M_y (axis of rotation), and torque about the z-axis, M_z (plane of rotation) for the four sets of values. We choose to present these loads, as they are the most significant among the torques and forces developed in the 3 directions. We are particularly interested in monitoring the behavior of the torque in the plane of rotation and analyzing it in the frequency domain. Only the torque in the z-direction is selected because, due to symmetry, the torque in the x-direction exhibits similar characteristics. Finally, we note that the loads represent the resultant loads on the entire propeller, not on individual blades.

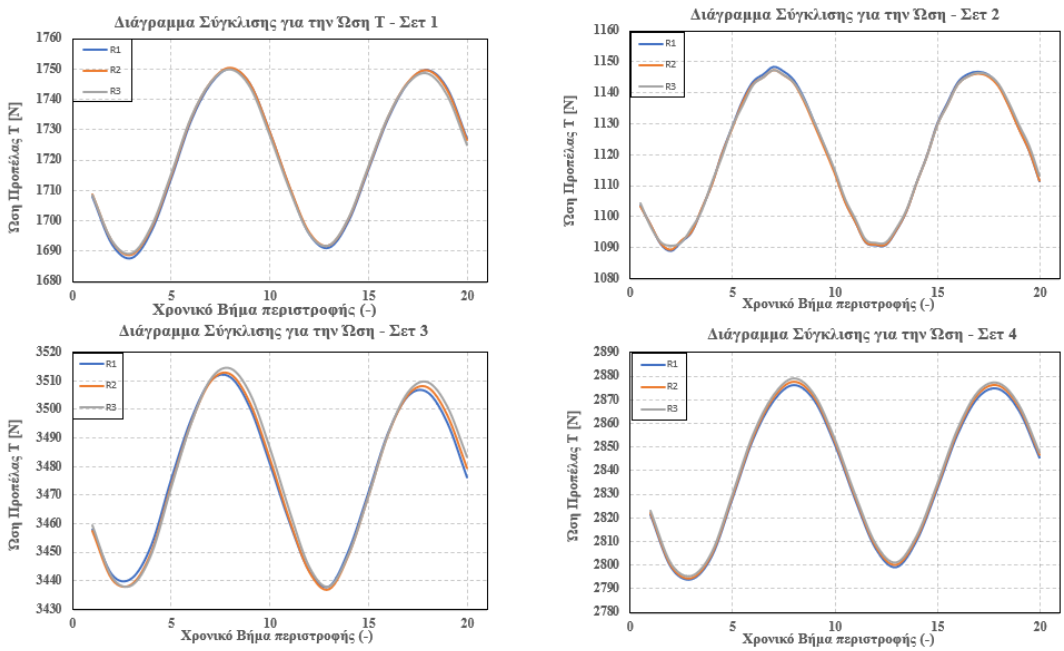

Figure 3. 10 Convergence plots for thrust, for all the value sets, for the 3 last rotations..

From the force responses, we observe that all of them exhibit periodic behavior with twice the frequency of the propeller. The doubling of the frequency is due to simulating the entire propeller, and thus, due to symmetry of the blades, we have the same behavior for forces twice in each

rotation. Between sets 1 and 2, we can see that by keeping the rotational speed of the propeller constant and increasing the free-stream velocity, the produced thrust and developed torques decrease. The same behavior is observed between the simulation values of sets 3 and 4.

Now, comparing the diagrams for the same flight speeds and different propeller rotational speeds, we can see that the loads increase. Specifically, increasing the rotational speed significantly affects the loads compared to increasing the flight speed.

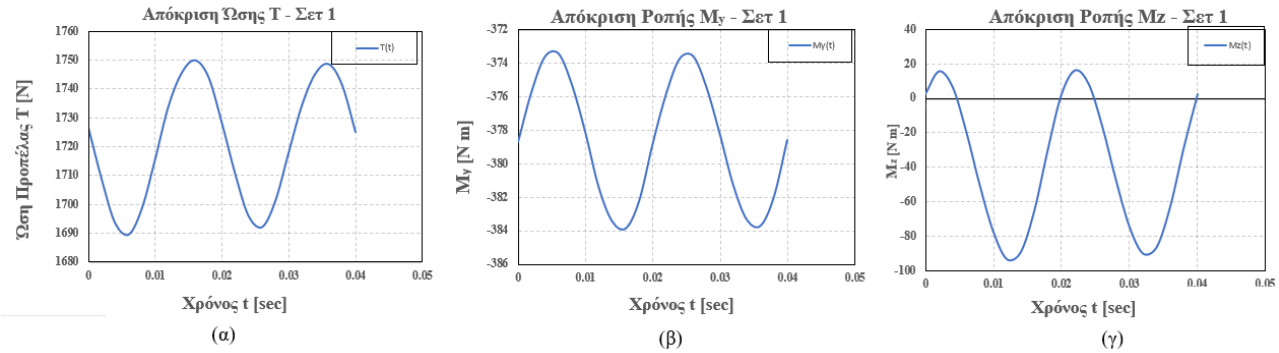

Σχήμα 3. 11. Response (α) Thrust (β) Moment M_y (γ) Moment on the rotation plane M_z for the 1st set.

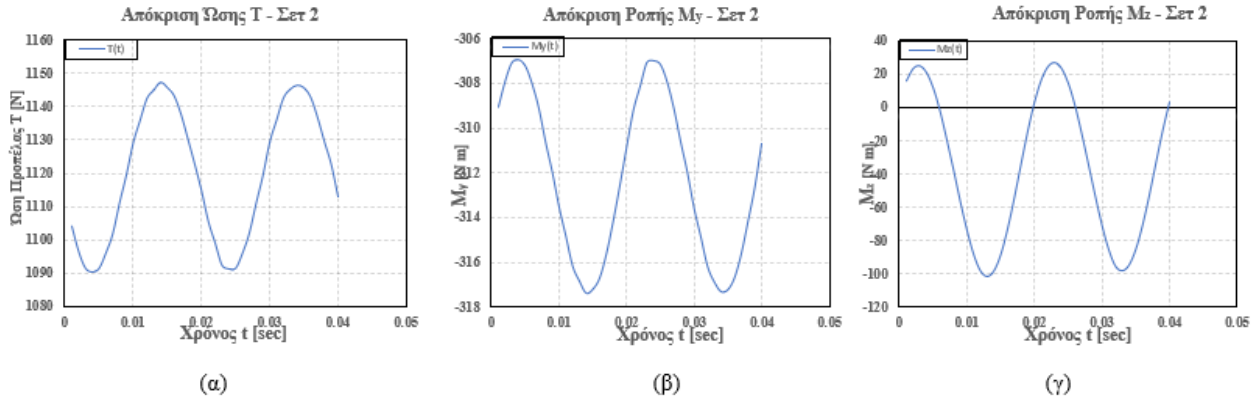

Σχήμα 3. 12 Response (α) Thrust (β) Moment M_y (γ) Moment on the rotation plane M_z for the 2st set.

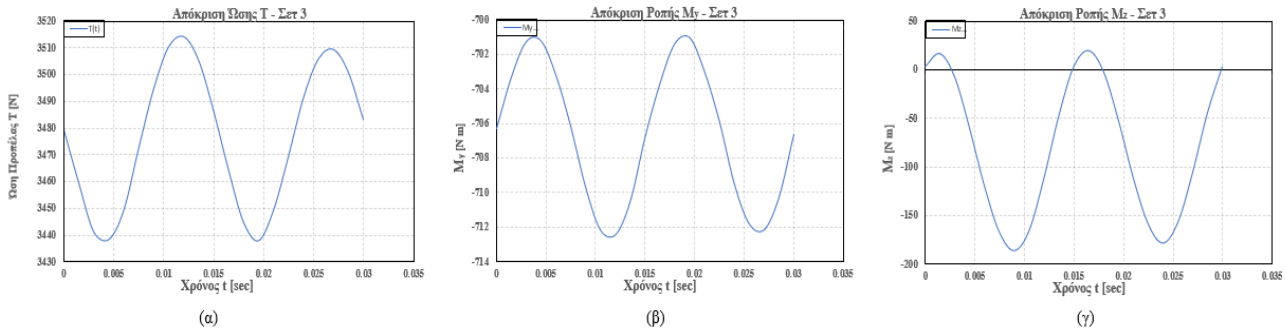

Σχήμα 3. 13 Response (α) Thrust (β) Moment M_y (γ) Moment on the rotation plane M_z for the 3st set.

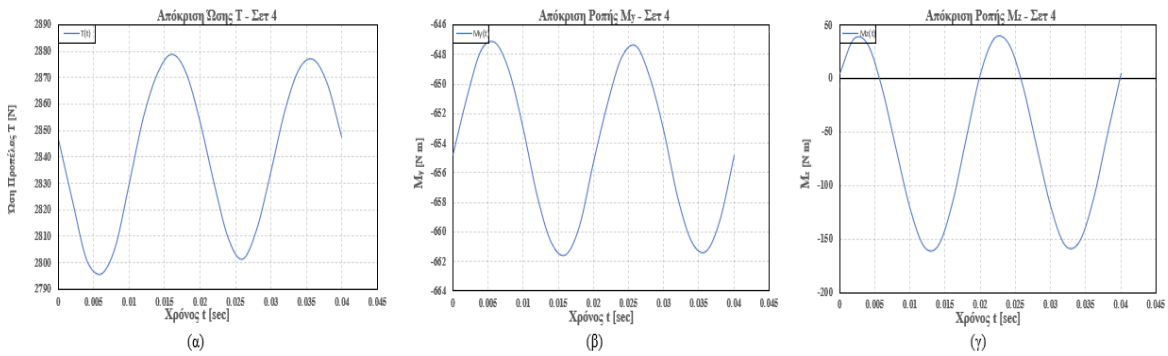

Σχήμα 3. 14 Response (α) Thrust (β) Moment M_y (γ) Moment on the rotation plane M_z for the 4st set.

Fourier analysis for the loads

Applying the Fast Fourier Transform (FFT) algorithm, as presented in section 3.2.2, we extract the harmonic components 0P, 1P, 2P, 3P (P=per propeller rotation) of the total forces. For the first set of values, the FFT algorithm is applied to all forces and torques of the propeller to obtain a general overview of the load behavior. The results are shown in Table 3.8. For the remaining sets of values, the analysis is performed only for thrust and torques in the y and z directions. The results can be found in Table 3.9.

The dynamic loading of the propeller due to torques with vectors in the plane of rotation is of great importance because, besides the large amplitude (for the 2P component), the bending of the propeller in these directions leads to deflection of the hub, which is supported on the reducer. Furthermore, this deflection affects the pitch angle of the propeller and therefore the angle of attack α, which in turn affects the generated thrust. As we will see in the analysis of the 'whirl flutter' phenomenon in Chapter 5, these torques are responsible for instability issues in the propeller.

Observing the values in Table 3.8, we can see that for the harmonic components, the largest oscillation amplitudes occur in the 2P component, as expected due to the symmetry of the blades. Compared to the other two components, the 2P component exhibits oscillations with amplitudes 5-10 times larger. Furthermore, we can observe that the bending loads in the directions within the plane of rotation have significantly larger amplitudes compared to the other loads. These

amplitudes are approximately 2 times the magnitude of the static bending load (in the x and z directions). For these reasons, in the remaining sets of values, we analyze only these two torques and the thrust of the propeller.

In the table, we also distinguish the static load 0P, which somehow carries the average value of the response diagrams we presented earlier. From the values in Table 3.9, we observe the same behavior as in the first set of values, where we see the dominant behavior (in terms of amplitude) of the 2P component for bending M_z compared to the others.

Table 3. 8 Oscillation amplitudes for the harmonic components 1st set.

Oscillation amplitudes for the harmonic components 1st set						
Load	T	F_x	F_z	M_x	M_y	M_z
Component						
0P	1720	7.16	21	37.4	379	37.1
1P	2.38	1.26	2.7	3.8	0.23	5.25
2P	28	21.6	21.3	56.8	5	53.6
3P	4.2	2.7	1.8	6.5	0.7	5.7

Table 3. 9 Oscillation amplitudes for the harmonic components 1st , 2nd and 3rd set

Set	2o			3o			4o		
Load	T	M_y	M_z	T	M_y	M_z	T	M_y	M_z
Component									
0P	1120	312	34.9	3476	706.6	77.8	2839	654.3	77.8
1P	2.7	1.5	6	1.9	0.25	10.3	3.7	0.225	10.3
2P	33	6	62	35.8	5.5	99.7	39.8	7.16	99.7
3P	1.5	0.11	1	4.4	0.7	10	0.18	0.036	10

3.4.4 Pressure Distribution

In Figure 3.15, the distributions of the pressure coefficient C_P are depicted for the 4 sets of values at a distance from the hub of r=0.75R. The figure also indicates which side of the airfoil the points on the diagrams refer to. The upper surface is considered as the surface where the normal vector is in the opposite direction to the velocity vector of the free flow, while the other side of the blades is considered the lower surface. The values of the pressure coefficient were derived from the equation presented in dimensionless coefficients:

- Velocity relative to the airfoil: $V_R = \sqrt{V_0^2 + (\Omega r)^2}$
- Dynamic pressure: $q_\infty = \frac{1}{2}\rho V_R^2 \ \ [Pa]$
- Pressure coefficient: $C_p = \frac{p_1 - p_\infty}{q_\infty}$

The shapes of the diagrams follow the typical pressure distribution patterns on airfoils, and we can observe that as the rotations increase (from sets 1 and 2 to 3 and 4), the pressure distributions become more uniform for each surface.

The results in this chapter, for fluid mechanics analysis, were presented concisely. Our goal was to demonstrate the generation process and the fundamental theory. These results will be put to greater use when compared to the solutions in the fourth chapter.

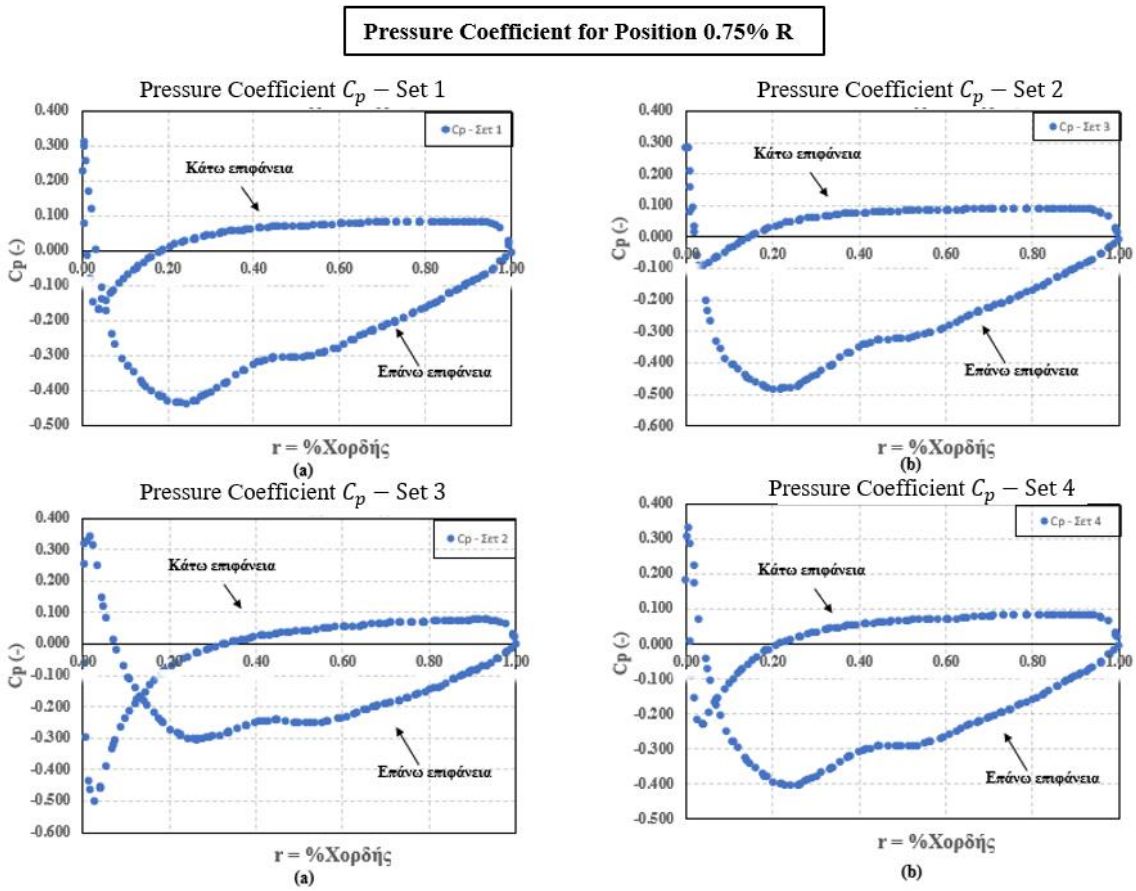

Figure 3.15 Distribution of the Pressure Coefficient at 75% of the Propeller Radius for a Vertical Position of the Propeller

4. AEROELASTIC ANALYSIS OF THE PROPELLER

In this chapter, we now take into account the deformability of the propeller. Based on this consideration, we analyze the phenomena that develop in the fluid-structure interaction (FSI) and compare our results with those of the previous chapter. Initially, we analyze the basic concepts of deformable structures and aeroelastic phenomena. Next, we solve the simplified problem of a rotating beam, which provides us with an initial understanding of the phenomena occurring in geometries like our propeller. We then outline the equations for the fluid and structure, and additionally, we present the methods for discretization (FEM) and numerical solution of these equations. We continue with the description of the co-simulation principles and the method we will use for solving our model. Finally, we conclude with the presentation of the results and the comparison with the solutions from Chapter 3.

4.1 Description of the Problem and Deformable Bodies

Up to this point, we have only studied the fluid mechanics part of our model. Treating the model as rigid, there was no need to describe the phenomena of interaction between the structure and the fluid separately, as both of these problems can be studied independently. In this chapter, we consider the propeller as deformable. This perspective is essential in aircraft design and analysis because the interaction between fluid and structure leads to the development of phenomena of great importance, as we will see later. These phenomena are the primary source of damage for modern aircraft.

From studies on Fluid-Structure Interaction (FSI) systems, we have observed that the structure and the surrounding fluid field are strongly coupled. Due to this interaction, a cyclic exchange of information occurs between these two fields. The quantities in the fluid field affect the behavior of the structure, and this behavior, in turn, affects the fluid field. From experiments and studies conducted in the past, we have found that this interaction can either stabilize into a steady state, dampen (stability), or increase over time (instability). A phenomenon of dynamic instability arising from the deformability of the structure is studied in Chapter 5.

By introducing deformability into the structure, we greatly increase accuracy, albeit at the cost of increased complexity.

Let's then wonder, what is a deformable body, and what are its differences from a solid (rigid) one?

A solid body is defined as a body in which the relative distance between its points remains unchanged over time, and its motion can be regarded as a combination of translational and rotational components. For solid bodies, deformation is either non-existent or small enough to be considered negligible (relatively rigid), regardless of the external forces and torques acting on it. In general, solid bodies have six degrees of freedom, consisting of three translational (x, y, z) and three rotational (correspondingly x, y, z) degrees of freedom. For solid bodies, the equations of motion are composed of ordinary differential equations and can be solved either analytically (for linear systems) or numerically (for non-linear and multi-body systems).

A deformable (elastic) body is defined as a body in which the relative distance between two of its points changes over time (deformation) due to external forces. For small deformations and linear material behavior of the body, we consider it as linearly elastic. However, for large deformations or non-linear material properties, it becomes non-linearly elastic. The variables describing deformable bodies have both spatial and temporal dependencies. The description of the body's behavior is based on the field of "Elasticity Theory," which formulates the equations governing the problem and calculates the body's behavior for different conditions.

"Elasticity Theory" and "Fluid Mechanics" are branches of a broader field called "Continuum Mechanics." According to the theory of elasticity, describing a deformable body requires solving 15 equations with 15 unknowns, which will be defined along the way for each point on the body. The resulting system of equations consists of partial differential equations with both temporal and spatial dependencies. Few problems with simple geometries have analytical solutions, so we often resort to solving them using numerical methods.

In the following analysis, we study the fluid mechanics and structural problems as interdependent, aiming to track the influence of one field on the other. Subsequently, we describe the theory of aeroelasticity.

4.2 Aeroelasticity

Aeroelasticity is the term we use to define the scientific field that deals with the interaction between the deformation of a structure within a fluid (air) environment and the aerodynamic forces acting on that structure. Primarily, the application of aeroelastic analysis is related to aircraft, but it also finds applications in buildings, marine vehicles, automobiles, and more. Figure 4.1 presents a schematic representation of the field of aeroelasticity. In this figure, we observe the interactions between three different fields: dynamics, aerodynamics, and elasticity.

Aerodynamics involves the calculation of forces acting on a body of specific geometry. Elasticity, as mentioned earlier, deals with calculating the shape of an elastic body subjected to specific loads. Meanwhile, dynamics introduces the phenomena that arise when considering inertial forces.

From the intersections of the circles in the diagram, we can see the scientific fields that study the interactions of these three fundamental principles. The problem we are studying falls within the intersection of all three circles, known as "Dynamic Aeroelasticity," as we investigate the influence of non-steady aerodynamic forces on the elastic behavior of the structure, characterized by the oscillatory behavior of its modes. The subsequent sections present the basic static and dynamic aeroelastic phenomena.

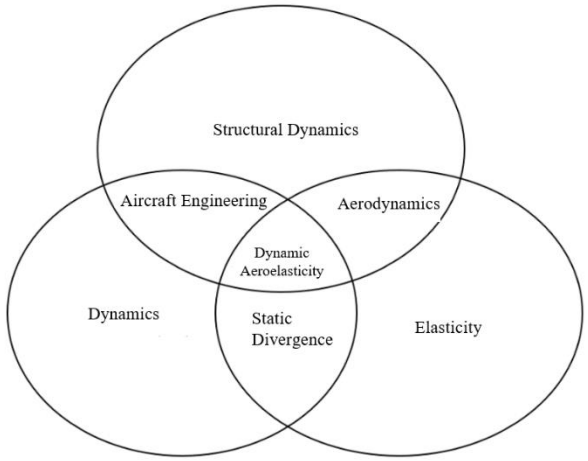

Figure 4. 1 Schematic representation of the science of aeroelasticity and the various fields that comprise it [11].

Static Aeroelastic Phenomena

Static aeroelastic phenomena involve the interaction of steady (time-independent) aerodynamic forces with the elastic forces of the structure. The static deformation of the structure leads to a redistribution of loads and related phenomena. Static aeroelasticity mainly influences small aircraft. The phenomena related to this field include the following:

1) Torsional divergence
2) Control surface reversion

In summary, during static divergence, static loads cause deformation of the structure, which, in turn, affects these loads. The resultant force from the aerodynamic loads and elastic forces determines the extent of load redistribution. Static divergence refers to the critical condition in which, due to the aforementioned behavior, the inertial elastic forces of the structure do not balance with the aerodynamic forces, which can lead to structural failure.

During control surface reversal, the aircraft loses its ability to maneuver or turn. In this phenomenon, due to load redistribution, the structure deforms, resulting in forces from the airfoil and control surface of equal magnitude and opposite direction. This loss of control capability can be detrimental to the aircraft..

Dynamics of Aeroelastic Phenomena

The dynamic aeroelasticity is attributed to the interaction of non-permanent aerodynamic forces, elastic forces, and inertial forces. These phenomena are critical for aircraft certification. Subsequently, the fundamental dynamic phenomena are presented, for some of which we use the English terminology used in the global literature:

1) Flutter
2) Buffeting

3) Aeroelastic Response to Dynamic Load

Flutter

Flutter is a critical aeroelastic phenomenon characterized by self-excited oscillations that occur when a disturbance in the aeroelastic system generates aerodynamic forces. Energy is supplied by the airflow. When an aircraft operates at critical flutter speeds (J), phase synchronization between the structural motion of the aircraft and the loads it experiences allows the system to extract energy equal to the energy dissipated internally within the structure. This results in a stable periodic motion of the system. For speeds below the critical threshold, this disturbance is damped out, and the system remains stable. However, at speeds above the critical threshold, the disturbance amplifies, and the motion becomes unstable.

The amplitudes of the self-excited oscillations in flutter theoretically can become unlimited. The principle of flutter is illustrated in Figure 4.2. In this figure, you can see the displacements of a simplified airfoil with two degrees of freedom (either a wing or an aileron) during one oscillation cycle. The figure also depicts the energy of the system for each position of the airfoil.

In Figure 4.2a, the case is shown in which the torsional and bending displacements of the airfoil are in phase. In this situation, the total energy over one cycle of motion is zero, and flutter does not occur. Conversely, in Figure 4.2b, the two degrees of freedom are out of phase by π/2. The total energy of the structure over one cycle of motion is positive, and flutter can occur. Specifically, you can observe that the bending deformation is excited through the torsional deformation.

Flutter is a critical concern in aerospace engineering, and understanding its mechanisms and how to mitigate it is crucial for the safety of aircraft and other aeroelastic structures.

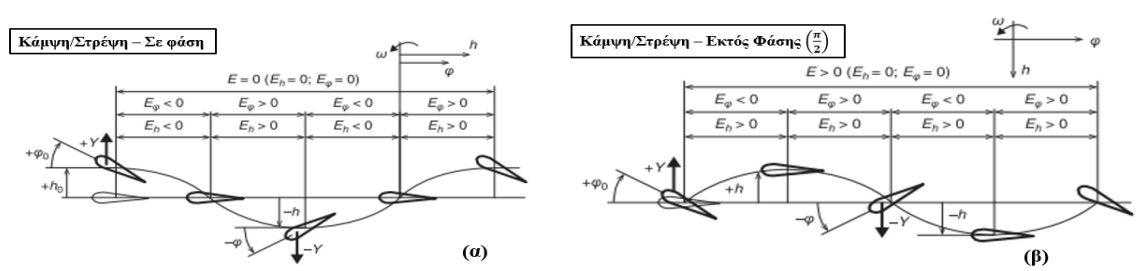

Σχήμα 4. 2 Harmonic motion of an airfoil with 2 degrees of freedom (a) Bending/Torsion in phase (b) Bending/Torsion out of phase by π/2.

The remaining dynamic aeroelastic phenomena are presented briefly. Buffeting is the phenomenon caused by the vortex shedding that occurs at the aerofoil trailing edge during operation. It is usually estimated using stochastic or experimental methods. As for aeroelastic response to dynamic loading, we refer to the response of deformable structures to non-permanent aerodynamic forces, which can lead to the flutter phenomenon. Another critical condition for aeroelastic response that can be observed is the synchronization of the structure with the forces applied to it. In this chapter, we deal with this aspect of the problem. All the phenomena presented up to this point, once they exceed their critical limits, lead us to instability. It is very important to always keep in mind the following distinction between the phenomena that arise :

"Typically, resonance response is ideally considered as the excitation of a structure at one or more of its natural frequencies by an external source of energy, whereas conversely, an unstable response is regarded as arising in a structure from an internal source of energy."

In general, every new aircraft design can potentially introduce new aeroelastic phenomena. A classic example is the 'whirl flutter' phenomenon, which emerged in turboprop engine constructions around 1950. More about this phenomenon will be presented in the next chapter, where a parametric study of the stability boundaries of 'whirl flutter' will be conducted for our propeller. Detailed descriptions of all aeroelastic phenomena can be found in references [9] and [11].

4.3 Rotational Beam

Due to the significantly greater length dimension of the propeller blades compared to other dimensions, we can initially simplify our model by considering the propeller blades as rotating one-dimensional beams. This simplification allows us to observe the fundamental characteristics that govern models like ours. This simplification will facilitate the understanding of the more complex propeller problem later on. Thus, for the rotating beam, we study the bending deformations in directions perpendicular and tangential to the rotation plane.

The primary difference between rotating beams, as opposed to non-rotating ones, is that they operate under the influence of a centrifugal force field (centrifugal/centripetal), which depends on the length of the beam, the rotational speed, and mass. The centrifugal force, in vector form, can be expressed as the product of the mass of the body and the centrifugal (opposite centripetal) acceleration:

$$\underline{f_c} = m\underline{a_c}\,, \qquad \text{Centripetal acceleration}: \; a_c = -\underline{\omega} \times \left(\underline{\omega} \times \underline{r}\right)$$

Where $\underline{r}$, $\underline{\omega}$ The radial distance of the body from the axis of rotation and its angular velocity, respectively.

For our beam, which rotates about the z-axis (ω=Ω_e_z), and bends in the plane of rotation and perpendicular to it, the position vector of a random point in space will have the equation: $\underline{r} = (x + u_x)\underline{e_x} + u_y\underline{e_y} + u_z\underline{e_z}$, with respect to a coordinate system fixed to the beam, where the x-axis is its longitudinal axis. The quantities u_x, u_y, u_z refer to the deformations in the x, y, z directions, respectively. For the above vector relationship, we assume that the dimensions in the y and z directions are much smaller than in the x direction. Thus, based on the above vector relationship, the centrifugal force for this point is calculated as:

$$\underline{f_c} = m\Omega^2\left((x + u)\underline{e_x} + u_y\underline{e_y}\right)$$

From the last equation, we can see that we only consider components along the axes defining the plane of rotation.

In Figure 4.3α, a rotating beam is depicted undergoing vertical bending in the plane of rotation. It has a distributed axial load $f_x(x,t) = m\Omega^2(x + u_x)\underline{e_x}$, which results from the centrifugal force and leads to the development of tensile forces N. Additionally, we observe the distributed lateral

external load $f_z(x,t)$. The beam rotates about the z-axis. In Figure 4.3β, we see an infinitesimal segment of the beam at a random position x and the forces acting on it.

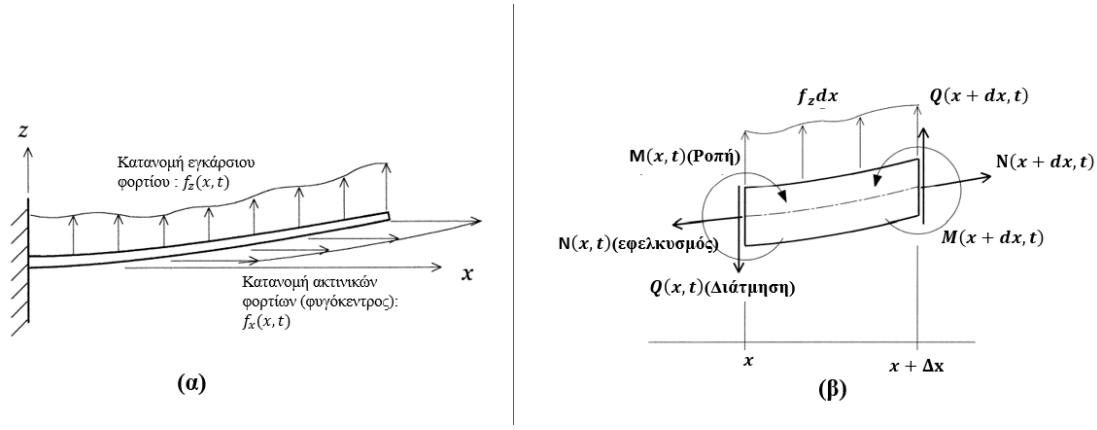

Figure 4. 3 (α) Rotating beam with distributed loads. (β) Infinitesimal beam segment. [6]

Due to the small dimensions of the beam in the y and z directions (compared to x), the displacements are functions only of the distance x (u_x(x, t), u_y(x, t), u_z(x, t)). A simplifying assumption of great significance introduced into the problem is that of small deformations of the beam. If we were to formulate the problem for large deformations, we would have nonlinear terms in the final equations of motion and coupling of different problems (bending, axial, etc.). The solution to the beam problem for large deformations can be found in reference [3]. Of course, this simplification may reduce the accuracy of our model, but in this chapter, we simply want to present the differences in the final equations for rotating beams compared to classical beams.

For the formulation of the equations of motion describing the rotating beam, the following assumptions are made :

- • The longitudinal axis Ox of the beam connects the geometric centers of its cross-sections. That is :

  $$\int_A y dA = \int_A z dA = 0$$

  Also, the transverse axes Oy and Oz are principal axes of the surface inertia, so $\int_A yz dA = 0$.

- Kirchhoff's assumption: The cross-sections of the beam that are perpendicular to the longitudinal axis Ox in the undeformed state remain flat and perpendicular to the deformed axis Ox. Additionally, they exhibit a small transverse displacement w(x,t), which is small compared to the dimensions of the cross-section.

- The material of the beam is linearly elastic, meaning it follows Hooke's law.

Additionally, we assume that the material's modulus of elasticity and the cross-sectional area of the beam remain constant along the entire length of the beam. From the second assumption, we have that the shear force is zero. Thus, it follows.

$$\gamma_{xz} = \frac{\partial w}{\partial x} + \frac{\partial u}{\partial z} = 0 \Rightarrow u = u_o(x,t) - z\frac{\partial w}{\partial x}(x,t)$$

So, for axial deformation we have : $\varepsilon_x = \frac{\partial u}{\partial x} = u_o' - zw''$ $(\mathbf{4.1})$. Writing Hooke's law for axial stress in the x-direction, we have : $\sigma_x = E\varepsilon_x \overset{(4.1)}{\Longrightarrow} \sigma_x = E(u_o' - zw'')$. These stresses are calculated for the stationary beam. In this state, there is no development of the inertial force $f_x(x,t)$, resulting in zero axial forces. Thus, using Hooke's law, we have:

$$N = \int_A \sigma_x \, dA = E \int_A u_o' \, dA - E \int_A zw'' \, dA$$

Based on the first assumption, the second integral becomes zero. Furthermore, due to the zero axial force, we finally obtain ($u_o' = 0$). Thus, the stresses in the x-direction are calculated from the equation:

$$\sigma_x = -Ezw'' \ (\mathbf{4.2})$$

The moment about the center of the cross-section of the beam resulting from the sum of the stresses (σ_x) is calculated using the equation:

$$M_y = \int_A \sigma_x z dA \xRightarrow{1^{\eta} \upsilon\pi\acute{o}\theta\varepsilon\sigma\eta \ \kappa\alpha\iota \ (4.2)} M_y = -EIw''$$

Where I is the surface moment of inertia for the cross section in respect to axis Oy : $I_y = \int_A z^2 dA$.

For the rotating beam, the axial load observed in Figure 4.1β arises from the distribution of $(f_x(x,t)$) illustrated in Figure 4.1α. As we demonstrated earlier, this component of the centripetal force has the equation ($f_x(x,t) = m\Omega^2(x + u_x)$. Due to small displacements, the axial load originates from the component of the centripetal force in the x-direction. Additionally, because $(x \gg u_x)$, the displacement (u_x) is considered negligible in the above expression. Thus, the axial load acting on the body is calculated by the integral :

$$N(x) = \Omega^2 \int_x^L m(x_1) \, dx_1 \xRightarrow{m(x_1)=\rho A x_1} N(x) = \Omega^2 \rho A \int_x^L x_1 \, dx_1 \quad (\mathbf{4.3})$$

The limits of the integral are due to the fact that at the free end of the beam (\(x=L\)), the axial load becomes zero.

Based on the equilibrium equation of the diagram in Figure 4.3β, we apply the equilibrium condition with respect to the z-axis, and thus we obtain:

$$Q(x+\Delta x,t) - Q(x,t) + N(x+\Delta x,t)\frac{\partial w}{\partial x} - N(x,t)\frac{\partial w}{\partial x} + f_z(x,t)\Delta x = (\rho A \Delta x)\frac{\partial^2 w}{\partial t^2} \quad (\mathbf{4.4})$$

In this equation, the terms involving the force N∂w/∂x represent the vertical component of the centrifugal force, which develops due to rotation. By expanding the terms Q(x+Δx,t) and N(x+Δx,t) in a Taylor series, we have.

$$Q(x+\Delta x,t) = Q(x,t) + \frac{\partial Q(x,t)}{\partial x}\Delta x + OAT(\Delta x^2)$$

$$and\ N(x+\Delta x,t) = N(x,t) + \frac{\partial N(x,t)}{\partial x}\Delta x + OAT(\Delta x^2)$$

By substituting these relationships into equation (4.4) and dividing by Δx, we obtain :

$$Q' + \frac{\partial}{\partial x}\left(N\frac{\partial w}{\partial x}\right) + f_z(x,t) = \rho A\frac{\partial^2 w}{\partial t^2} \quad (\mathbf{4.5})$$

Now, equating the moments in the y-direction, we have: $\Sigma M_y = \Delta I_y \ddot{\varphi}$, where φ is the angle formed by the axis of the beam with the x-axis,

$$\tan(\varphi) = -w'(x,t) \Rightarrow \ \varphi \ \approx -w' \quad (\mathbf{4.6})$$

Due to small slopes of the beam. Furthermore, the mass moment of inertia of the beam segment, after integration, is obtained as follows:

$$\Delta I_y = \rho I_y \Delta x$$

So, the equilibrium equation becomes :

$$M(x+\Delta x,t) - M(x,t) - Q(x+\Delta x,t)\frac{\Delta x}{2} - Q(x,t)\frac{\Delta x}{2} = \rho I_y \Delta x(-\ddot{w}')$$

Expanding the terms of the forces in a Taylor series, as before, and retaining terms up to the first order, and substituting the equations derived in the last equation, we obtain:

$$Q = \frac{\partial M}{\partial x} = -(EIw'')' \ (\mathbf{4.7})$$

Substitution of (4.7) into (4.5) give us :

$$-(EIw'')' \ + \frac{\partial}{\partial x}\left(N\frac{\partial w}{\partial x}\right) + f_z(x,t) = \rho A\frac{\partial^2 w}{\partial t^2} \ \Rightarrow$$

$$\Rightarrow \rho A\frac{\partial^2 w}{\partial t^2} + (EIw'')'' - \frac{\partial}{\partial x}\left(N\frac{\partial w}{\partial x}\right) = f_z(x,t)$$

$$\Rightarrow \rho A\frac{\partial^2 w}{\partial t^2} + (EIw'')'' - \Omega^2\frac{\partial}{\partial x}\left(\rho A\frac{\partial w}{\partial x}\left(\int_x^L x_1\, dx_1\right)\right) = f_z(x,t)(\mathbf{4.8})$$

The above equation is a partial differential equation of the 4th order with respect to space and the 2nd order with respect to time. Its solution requires 2 initial conditions and 4 boundary conditions, which depend on how the beam is supported.

For equation (4.8), we first separate the variables by assuming that \(w(x,t) = X(x)T(t)\). Then, we demonstrate the orthogonality property of the eigenfunctions \(X(x)\), which is formulated as:

$$\int_0^L mX_r(x)X_s(x)dx = \delta_{rs} \ \ (\mathbf{4.9})$$

After establishing the eigenproblem, we know that, according to the eigenfunction expansion theorem, any function f(x) that satisfies the homogeneous boundary conditions of the system can be expressed as an absolutely and uniformly convergent infinite series of the form:

$$f(x) = \sum_{n=1}^{\infty} a_n X_n(x),\ where\ X_n(x)\ is\ the\ eigenmodes$$

For this reason, the beam's response can be written as:

$$w(x,t) = \sum_{n=1}^{\infty} \tau_n(t) X_n(x) \quad (\mathbf{4.10})$$

where, Using the orthogonality conditions, the coefficients of the infinite series are determined by the equation:

$$\tau_n(t) = \int_0^L \rho A X_n(x) w(x,t) dx \quad (\mathbf{4.11})$$

Now, by substituting equation (4.10) into the motion equation (4.8), multiplying the equation by the eigenfunction X_n, integrating it over the entire length of the beam, and applying the relationship (4.11), after some calculations, we obtain:

$$\rho A \ddot{\tau}_n(t) \int_0^L X_n^2(x) dx + \left\{ EI \int_0^L \left(X_n''(x)\right)^2 dx + \Omega^2 \rho A \int_0^L \left[\left(X_n'(x)\right)^2 \int_x^L x_1\, dx_1 \right] dx \right\} \tau_n(t)$$
$$= \int_0^L X_n(x)\, f_z(x,t) dx \quad (\mathbf{4.12})$$

Using the definitions:

$$Beam's\ Mass: M_n = \rho A \int_0^L X_n^2(x) dx\ ,$$

$$K_{Sn} = EI \int_0^L \left(X_n''(x)\right)^2 dx$$

$$K_{CF_n} = \rho A \int_0^L \left[\left(X_n'(x)\right)^2 \int_x^L x_1\, dx_1 \right] dx\ , \qquad \Xi_n(t) = \int_0^L X_n(x)\, f_z(x,t) dx$$

Equation (4.12) takes the compact form of the motion equation for the beam:

$$M_n \ddot{\tau}_n(t) + \left[K_{S_n} + \Omega^2 K_{CF_n}\right] \tau_n(t) = \Xi_n(t) \quad (\mathbf{4.13})$$

In the above equation, the terms $(K_{S_n})\ and\ (K_{CF_n})$ represent the generalized stiffness of the structure and the generalized centrifugal stiffness, respectively. It is important to emphasize that neither of the two stiffness terms, when applied individually, satisfies the orthogonality conditions. However, if they are applied together in combination with an appropriate value of the angular velocity \(\Omega\), then the orthogonality conditions are satisfied. The system of equations (4.13)

constitutes a system of second-order ordinary differential equations. At this point, we are not interested in solving the system but in observing its characteristics in a state of free oscillation. From equation (4.13), we can easily see that the natural frequency (ω_n) of the n-th mode of the system is obtained, after first dividing by the mass M_n. Thus, we have:

$$\omega_n^2 = \left[\frac{K_{S_n}}{M_n} + \Omega^2 \frac{K_{CF_n}}{M_n}\right] = \omega_{NR}^2 + \Omega^2 K_{w_n} \quad (\mathbf{4.14})$$

The term (ω_{NR_n}) represents the n-th natural frequency of the non-rotating system, while the term (K_{w_n}) is an additional term that takes into account the increase in stiffness due to the centrifugal force (gyroscopic stiffening) and is often referred to in the literature as the "Southwell coefficient." This coefficient serves as a measure of how quickly the natural frequency of the structure increases with the rotation frequency of the propeller. A more detailed derivation of the equations for the bending problem of a simple beam can be found in reference [2], while for the rotating beam problem, it can be found in reference [6].

Thus, we have arrived at the most significant result of this section. While we generally know that the natural frequencies depend only on the characteristics of the oscillator, the above equation shows us that they are also influenced by the rotational speed of the structure. Furthermore, we observe that due to the centrifugal force, there is an increase in the stiffness of our structure in a direction perpendicular to the plane of rotation.

Equation (4.8) is considered as the equation for flapwise bending, i.e., bending perpendicular to the plane of rotation. By following the same procedure used to derive this equation, we can also derive the equation for edgewise bending, which is bending within the plane of rotation. The difference between the two equations arises from the component of the inertial centrifugal load in the y-direction, $f_{cy}(x,t) = m\Omega^2 u_y$. This component is due to the deformation $v(x,t)$ in the y-direction and can be expressed as$f_{cy}(x,t) = m\Omega^2 \frac{\partial v}{\partial x}(x,t)$.. By adding this term and replacing the displacement \(w\) with the displacement v, we obtain:

$$\rho A \frac{\partial^2 v}{\partial t^2} + (EIv'')'' - \Omega^2 \rho A \frac{\partial}{\partial x}\left(\frac{\partial v}{\partial x}\left(\int_x^L x\, dx\right)\right) - \Omega^2 m \frac{\partial v}{\partial x}(x,t) \quad = f_y(x,t) \; (\mathbf{4.15})$$

Applying the same procedure that we used for Equation (4.8), we arrive at an expression for the natural frequencies of the structure:

$$\omega_n^2 = \omega_{NR_n}^2 + \Omega^2 K_{v_n} \quad \text{όπου } K_{v_n} = K_{w_n} - 1$$

Where ω_{NR_n} is the natural frequency of the non-rotating system and K_{v_n} is the stiffness increase factor due to centrifugal forces. We can observe that stiffness increases due to rotation, even in the y-direction in the plane of rotation (edgewise). However, in this case, the coefficient is smaller by one unit than the previous one.

As we will see later, this behavior during the dynamic analysis of structures should be taken into account to avoid the structure operating under conditions where there is a risk of resonance with the load. One way to observe the correlation between the frequencies of harmonic loads on rotating bodies and the natural frequencies of the structure is the Campbell diagram, which is presented below.

4.3.1 Campbell Diagram

Such a diagram represents the frequency response of a system as a function of its oscillatory behavior. Specifically, it shows how the natural frequencies of each mode of vibration for a structure change with the rotational speed of the structure. The Campbell diagram finds applications in structures that rotate at high speeds, such as helicopter rotors, turbomachinery, turboprop engines, and more.

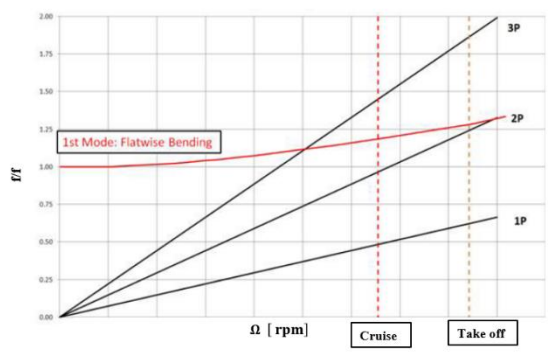

Figure 4. 4 Campbell Diagraml

A typical diagram of this kind is presented in Figure 4.4. On the ordinate axis are the normalized frequency values, and on the abscissa axis are the rotational speeds of the propeller. This diagram depicts the relationship of only the first natural frequency, as the others have values that exceed the limits of the chart. We can observe that the 2P harmonic component, for rotational speeds slightly higher than the takeoff speed, is equal to the frequency of the first mode. Therefore, based on the information from the diagram, we should either avoid operating within the ranges of these values or, during design, modify the characteristics of our structure to avoid this resonance. Typically, in rotating structures where there is a risk of resonance, permissible limits are provided that should not be approached by the operational rotational speeds of the propeller.

Having described the simplified model and understood the phenomena that occur in rotating structures, we proceed with the formulation of the equations for our propeller.

4.4 Formulation of equations

For the formulation of equations, we need to consider both the fluid system and the structural system. For the fluid system, we require equations that govern the behavior of the fluid field. Additionally, for the structural system, we need equations that express the variables for our deformable structure. In this section, we will develop these two systems.

We are aware that the response of a continuous medium is generally given by the solution of the partial differential equation:

$$Lu(\underline{r},t) + m(\underline{r})\ddot{u}(\underline{r},t) = f(\underline{r},t) \quad ,\underline{r} \in S \quad (\mathbf{4.16})$$

Where u is the generalized deformation at the point of the body with the position vector $\underline{r}$, m is the scalar mass distribution function, L is the stiffness operator, and f is the external load. The analytical solution of (4.16) is feasible only for simple geometries and simple boundary conditions, and therefore, it is solved numerically. To transform this equation into a solvable form, a geometric discretization process is required. This is achieved using the Finite Element Method (FEM). Using this method and subsequently applying the Galerkin method, we generate the equations of motion, which are solved to calculate the behavior of our structure.

Subsequently, the three-dimensional theory of elasticity is presented, and the system of equations in the form (4.16) for rotating bodies is derived. After this is accomplished, we use the above-mentioned methods to generate the equations of motion for the model. The principles of three-dimensional elasticity and inertial characteristics, which will be used for formulating these equations, are based on references [1], [2], [4], and [5].

4.4.1 Three-dimensional elasticity theory for Rotating Structures

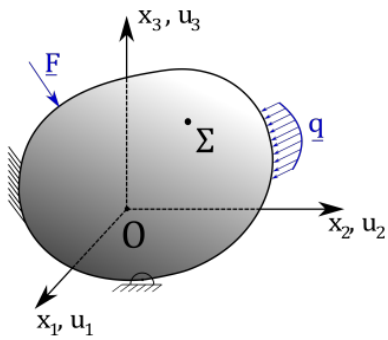

Figure 4. 5 Flexible body with arbitrary geometry

During the formulation of the equations, we are referring to the rotating system attached to our body. Figure 4.5 presents a deformable solid of arbitrary geometry and orientation, subjected to an external force and distributed load. The displacements at each point in the body have both temporal and spatial dependence, denoted as $u = u(x_1, x_2, x_3, t)$. For this body, the quantities of modes ε_{ij} and stresses σ_{ij} are defined. Our goal is to calculate the tensors for these quantities. The tensors are defined as follows:

$$[\varepsilon_{ij}] = \begin{bmatrix} \varepsilon_{11} & \varepsilon_{12} & \varepsilon_{13} \\ \varepsilon_{21} & \varepsilon_{22} & \varepsilon_{23} \\ \varepsilon_{31} & \varepsilon_{32} & \varepsilon_{33} \end{bmatrix}, \quad [\sigma_{ij}] = \begin{bmatrix} \sigma_{xx} & \tau_{xy} & \tau_{xz} \\ \tau_{yx} & \sigma_{yy} & \tau_{yz} \\ \tau_{zx} & \tau_{zy} & \sigma_{zz} \end{bmatrix}$$

The terms within the matrices above, for small deformations and linear elastic material, are calculated using the following relationships:

Normal strains: $\varepsilon_{ii} = \frac{\partial u_i}{\partial x_i}$

Shear strains: $\varepsilon_{ij} = \frac{1}{2}(u_{i,j} + u_{j,i})$ ή $\gamma_{ij} = \frac{\partial u_i}{\partial x_j} + \frac{\partial u_j}{\partial x_i} = 2\varepsilon_{ij}$

Normal stresses: $\sigma_{ii} = \frac{F_i}{A_i}$, Where F_i is the force in the direction of the stress, and A_i is the area with a normal vector in the direction of the stress.

Shear Stresses: $\tau_{ij} = \frac{F_j}{A_i}$, Where τ_{ij} represents the shear stress, with the first index denoting the direction of the normal vector of the plane on which it acts, and the second index indicating the direction of the axis parallel to the stress. An important property of the strain tensor is that, for small displacements and deformations, it is symmetric:

$$\varepsilon_{ij} = \frac{1}{2}(u_{i,j} + u_{j,i}) = \varepsilon_{ji} \quad (\mathbf{4.17}).$$

To generate the equations for the deformable body, we apply the equations of dynamic equilibrium to the finite cube, which rotates about the x_3 axis and is depicted in Figure 4.6. In this figure, we can discern all the developing stresses in the finite cube. Additionally, because the gravitational force developed due to centrifugal force is an inertial force, we expect it to arise from the acceleration of the infinite cube and not as a form of applied force. For this reason, we do not see these forces in Figure 4.6.

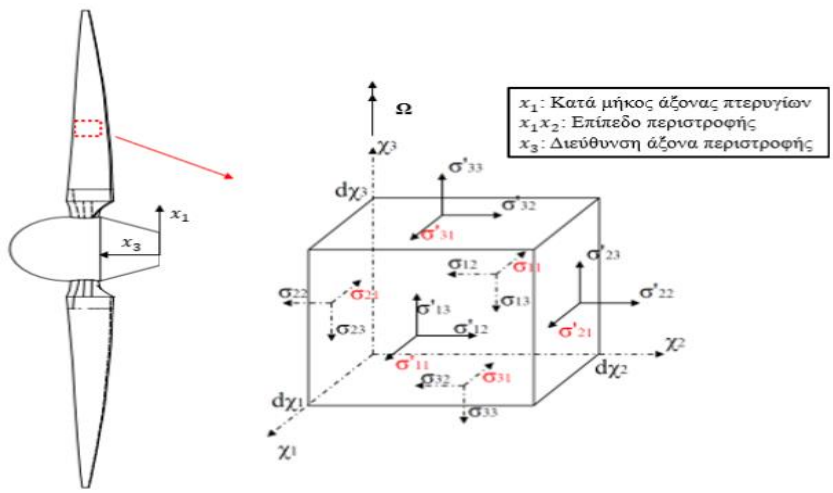

Figure 4. 6 Infinitesimal Cube and Applied Stresses

Before we proceed with the application of the motion equations for the three directions in the above figure, we need to define the acceleration of the cube. We symbolize the deformations in the directions x_1, x_2, x_3 as u_1, u_2, u_3, respectively. The acceleration of an arbitrary point of the structure for zero angular acceleration (Ω=constant), expressed with respect to the inertial system based on reference [1], is calculated from the equation:

$$\underline{\alpha} = \underline{\alpha}_t + \underline{a}_c$$

Where $\underline{\alpha}_t$ the translational component of the acceleration with respect to the rotating system, denoted as a_r, and a_c represents the centripetal acceleration. Because the structure is rotating only and not translating, the translational component only includes the terms of displacements due to deformation in their respective directions. In contrast, for centripetal acceleration, we take into account both the displacements and the distance of the point from the axis of rotation.

So, we have:

$$\underline{\alpha}_t = \left(\ddot{u}_1 \underline{e}_{x_1} + \ddot{u}_2 \underline{e}_{x_2} + \ddot{u}_3 \underline{e}_{x_3}\right)$$

$$\underline{a}_c = -\underline{\omega} \times \left(\underline{\omega} \times \underline{r}\right)$$

The negative sign in the acceleration a_c is due to the direction in which the centrifugal force acts. If we formulated the equations based on centripetal acceleration instead of centrifugal acceleration, this sign would indeed be positive. With $\underline{r} = (x_1 + u_1)\underline{e}_{x_1} + (x_2 + u_2)\underline{e}_{x_2} + (x_3 + u_3)\underline{e}_{x_3}$ and $\omega = \Omega\ \underline{e}_z$ we calculate:

$$\alpha_c = -\left(\Omega \underline{e}_{x_3}\right) \times \left(\left(\Omega \underline{e}_{x_3}\right) \times \left((x_1 + u_1)\underline{e}_{x_1} + (x_2 + u_2)\underline{e}_{x_2} + (x_3 + u_3)\underline{e}_{x_3}\right)\right) \Rightarrow$$

$$\Longrightarrow \alpha_c = -\left(\Omega \underline{e}_{x_3}\right) \times \left(\Omega(x_1 + u_1)\underline{e}_{x_2} - \Omega(x_2 + u_2)\underline{e}_{x_1}\right) \Rightarrow$$

$$\Longrightarrow \alpha_c = \Omega^2 \left((x_1 + u_1)\underline{e}_{x_1} + (x_2 + u_2)\underline{e}_{x_2}\right)$$

So, the total acceleration for the infinitesimal volume can be expressed in the form:

$$\underline{a} = \left(\ddot{u}_1 + \Omega^2(x_1 + u_1)\right)\underline{e}_x + \left(\ddot{u}_2 + \Omega^2(x_2 + u_2)\right)\underline{e}_y + (\ddot{u}_3)\underline{e}_z$$

Finally, the components of acceleration in the three directions are obtained as follows:

$$a_{x_1} = \ddot{u}_1 + \Omega^2(x_1 + u_1)$$

$$a_{x_2} = \ddot{u}_2 + \Omega^2(x_2 + u_2)$$

$$a_{x_3} = \ddot{u}_3$$

We apply the equations of motion with respect to the x_1 axis:

$$\Sigma F_1 = m a_{x_1} \Rightarrow$$

$$\Rightarrow (\sigma'_{11} - \sigma_{11})dx_2dx_3 + (\sigma'_{21} - \sigma_{21})dx_1dx_3 + (\sigma'_{31} - \sigma_{31})dx_1dx_2 + (f_1)dx_1dx_2dx_3 = \rho \underbrace{dV}_{dx_1dx_2dx_3} \left(\ddot{u}_1 + \Omega^2(x_1 + u_1)\right) \quad (\mathbf{4.18})$$

Όμως : $\sigma'_{11} = \sigma_{11}(x + dx_1) \xrightarrow{Taylor} \sigma_{11} + \frac{\partial \sigma_{11}}{\partial x_1}dx_1 + \underbrace{\frac{1}{2}\frac{\partial^2 \sigma_{11}}{\partial x_1^2}dx_1^2}_{O.A.T} + \cdots \Rightarrow (\sigma'_{11} - \sigma_{11}) = \frac{\partial \sigma_{11}}{\partial x_1}dx_1$

So, equation (4.18) becomes:

$$\frac{\partial \sigma_{11}}{\partial x_1} + \frac{\partial \sigma_{12}}{\partial x_2} + \frac{\partial \sigma_{13}}{\partial x_3} + f_1 = \rho \ddot{u}_1 + \rho\, \Omega^2(x_1 + u_1) \Longrightarrow$$

$$\Longrightarrow \frac{\partial \sigma_{11}}{\partial x_1} + \frac{\partial \sigma_{12}}{\partial x_2} + \frac{\partial \sigma_{13}}{\partial x_3} + f_1 - \rho\, \Omega^2 u_1 = \rho \ddot{u}_1 + \rho\, \Omega^2 x_1 \quad (\mathbf{4.19}\boldsymbol{a})$$

Where the term f_1 includes external forces acting in the x_1 direction and gravitational forces. Using the same procedure, we obtain equations in the other directions.

$$\frac{\partial \sigma_{21}}{\partial x_1} + \frac{\partial \sigma_{22}}{\partial x_2} + \frac{\partial \sigma_{23}}{\partial x_3} + f_2 - \rho \Omega^2 u_2 = \rho \ddot{u}_2 + \rho\, \Omega^2 x_2 \quad (\mathbf{4.19}\boldsymbol{\beta})$$

$$\frac{\partial \sigma_{31}}{\partial x_1} + \frac{\partial \sigma_{32}}{\partial x_2} + \frac{\partial \sigma_{33}}{\partial x_3} + f_3 = \rho \ddot{u}_3 \quad (\mathbf{4.19}\boldsymbol{\gamma})$$

Applying the equilibrium equations of moments about the center of gravity of the cube $(I_G \approx 0)$, we obtain the relationship $\sigma_{ij} = \sigma_{ji}$ $(\mathbf{4.20})$, which shows the symmetry of the stress tensor.

From Hooke's law, we derive the relationship between the strains and stresses as:

$$\sigma_{ij} = C_{ijkl}\varepsilon_{kl}$$

Where the matrix C is a fourth-order tensor composed of 81 constants. Application of stress and strain symmetry, and because our material is isotropic, the number of independent constants reduces to 2. These constants are the Poisson's ratio ν and the modulus of elasticity E. Isotropic materials have the same mechanical properties in all directions at each point. Each of their planes is a plane of symmetry, and each of their axes is an axis of symmetry.

In summary, we write the system of equations that describes the variables for a rotating deformable body:

$$\begin{cases} \frac{\partial \sigma_{11}}{\partial x_1} + \frac{\partial \sigma_{12}}{\partial x_2} + \frac{\partial \sigma_{13}}{\partial x_3} + f_1 - \rho\, \Omega^2 u_1 = \rho \ddot{u}_1 + \rho\, \Omega^2 x_1 \\ \frac{\partial \sigma_{21}}{\partial x_1} + \frac{\partial \sigma_{22}}{\partial x_2} + \frac{\partial \sigma_{23}}{\partial x_3} + f_2 - \rho \Omega^2 u_2 = \rho \ddot{u}_2 + \rho\, \Omega^2 x_2 \\ \frac{\partial \sigma_{31}}{\partial x_1} + \frac{\partial \sigma_{32}}{\partial x_2} + \frac{\partial \sigma_{33}}{\partial x_3} + f_3 = \rho \ddot{u}_3 \\ \sigma_{ij} = \sigma_{ji} \\ \varepsilon_{ij} = \frac{1}{2}\left(u_{i,j} + u_{j,i}\right) = \varepsilon_{ji} \\ \sigma_{ij} = C_{ijkl}\varepsilon_{kl} \end{cases} \qquad (\boldsymbol{II})$$

4.4.2 Propeller's Equations

Defining the matrix of differential operators L and changing the symbols for the axes $from\ (x_1, x_2, x_3)$ to (x, y, z) respectively, we have:

$$L = \begin{bmatrix} \frac{\partial}{\partial x} & 0 & 0 \\ 0 & \frac{\partial}{\partial y} & 0 \\ 0 & 0 & \frac{\partial}{\partial z} \\ \frac{\partial}{\partial y} & \frac{\partial}{\partial x} & 0 \\ 0 & \frac{\partial}{\partial z} & \frac{\partial}{\partial y} \\ \frac{\partial}{\partial z} & 0 & \frac{\partial}{\partial x} \end{bmatrix}, \underline{u} = \begin{bmatrix} u_x \\ u_y \\ u_z \end{bmatrix}, \underline{\varepsilon} = \begin{bmatrix} \varepsilon_x \\ \varepsilon_y \\ \varepsilon_z \\ 2\varepsilon_{xy} \\ 2\varepsilon_{yz} \\ 2\varepsilon_{xz} \end{bmatrix}, \underline{\sigma} = \begin{bmatrix} \sigma_{xx} \\ \sigma_{yy} \\ \sigma_{zz} \\ \sigma_{xy} \\ \sigma_{yz} \\ \sigma_{xz} \end{bmatrix}, \underline{f_{c_{in}}} = -\rho\, \Omega^2 \begin{bmatrix} u_x \\ u_y \\ 0 \end{bmatrix}, \underline{f_{c_{ex}}} = \rho\, \Omega^2 \begin{bmatrix} \mathrm{x} \\ y \\ 0 \end{bmatrix}$$

The system (II) can be written in the bulk form:

$$\begin{cases} L^T \underline{\sigma} + \underline{f} + \underline{f_{c_{in}}} = \rho \underline{\ddot{u}_i} + \underline{f_{c_{ex}}} & (\mathbf{4.21}) \\ \underline{\varepsilon} = L\underline{u} & (\mathbf{4.22}) \\ \underline{\sigma} = C\underline{\varepsilon} & (\mathbf{4.23}) \end{cases} \qquad (\boldsymbol{III})$$

The first equation of the system (II) expresses the motion equations of the finite element and is accompanied by a set of boundary and initial conditions, in their general form:

$$\begin{cases} \underline{u}\big|_{\Gamma_u} = \underline{\hat{u}} \\ \underline{\sigma}\big|_{\Gamma_\sigma} \underline{\hat{n}} = \underline{\hat{t}} \end{cases} \quad (\mathbf{4.24})$$

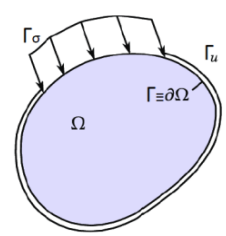

And

$$\begin{cases} \underline{u}(\underline{r}, 0) = \underline{u}_0(\underline{r}) \\ \underline{u}(\underline{r}, 0) = \underline{v}_0(\underline{r}) \end{cases} \quad (\mathbf{4.25})$$

where Γ_u and Γ_σ represent the partitions of the external surface into regions with known displacements and known external loads.

The system (III) constitutes a system of partial differential equations, both in space and time, that describe all the variables for our body. Equation (4.21) represents the motion equations of the system.

Finite Element Analysis Method

The logic behind the finite element method begins with the geometric discretization of our body into elements of predetermined geometry. It involves expressing the displacements within each element ($\underline{u}(\underline{r},t)$), based on the nodal values of these variables, where $\underline{r} = (x, y, z)$. Each node of the mesh (in 3D problems) has 6 degrees of freedom, of which 3 are rotational and 3 are translational.

The correlation between the nodal values and the distributions of the internal variables within the elements is achieved using predefined functions known as shape functions, denoted as $N_i(\underline{r})$. The equation for computing the displacements is as follows:

$$\underline{u}(\underline{r},t) \approx \sum_{i=1}^{n} N_i(\underline{r})\underline{u}_i(t) = N(\underline{r})\underline{\hat{u}}(t) \quad (\mathbf{4.26})$$

where $\underline{\hat{u}}(t)$ represents the nodal values of displacements. The values for the displacements $\underline{u}(\underline{r},t)$, which we calculate, must satisfy the equations of the system (III). A fundamental question that arises is what kind of elements we will discretize and what are the expressions for the shape functions $N_i(\underline{r})$.

For three-dimensional geometries, we can use various types of elements (tetrahedra, hexahedra, etc.). Each element has specific advantages and disadvantages compared to others. The elements we use will be presented in the discretization section. Additionally, the shape functions depend on the number of nodes and the type of problem (2D, 3D). For example, for a tetrahedron, we can have nodes only at the corner points or even at their midpoints. Increasing the number of nodes increases the complexity but also the accuracy of the solution (provided that the N functions are correctly formulated).

Galerkin

Since equation (4.26) is an approximate equation for calculating displacements, replacing it in the general equation of the continuous medium (4.16) results in an error in the form of:

$$L\underline{u}(\underline{r},t) + m(\underline{r})\underline{\ddot{u}}(\underline{r},t) - f(\underline{r},t) = \varepsilon(\underline{r},t)$$

A requirement for the Galekin's method is that the error $\varepsilon(\underline{r},t)$ satisfies the condition :

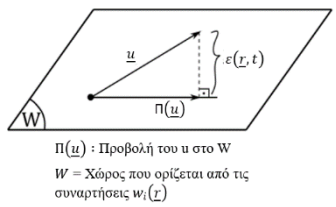

Figure 4. 7 Geometric interpretation of Galerkin

$$\int_S \varepsilon(\underline{r},t)\, w_i(\underline{r}) dS = 0$$

In the above integral, the functions multiplied by the error are denoted as "w" and are called weighting functions. Subsequently, when these functions are considered to be the shape functions of the finite elements, they are denoted as "N." The integral above implies that the error must be orthogonal to all the functions $w_i(\underline{r})$. The assumption of orthogonal error to the shape functions is made because if we consider a horizontal plane and a point outside this plane, as shown in Figure 4.7, then the shortest possible distance from this point to the plane defined by the vectors $w_i(\underline{r})$ is the perpendicular distance. The shape functions must be acceptable, which means they must satisfy all the geometric boundary conditions of the system.

Before we proceed with the application of the Galerkin method, based on the theorem of divergence, we have the following:

$$\int_\Omega \underline{u}\, \nabla \underline{v} d\Omega = \int_\Omega \underline{u}\, \underline{v}\, \underline{\hat{n}} d\Gamma - \int_\Omega \nabla \underline{u}\, \underline{v} d\Omega \quad (\mathbf{4.27})$$

Where Ω the integration volume, $\Gamma = \Gamma_u \cup \Gamma_\sigma = \partial\Omega$ is the borders for Ω and $\underline{\hat{n}}$ the vertical unit vector for the border with outward direction.

Now, multiplying the equation of motion (4.21) by the weighting function and integrating over the entire volume of the body gives us:

$$\underbrace{\int_\Omega \underline{w}^T \left(-L^T \underline{\sigma} - \underline{f} - \underline{f}_{c_{in}} + \rho \underline{\ddot{u}}_i + \underline{f}_{c_{ex}}\right) d\Omega}_{weighted\ residual} = 0$$

$$\Rightarrow \int_\Omega \underline{w}^T \left(\rho \underline{\ddot{u}}_i\right) d\Omega - \int_\Omega \underline{w}^T \left(L^T \underline{\sigma}\right) d\Omega - \int_\Omega \underline{w}^T \left(\underline{f}\right) d\Omega - \int_\Omega \underline{w}^T \left(\underline{f}_{c_{in}}\right) d\Omega + \int_\Omega \underline{w}^T \left(\underline{f}_{c_{ex}}\right) d\Omega = 0 \overset{(4.27)}{\Longrightarrow}$$

$$\Rightarrow \int_\Omega \underline{w}^T \left(\rho \underline{\ddot{u}}_i\right) d\Omega + \int_\Omega \left(L\underline{w}\right)^T \underline{\sigma}\, d\Omega - \int_\Gamma \underline{w}^T \underline{\sigma}\, \underline{\hat{n}} d\Gamma - \int_\Omega \underline{w}^T \underline{f}\, d\Omega - \int_\Omega \underline{w}^T \underline{f}_{c_{in}}\, d\Omega + \int_\Omega \underline{w}^T \left(\underline{f}_{c_{ex}}\right) d\Omega = 0 \overset{(4.23)}{\Longrightarrow}$$

$$\Rightarrow \int_\Omega \underline{w}^T \left(\rho \underline{\ddot{u}}_i\right) d\Omega + \int_\Omega \left(L\underline{w}\right)^T C\underline{\varepsilon}\, d\Omega - \int_{\Gamma_\sigma} \underline{w}^T \underline{\sigma}\, \underline{\hat{n}} d\Gamma - \int_\Omega \underline{w}^T \underline{f}\, d\Omega + \rho\, \Omega^2 \int_\Omega \underline{w}^T N \underline{\hat{u}}\, d\Omega + \int_\Omega \underline{w}^T \left(\underline{f}_{c_{ex}}\right) d\Omega = 0 \overset{(4.22),(4.26)}{\Longrightarrow}$$

$$\Rightarrow \int_\Omega \underline{w}^T \left(\rho N \underline{\ddot{\hat{u}}}\right) d\Omega + \int_\Omega \left(L\underline{w}\right)^T CLN \underline{\hat{u}}\, d\Omega - \int_{\Gamma_\sigma} \underline{w}^T \underline{\sigma}\, \underline{\hat{n}} d\Gamma - \int_\Omega \underline{w}^T \underline{f}\, d\Omega + \rho\, \Omega^2 \int_\Omega \underline{w}^T N \underline{\hat{u}}\, d\Omega + \int_\Omega \underline{w}^T \left(\underline{f}_{c_{ex}}\right) d\Omega = 0 \overset{\underline{w} \equiv \underline{N}}{\Longrightarrow}$$

In this step, we use the shape functions of the finite elements as weighting functions. This results in the final mass and stiffness matrices being symmetric. If we were to use a different methodology, such as displacement-based finite elements, the shape functions would be different, and the matrices may not be symmetric:

$$\Rightarrow \int_{\Omega} N^T \rho N \ddot{\underline{\hat{u}}}\, d\Omega + \int_{\Omega} (L\underline{N})^T CLN\underline{\hat{u}}\, d\Omega + \rho\, \Omega^2 \int_{\Omega} \underline{w}^T N \underline{\hat{u}}\, d\Omega = \int_{\Gamma_\sigma} \underline{N}^T \underline{\sigma}\, \underline{\hat{n}} d\Gamma + \int_{\Omega} \underline{N}^T \underline{f}\, d\Omega + \int_{\Omega} \underline{N}^T \left(\underline{f_{c_{ex}}}\right) d\Omega \overset{B=LN}{\Longrightarrow}$$

$$\Rightarrow \ddot{\underline{\hat{u}}} \underbrace{\int_{\Omega} N^T \rho N\, d\Omega}_{M} + \underline{\hat{u}} \left[\underbrace{\int_{\Omega} B^T CB\, d\Omega}_{K_{NR}} + \Omega^2 \rho \underbrace{\int_{\Omega} \underline{w}^T N''\, d\Omega}_{K_C} \right] = \underbrace{\int_{\Gamma_\sigma} \underline{N}^T \underline{\sigma}\, \underline{\hat{n}} d\Gamma + \int_{\Omega} \underline{N}^T \underline{f}\, d\Omega}_{F} + \underbrace{\int_{\Omega} \underline{N}^T \left(\underline{f_{c_{ex}}}\right) d\Omega}_{F_c}$$

$$\Rightarrow M\ddot{\underline{\hat{u}}} + (K_{NR} + \Omega^2 K_c)\underline{\hat{u}} = F + F_c \quad (\mathbf{4.27})$$

The system of equations (4.27) represents the equations of motion of the structure and constitutes a system of second-order ordinary differential equations. The vector $\underline{\hat{u}}$ consists of all the degrees of freedom of all the nodes discretizing the structure. In this system of equations, we need to include the non-steady aerodynamic loads acting on the propeller from the airflow. Therefore, we add the term $F_A(t)$, which is updated for each time step. Additionally, we symbolize the vector of degrees of freedom as $\underline{q}$, which is a more common notation and refers to the generalized coordinates of the deformable structure. Thus, the system (4.27) takes its final form.

$$M\ddot{\underline{q}}(t) + (K_{NR} + \Omega^2 K_c)\underline{q}(t) = F + F_c + F_A(t) \quad (\mathbf{4.28})$$

where K_{NR} is the stiffness introduced by the characteristics of the system, and K_c is the stiffness introduced by the centrifugal force.

Together with boundary and initial conditions, this system can be solved either analytically or numerically. From the solution of this system, we calculate the displacements at the nodes, and then, using equations (4.22) and (4.23), we calculate the rotations and stresses in the structure. For the analytical solution of the system, after numerically calculating the integrals in the matrices of equation (4.28), we can apply the method of mode superposition, based on which the response is calculated from the equation:

$$\underline{q} = \sum_{n=1}^{k} \underline{\varphi_n} \tau_n(t)$$

Where $\tau_n(t)$ are the principal coordinates and $\underline{\varphi_n}$ are the orthonormal mode shapes of the system.

The problem with the method of mode superposition is the very large number of degrees of freedom for the system (6 times the number of nodes), which makes the solution particularly time-consuming. This problem can be solved by applying methods to reduce the degrees of freedom, such as the one presented below.

We consider periodic excitation for the system in the form $\underline{F}(t) = \hat{A}\cos(\Omega t)$. Due to the periodic excitation, we assume that our solution for the principal coordinates $\underline{\tau}(t)$ will also be periodic in the form

$$\tau_n(t) = \frac{\Phi^T \hat{A}}{\omega_n^2 - \Omega^2} \cos(\Omega t) \quad (\mathbf{4.29}), \qquad \textit{Where } \Phi \textit{ is the eigenvector matrix}$$

The last equation shows us that the modes with the most influence on our solution are those with natural frequencies (ω_n) close to the excitation frequency Ω. Because the excitation frequency is generally low, we can retain only the first l terms of equation (4.29), with l much smaller than the total number of degrees of freedom k.

We briefly mention another, more accurate method for reducing degrees of freedom, the Craig-Bampton method, in which the high-frequency modes, instead of being completely neglected, are replaced by unit displacement vectors. In other words, for the static response of the structure, this results from imposing unit displacement on each degree of freedom at the boundaries. Here, the term "boundary degrees of freedom" refers to those that connect this component with neighboring or directly loaded components.

For our problem, we apply the modal analysis method to calculate the natural frequencies and modes at different operating speeds of the propeller. To calculate natural frequencies and modes, we solve the eigenproblem of equation (4.28). After removing the excitation from the system of equations, we solve the system.

$$(K - \omega_n^2 M)\underline{\varphi_n} = \underline{0} \quad , \quad \mu\varepsilon\, K = (K_{NR} + \Omega^2 K_c)$$

Where the eigenvalues ω_n are calculated by solving the equation$|K - \omega_n^2 M| = 0$ and in the next step, after we calculate the eigenvalues, we calculate the eigenmodes $\underline{\varphi_n}$.

The computation of the system's response is carried out using the numerical methods that will be presented in section 4.5.

4.4.3 Fluid Equations

The equations we solve for calculating the aerodynamic field are the same as the fluid mechanics analysis we performed in the previous chapter. As a reminder, we rewrite these equations. We solve the URANS (Unsteady Reynolds-Averaged Navier-Stokes) equations:

$$\begin{cases} \dfrac{\partial \overline{\rho}}{\partial t} + \dfrac{\partial}{\partial x_i}(\overline{\rho}\, u_i) = 0 \\ \dfrac{\partial(\overline{\rho}\, u_i)}{\partial t} + \dfrac{\partial}{\partial x_i}\left(\overline{\rho}\, u_i u_j\right) = -\dfrac{\partial \overline{p}}{\partial x_i} + \dfrac{\partial}{\partial x_i}\left(\mu\left(\dfrac{\partial u_i}{\partial x_j} + \dfrac{\partial u_j}{\partial x_i} - \dfrac{2}{3}\delta_{ij}\dfrac{\partial u_i}{\partial x_i}\right)\right) + \dfrac{\partial}{\partial x_j}\left(-\rho\overline{u_i' u_j'}\right) + F_i \end{cases} \quad (\boldsymbol{I})$$

Using the turbulence model SST k-ω 2 equations:

$$\frac{\partial}{\partial t}(\rho k) + \frac{\partial}{\partial x_i}(\rho k u_i) = \frac{\partial}{\partial x_j}\left(\Gamma_\kappa \frac{\partial k}{\partial x_j}\right) + G_k - \Upsilon_k + S_k$$

$$\frac{\partial}{\partial t}(\rho \omega) + \frac{\partial}{\partial x_i}(\rho \omega u_i) = \frac{\partial}{\partial x_j}\left(\Gamma_\omega \frac{\partial \omega}{\partial x_j}\right) + G_\omega - \Upsilon_\omega - D_\omega + S_k$$

For solving this system, we use the finite volume method, implementing the "Sliding Mesh" algorithm, and employing relaxation methods, as was done in the third chapter.

<u>Dynamic Computational Grid</u>

The difference compared to a simple CFD problem lies in the fact that our grid, located on the propeller, deforms with time. Therefore, we need to apply a process to correctly move the grid nodes to their new positions for each time step. This is achieved using the "Spring-based Smoothing" method.

According to this method, we consider that all edges between neighboring nodes represent springs. Based on Hooke's law, for any deformation of the grid and thus movement of its nodes, the resultant force applied to each node by all the springs connected to it arises from the equation:

$$F_i = \sum_{j}^{n_i} k_{ij}\left(\Delta x_j - \Delta x_i\right)$$

Where Δ_{x_i} and Δ_{x_j} are the displacements of nodes i and j, respectively, n_i is the number of neighboring nodes connected to node i, and k_ij is the spring constant of the spring, which can be expressed as $k_{ij} = \frac{k_{fac}}{\sqrt{|x_i - x_j|}}$, with k_{fac} being a constant to define the spring constant. For our problem, $k_{fac} = 1$. is chosen.

Since the system is in equilibrium, all the forces acting on node i must sum to zero. This can be calculated using an iterative scheme based on the equation:

$$\Delta x_i^{m+1} = \frac{\sum_j^{n_i} k_{ij} \Delta x_j^m}{\sum_j^{n_i} k_{ij}} \text{ , where m is the iteration number.}$$

Once the last equation converges, based on the error we define, the position of the node in the next time step (n+1) is determined by the equation:

$$x_i^{n+1} = x_i^n + \Delta x_i^{final}$$

4.5 Numerical Methods and Co – Simulation

<u>Numerical Integration Gauss – Legendre</u>

As we have seen, the matrices in equation (4.28) contain spatial integrals. Depending on the shape of the elements used for the geometric discretization of our structure, these integrals can differ, and in some cases, their computation can be particularly challenging. Moreover, due to the large dimensions of these matrices, analytical computation would require prohibitive amounts of time. For these reasons, these integrals are solved using the Gauss-Legendre numerical integration method.

This method is an approximation technique where we essentially approximate the integral with a weighted sum in the form:

$$\int_{-1}^{1} f(\xi) d\xi \approx \sum_{k=1}^{n} w_k f(\xi_k)$$

In this context, where n is the number of Gauss points used to approximate the integral, w_k represents the weighting coefficients. This method provides good accuracy for polynomials up to degree (2n-1). The evaluation points ξ_k, where the functions are computed, are equidistant. Therefore, depending on the number of points n chosen (for the desired accuracy), the values of the weighting coefficients and evaluation points for computing f can be found from tables like the one presented in Figure 4.8a. For the three-dimensional case, the integrals take the form:

$$\int_{-1}^{1}\int_{-1}^{1}\int_{-1}^{1} f(\xi,\eta,\mu)d\xi d\eta d\mu = \sum_{i=1}^{N}\sum_{j=1}^{N}\sum_{k=1}^{N} f(\xi_i,\eta_j,\mu_k)w_i w_j w_k$$

With the points distributed spatially in the manner shown in Figure 4.8b.

n	ξ_i	w_i
1	0	2
2	$\pm 1/\sqrt{3}$	1
3	0	$\frac{8}{9}$
	$\pm\sqrt{3}/\sqrt{5}$	$\frac{5}{9}$
4	$\pm\frac{1}{35}\sqrt{525-70\sqrt{30}}$	$\frac{1}{36}\left(18+\sqrt{30}\right)$
	$\pm\frac{1}{35}\sqrt{525+70\sqrt{30}}$	$\frac{1}{36}\left(18-\sqrt{30}\right)$
5	0	$\frac{128}{225}$
	$\pm\frac{1}{21}\sqrt{245-14\sqrt{70}}$	$\frac{1}{900}\left(322+13\sqrt{70}\right)$
	$\pm\frac{1}{21}\sqrt{245+14\sqrt{70}}$	$\frac{1}{900}\left(322-13\sqrt{70}\right)$

(α)

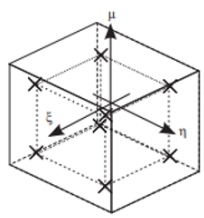

(β)

Figure 4. 5 Gauss values (α) and distribution (β) points

Newmark

Having described the method for calculating the integrals in the equation of motion, we can now compute the response of the displacements of the nodes in the structure. To achieve temporal discretization, the Newmark method is applied. The Newmark method is used for systems of differential equations and is based on the assumption that acceleration changes linearly with time. The equations for this method at the time step (m+1) are given, based on reference [3]:

$$\underline{\dot{x}}_{m+1} = \underline{\dot{x}}_m + h\left[(1-\beta)\underline{\ddot{x}}_m + \beta\underline{\ddot{x}}_{m+1}\right] \quad (\mathbf{4.30})$$

$$\underline{x}_{m+1} = \underline{x}_m + h\underline{\dot{x}}_m + h^2\left[\left(\frac{1}{2}-\alpha\right)\underline{\ddot{x}}_m + a\underline{\ddot{x}}_{m+1}\right] \quad (\mathbf{4.31})$$

The notation $\underline{x}_m$, refers to the values of the vector x at time step m, $\underline{x}_m = \underline{x}(t_m)$.). The coefficients α and β are chosen in such a way that the computational scheme is stable (usually around $\alpha = \frac{1}{5}, \beta = \frac{1}{2}$). We write the system (4.28) for the time step (m+1) and solve (4.31) for the second-time derivative.

$$\underline{\ddot{x}}_{m+1} = \frac{1}{ah^2}\left(\underline{x}_{m+1} - \underline{x}_m\right) - \frac{1}{ah}\underline{\dot{x}}_m + \left(1-\frac{1}{2a}\right)\underline{\ddot{x}}_m \quad (\mathbf{4.32})$$

Next, we first substitute equation (4.30) and then (4.32) into the system (4.28). Thus, we obtain a system of the form $\underline{x}_{m+1} = \underline{f}\left(\underline{x}_m, \underline{\dot{x}}_m, \underline{\ddot{x}}_m\right)$ $(\mathbf{4.33})$.

If this system does not contain nonlinear terms, it is solved directly by first calculating the acceleration $\underline{\ddot{x}}_0$, from the motion equation using the initial conditions. Then, by substituting the values $\left(\underline{x}_0, \underline{\dot{x}}_0, \underline{\ddot{x}}_0\right)$) into (4.33), $\underline{x}_1$is computed. We proceed by introducing this value into (4.30) and (4.32) to calculate $\left(\underline{\dot{x}}_1, \underline{\ddot{x}}_1\right)$, and we repeat this process until we calculate all values within the desired time interval.

In cases where there are nonlinear terms in the system (4.33), we apply an iterative procedure at each integration step. Specifically, equation (4.33) is solved using the Newton–Raphson method for each time step $\underline{x}_{m+1}$. The solution scheme takes the form:

$$\underline{x}_{m+1}^{k+1} = \underline{x}_{m+1}^{k} + \underline{\Delta x}_{m+1}^{k}$$

until convergence is achieved, with k denoting the index of the inner iterations at each time step. A more detailed description of the Newmark and Newton–Raphson methods is presented in reference [3].

Before we proceed with the discretization process of our structure, we present the principles of co-simulation and the algorithm that we will use to exchange information between the software components.

FSI and Co – Simulation

During co-simulation, the different subsystems (fluid and structure) that define our problem are modeled and simulated separately in a distributed manner. Thus, the modeling of each problem is done separately within the subsystems, without considering their coupling.

Based on this, we understand that solving Fluid-Structure Interaction (FSI) systems requires co-simulation between the structure and fluid subsystems. To couple the two subsystems, we use a loosely coupled approach. In this form, the subsystems depend on each other to the smallest possible extent. This co-simulation architecture protects the individual subsystems, reducing the risk of changes in one system affecting the other. Consequently, a loosely coupled system can be easily separated into its individual subsystems, from which it is composed.

Generally, there are two distinct forms of analysis that can be conducted for FSI systems:

- 1 - way FSI
- 2 - way FSI

For the "1-way FSI" simulation, aerodynamic loads are computed once (for one rotation of the propeller), and based on these loads, the structure deforms. Therefore, the simulation calculates deformations at each time step for the aerodynamic forces acting on the solid propeller. However, as we have analyzed up to this point, because aerodynamic forces deform the propeller, the deformation of the propeller affects the forces, and in turn, the forces modify the field of modes. Hence, we understand that at each time step, the displacements of the structural nodes should be transferred to the fluid grid and deform it accordingly to follow the deformation of the propeller.

The process described is carried out with the "2-way FSI" analysis and is considered a fully coupled simulation for aeroelastic systems.

The two subsystems, along with the coupling subsystem that applies the "Gauss–Seidel" algorithm, are connected in a structure called Master-Slave, where the structural solver (ANSYS Mechanical) and the fluid field solver (ANSYS FLUENT) act as Slave subsystems, while the coupling system serves as the Master. For communication between subsystems and data exchange between them, the "Gauss–Seidel" algorithm is employed, and it is executed by the coupling subsystem. The name of the algorithm is derived from its similarities to the numerical method of the same name. In Figure 4.9, two schematic representations of the coupling algorithm are depicted.

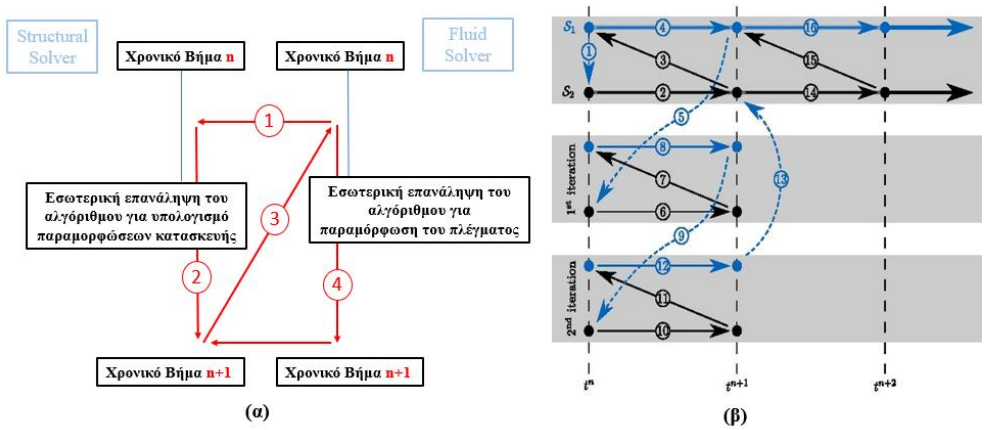

Figure 4.6 Schematic presentation for the algorithm Gauss-Seidel

From the above diagram, we can see that the algorithm begins by calculating the aerodynamic forces, which are then transferred to the structural part and deform the structure. When the solution for the structural deformation converges, the structural part advances to the (n+1)-th time step, while simultaneously, the deformations of the mesh are returned to the fluid solver to update the fluid grid. In the 4th step, as shown in Figure 4.9a, the "Spring-based Smoothing" method, as described previously, is applied. In Figure 4.9a, we see a cycle of communication between the subsystems, where in reality, the coupling subsystem, before proceeding to the next time step, applies a number of internal iterations (which are defined by us) to improve the coupling. The iterative process of the coupling is shown in Figure 4.9b, where you can see the 3 iterations of the coupling before advancing to the (n+1) time step. Finally, it's worth noting that both subsystems, the fluid and the structure, apply internal iterative loops for better accuracy in the solution.

For our co-simulation problem, we require the Master subsystem to perform at least 5 coupling iterations at each time step of the solution. Furthermore, for the fluid mechanics problem, we instruct the solver to apply 5 internal iterations.

4.6 Discretization

We use the mesh created in the third chapter for the structural domain without any modifications. For this reason, it will not be presented again.

We discretize our structure using linear tetrahedral elements. This means that each spatial element consists of 4 nodes (1 at each vertex). The shape functions used in such elements were discussed in the presentation of the Finite Element Method (FEM).

We choose higher density meshing for the propeller in the thin regions of the blade at the Leading Edge (LE) and Trailing Edge (TE), as these are the areas of interest due to significant deformations. The resulting mesh is depicted in Figure 4.10.

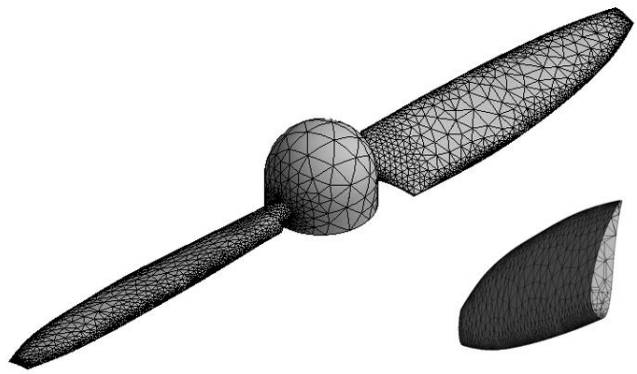

Figure 4. 7 Discretized propeller with linear tetrahedral elements

The tetrahedral elements were chosen for both the fluid and structural domains due to their ability to model complex geometries effectively.

In Table 4.1, the mesh dimensions and quality criteria are presented. In Figure 4.11, the quality regions are shown again for the criteria of orthogonality and aspect ratio. The mesh appears to be in good regions for these criteria, indicating that it can provide a good solution.

The mesh was created using ANSYS Mechanical software, and this software will also be used for the simulation. For simulating the structure, a rotational velocity is introduced along the y-axis of the propeller, matching the rotation speed of the mesh. Additionally, at the beginning of the simulation, we ensure that the positions of the propeller in both the fluid mesh and the structural software are identical (e.g., horizontally aligned). This is done to simulate the presence of a rigid hub connecting the propeller to the gearbox. Another reason for placing a fixed hub is to avoid the rotational motion of the propeller around an axis other than the y-axis, which could lead to gyroscopic phenomena and instability, as discussed in Section 4.2. The forces generated due to gyroscopic motion will be discussed further in the next chapter.

For more details on structural discretization, you can refer to reference [15].

Table 4. 1 Grid quality dimensions and values for the quality criterions

Nodes Number	$7.6\ 10^4$	Orthogonality	Min = 0.24
Elements Number	$4.6\ 10^4$	Aspect Ratio	Max = 6.4
		Skewness	Max = 0.75

Ορθογωνικότητα

Unacceptable	Bad	Acceptable	Good	Very good	Excellent
0-0.001	0.001-0.14	0.15-0.20	0.20-0.69	0.70-0.95	0.95-1.00

Λοξότητα

Excellent	Very good	Good	Acceptable	Bad	Unacceptable
0-0.25	0.25-0.50	0.50-0.80	0.80-0.94	0.95-0.97	0.98-1.00

Figure 4. 8 Quality criterions values

4.7 Results

In this section, the results are presented. Initially, the Campbell diagram for our propeller is created, and the natural (without rotation) modes of the structure are presented. Subsequently, the responses of the loads and deformations are shown, the Fourier transform is applied, and the pressure coefficient distributions at specific cross-sections are presented. Finally, the distribution of von Mises stresses for the aeroelastic problem is shown.

4.7.1 Modal Analysis and Campbell diagram

From the analysis of the natural modes of vibration, we can observe the eigenmodes and eigenfrequencies of the structure. Initially, we present these modes without applying any centrifugal force (without rotational speed). Increasing the propeller's rotational speed may lead to higher eigenfrequencies and larger mode shapes, but the characteristic nature of low-frequency modes remains the same.

The term "characteristic nature" refers to the nature of deformation (such as bending modes, twisting modes, etc.). Depending on the direction of bending, two terminologies are commonly used for interpreting the results in aviation propellers: "flapwise" bending (bending perpendicular to the plane of rotation) and "edgewise" bending (bending within the plane of rotation).

In Figure 4.12, we present the first four elastic eigenmodes and eigenfrequencies of our structure, scaled by a factor of 4. A color scale indicates the displacement magnitudes at corresponding positions. From this figure, it's evident that as the mode order increases, the complexity of the mode shape also increases. Additionally, it's worth noting that torsional modes or coupled modes (e.g., bending and torsion together) tend to occur at much higher eigenfrequencies.

These eigenmodes and eigenfrequencies provide valuable insights into how the structure vibrates naturally under various conditions, and they are essential for understanding its dynamic behavior and potential resonances. If you have specific questions or need further information about these modes and frequencies or their implications, please let me know.

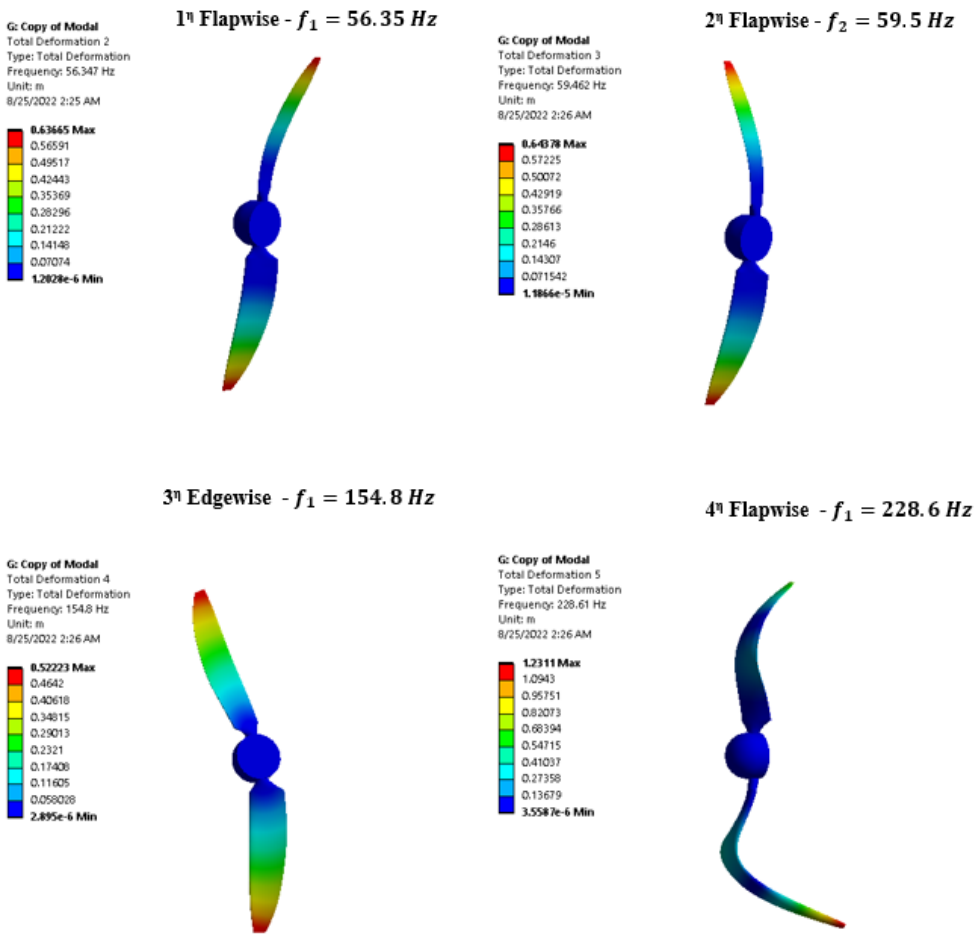

Figure 4. 9 Elastic eigenmodes and eigenfrequencies of the propeller and color-coded displacement visualization.

To generate the Campbell diagram for the propeller, we need to conduct a pre-stressed analysis. Through this analysis, we essentially introduce the influence of the loads resulting from rotation, which enhances the stability of the structure. This method, instead of calculating the terms arising from the distribution of the centrifugal force, introduces a stress field for the propeller for each different rotational speed. Thus, the eigenproblem solved at the end has the form:

$$(K + [S] - \omega_n^2 M)\underline{\varphi_n} = \underline{0}$$

Where [S] is the stress matrix. To perform this analysis in the Mechanical software, we calculate the stress field for each rotational speed and then conduct a modal analysis while maintaining our structure under these stresses. Figure 4.13 shows the Campbell diagram for the first 4 elastic modes and the first 4 harmonic components of the propeller's rotational speed. On the coordinate axis, the normalized frequency is plotted with respect to the frequency of the 1st mode for zero angular velocity. Additionally, the dashed lines in the diagram represent the speeds of the value sets for which we will solve the aeroelastic system.

We can observe that for speeds close to 2000 rpm, the 2P component of the load approaches resonance with the 1st mode. Consequently, we expect to see large response amplitudes for displacements in the y-direction, as the 1st mode bends in the flapwise direction. For modes 3 and

4, there is no risk of resonance within the range of values we simulate. The other modes exhibit significantly higher natural frequencies, placing them outside the Campbell diagram. It is evident that the eigenfrequencies of the structure vary significantly with rotational speed. In general, it is preferable to avoid operating at values close to the intersection of eigenmodes with harmonic loads. In our specific problem, however, we aim to highlight the effect of this phenomenon.

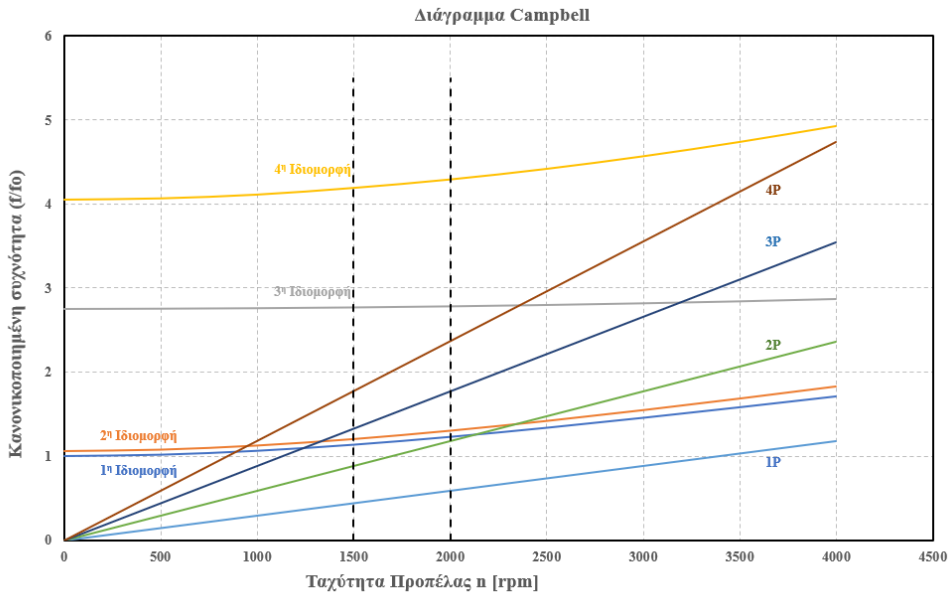

Figure 4. 10 Propeller's Campbell diagram

4.7.2 Load response and Fourier analysis

The simulation conditions remain the same as those for which we solved the fluid mechanics problem in Chapter 3 and are summarized in Table 4.2. Table 4.3 presents the physical properties of the air at sea level since we simulate the propeller's takeoff operation. To solve the aeroelastic problem, we begin with a solution that has fully converged our flow field. Specifically, we first solve the solid propeller model for steady-state conditions, and once steady state is achieved, we proceed to solve for the transient phenomenon until we reach a stable periodic solution. As we will see in the response plots later, for our problem, it took 8 rotations of the propeller until the aeroelastic problem reached a steady state.

The time step we use ensures that, for each set of values, the propeller rotates by 18 degrees in a single time step. This choice was made to obtain satisfactory results while keeping simulation time within acceptable limits. As for the fluid mechanics problem, the rotation axis of the propeller is the y-axis, the z-axis is in the direction of gravity's positive direction, and the x-axis is oriented to satisfy the right-hand rule. For the fluid mechanics problem, we introduce 5 inner iterations for solution convergence, and for the coupling sub-system, we also employ 5 iterations to improve the solution. For the propeller, a constant force is applied to the hub. This way, we simulate the connection between the propeller and the output shaft of the gearbox.Table 4. 2 Simulation conditions FSI

	Set 1	Set 2	Set 3	Set 4
Aircraft velocity	$V = 20\ \left[\frac{m}{s}\right]$	$V = 30\ \left[\frac{m}{s}\right]$	$V = 20\ \left[\frac{m}{s}\right]$	$V = 30\ \left[\frac{m}{s}\right]$
Propeller's rotational velocity	$n = 1500[rpm]$	$n = 1500[rpm]$	$n = 2000[rpm]$	$n = 2000[rpm]$
Propeller's pitch angle	$\beta = 10°$	$\beta = 10°$	$\beta = 10°$	$\beta = 10°$
Aircraft's AOA on take - off	$\alpha = 10°$	$\alpha = 10°$	$\alpha = 10°$	$\alpha = 10°$

Table 4. 3 Air properties above the sea level

Density	$\rho = 1.225\ \left[\frac{kg}{m^3}\right]$	Temperature	$T = 288.15\ [K]$
Dynamic viscosity	$\mu = 1.789\ 10^{-5}\ \left[\frac{kg}{ms}\right]$	Specific heat ratio	$k = 1.401$
Total Pressure	$P = 1.013\ 10^5\ [Pa]$	Sound velocity	$a = 304.3\ \left[\frac{m}{s}\right]$

In Figure 4.14, the responses of the blade deflection for the last 3 rotations of the propeller are presented to verify the convergence of our solution. It is interesting to observe that as the propeller's rotations increase (sets 3 and 4), and therefore, the loads increase, it becomes more challenging to achieve a steady-state solution, and the complexity of the diagrams also increases. Specifically, for the 3rd set of values, we can see that the behavior of the blade deflection response differs significantly compared to the other sets. This is primarily due to the large loads and their influence on the elastic characteristics of the structure.

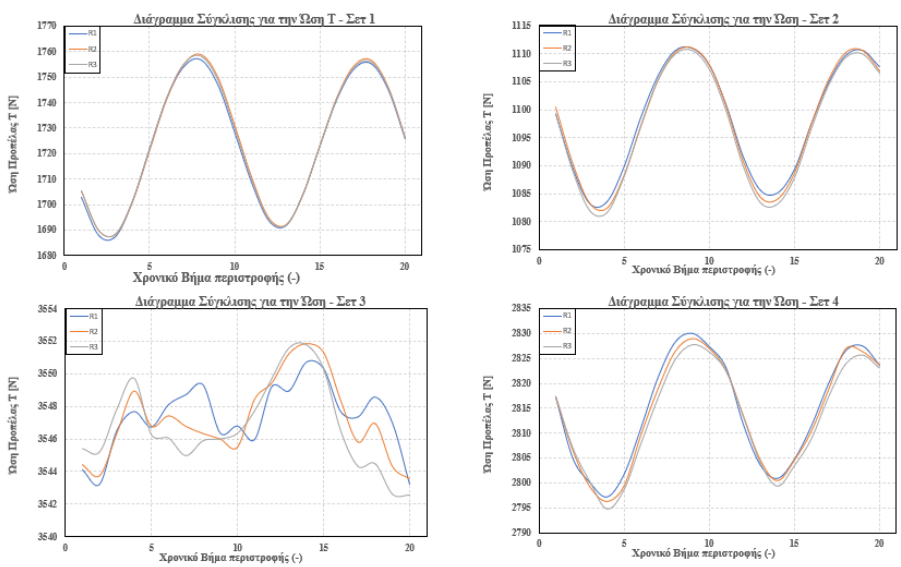

Figure 4. 11.Convergence plots for Thrust for the 4 operational conditions sets.

In Figures 15 and 16, the responses of the moments in the y-direction (rotational axis) and z-direction (plane of rotation) are presented. Just like with thrust, we observe that the complexity increases as the loads increase. The differentiation in the diagrams results from the deformation of the structure. The deformed structure changes the angles of attack seen by the individual airfoils of the blades, leading to significant variations in loads along the blades. The shapes of the load

responses can be better understood from the values in Table 4.4, which contains the results of the Fourier analysis for the last rotation of the propeller.

In this table, we can see that the 2P harmonic component remains dominant compared to the other dynamic loads. Specifically, for the moment in the z-direction, resulting from the change in the angle of attack in the horizontal position, we can observe that the amplitude of the 2P component is larger than the static component. The M_z load is responsible for bending out of the plane of rotation (flapwise), and especially for sets 3 and 4, we can see a significant increase in the amplitudes of the 2P component compared to the others for M_z. In general, we can say that for loads acting in directions defining the plane of rotation, emphasis should be placed on the harmonic components. Conversely, for loads along the rotational axis, static loads are of primary importance, as the amplitudes of the dynamic components are orders of magnitude smaller.

Table 4. 4 Fourier results for the loads T, M_y, M_z

Set	1o			2o			3o			4o		
Load	T	My	Mz	T	My	Mz	T	My	Mz	T	My	Mz
Harmonic Component												
0P	1720	379.12	41.9	1099	309	14	3546	704	16.7	2813	652	7.97
1P	2	0.11	2	1.2	0.93	0.75	1.99	0.21	5.3	2.59	0.28	1.3
2P	34	6	54.8	28	4.7	19.3	2.87	1.81	90	14.55	3	101
3P	0.1	0.007	0.21	0.06	0.0064	0.0057	0.247	0.0093	0.25	0.127	0.017	0.33

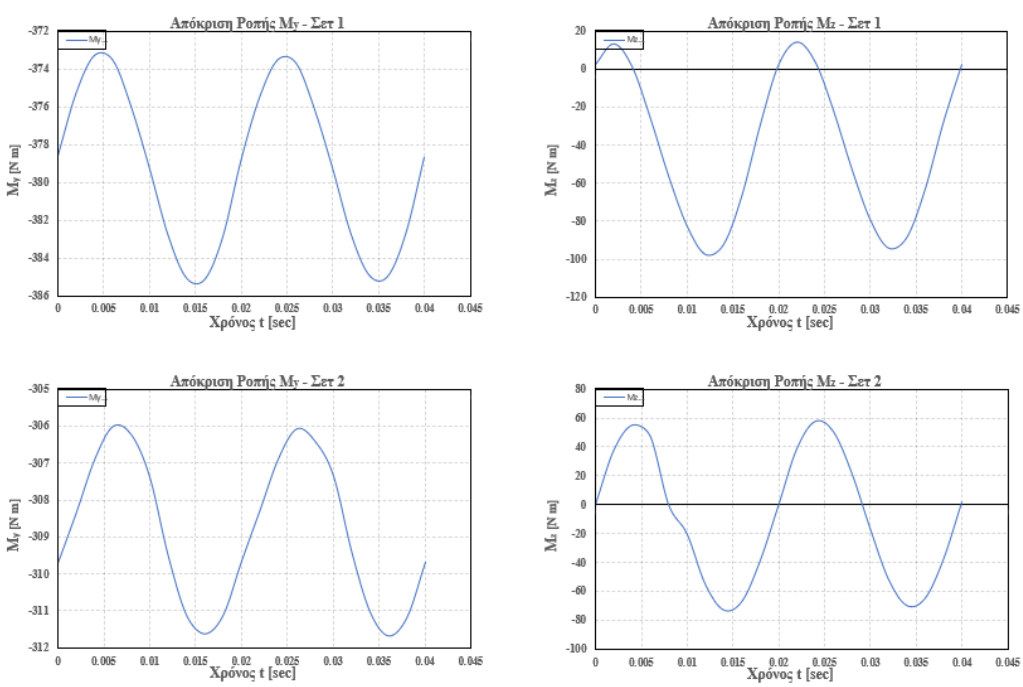

Figure 4. 12 Moment responses on the axis y, z for the sets 1,2.

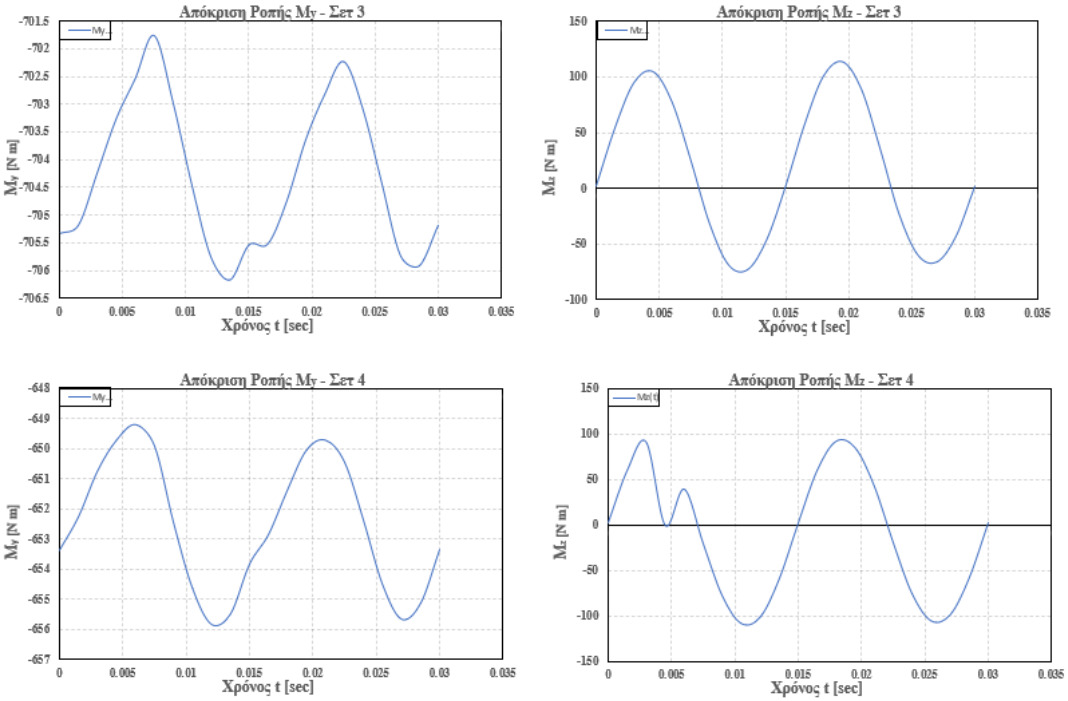

Σχήμα 4. 13 Moment responses on the axis y, z for the sets 3,4

4.7.3 Structural Response

The variables of the responses, displacements, and stresses are measured with respect to the rotating coordinate system f(x', y', z'), which is attached to the propeller and rotates with it. Under this convention, we have the rotational axis y', along which the material z' is distributed, and the x' axis perpendicular to the other two.

According to the Campbell diagram we presented in Figure 4.13, for rotational speeds of 2000 [rpm], the 2P components of the loads are near the resonance region with the 1st mode (flapwise) of the structure. Therefore, in the response diagrams of displacements and stresses, we expect to see large vibration ranges for sets 3 and 4 (2000 [rpm]) in the y-direction (flapwise). Initially, in Figure 4.17, we present the response of the maximum displacement for the three directions for the 4th set of values. Since we are discussing the maximum displacement, it obviously refers to a node located at the tip of the blade. From this diagram, we can grasp the orders of magnitude of the displacements and make comparisons among them. For example, we can see that the displacement in the y-direction is an order of magnitude larger than that in the x-direction, while, in turn, the displacement in the x-direction is an order of magnitude larger than that in the z-direction (axis of material distribution).

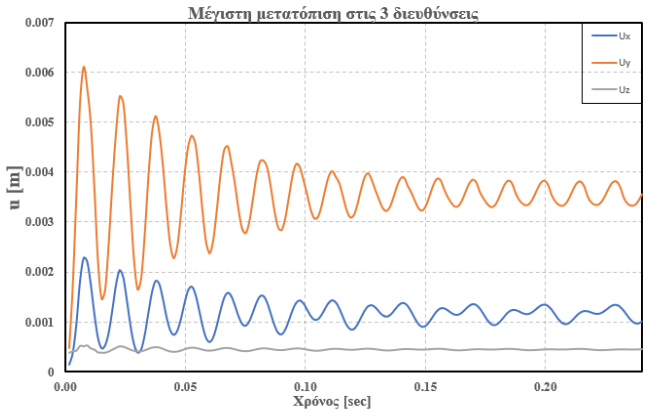

Figure 4. 14 Displacement response for the 3 directions.

Since the largest loads and, therefore, the greatest deformations occur at the leading edge of the blades, in Figure 4.18, we present the response of displacements in the x and y directions for the 4 sets of values at a point on the leading edge at a position r=0.75 R from the propeller hub. We observe that, in addition to the increase in vibration range for increasing loads, the shape of the response diagrams at this specific location exhibits complex periodic fluctuations compared to Figure 4.17, where we had uniform periodic responses.

The large-range vibrations with high frequencies observed at the beginning of the diagrams are due to the application of aerodynamic loads and the centrifugal force on the structure. Over time, we quickly converge to a periodic response with small vibration ranges. Additionally, we see that for sets of values with the same rotational speed in the steady state, the vibration ranges are very close to each other. This indicates that the free-flow velocity (aircraft speed) doesn't significantly influence the aeroelastic response over time. Furthermore, when comparing the two different directions (x and y), the behavior is the same, with the difference that in the x-direction (edgewise), the vibration ranges are approximately an order of magnitude smaller. It's important to note that in all the diagrams, for steady-state conditions, the frequency of displacement oscillations is the same as the propeller's rotational frequency.

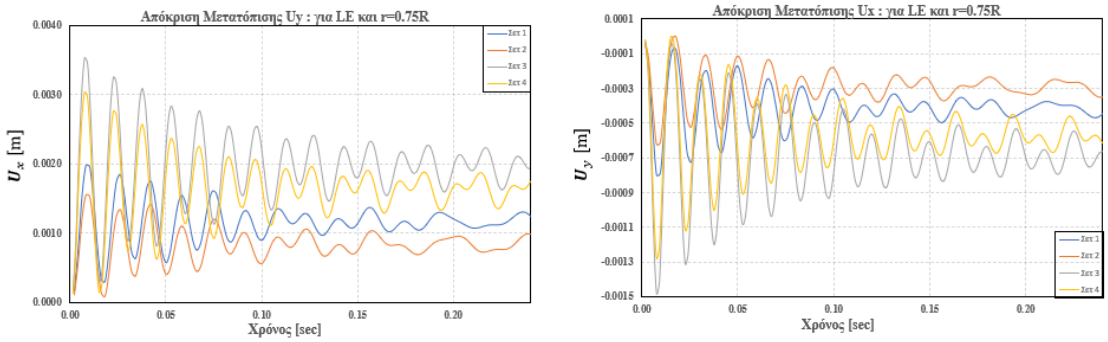

Figure 4. 15 Displacement response, for point on the Leading Edge on the propeller's blade, in position 0.75R (a) axis y (b) axis x

In Figure 4.19, the response of the maximum displacement in the y-direction and the maximum Von Mises stress for the FSI (Fluid-Structure Interaction) system and the Computational Structural

Dynamics (CSD) system, where no aerodynamic loads are applied, is presented. The equivalent Von Mises stresses, σ_{von}, are a theoretical quantity used to determine if there is leakage in a ductile material or to define the fatigue life.

Von Mises stresses, based on reference [4], are calculated using the equation:

$$\sigma_{von} = \sqrt{\frac{\left(\left(\sigma_{xx} - \sigma_{yy}\right)^2 + \left(\sigma_{yy} - \sigma_{zz}\right)^2 + \left(\sigma_{zz} - \sigma_{xx}\right)^2 + 6\left(\sigma_{xy}^2 + \sigma_{yz}^2 + \sigma_{zx}^2\right)\right.}{2}}$$

As seen in Figure 4.19, when considering only the centrifugal force in our solution, the system converges to a steady value for the permanent state. In contrast, as we saw previously, applying aerodynamic loads results in a stable periodic oscillation of the response in the permanent state. Aerodynamic loads act as excitation for the structure, as there are no other external forces to excite it. Removing these loads leads to a constant response.

Additionally, we observe that the response for the centrifugal force alone exhibits higher-frequency oscillations compared to the aeroelastic problem and a slower convergence rate to the permanent state. Therefore, we can say that aerodynamic loads serve as a form of damping for the structure, leading to periodic responses. This introduced damping effect will become more evident when formulating the equations in the 5th chapter, where we will see that the damping matrix includes contributions from the aerodynamic loads.

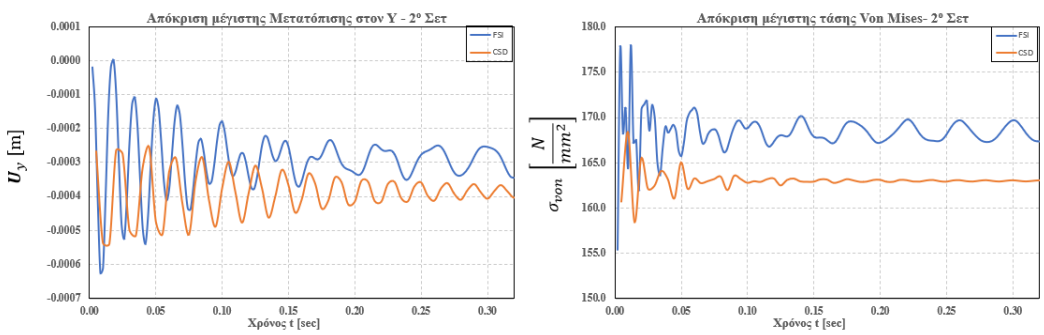

Figure 4. 16 Displacement response and Von Misses stresses for the systems FSI and CSD

In Figure 4.20, we can observe the responses of the maximum Von Mises stress and the total force acting on the propeller hub for the four sets of values. The oscillatory characteristics of the Von Mises stresses remain the same as those of the displacements. Notably, for sets (3,4), we observe double the values of stresses compared to lower speeds. The frequency of the response in the steady state remains the same as the rotation frequency of the propeller. For the total force on the hub, we notice that it exhibits the same dynamic characteristics as the aerodynamic loads. In other words, it has twice the frequency of the propeller rotation frequency (2 blades - 2 repetitions in the pattern). The higher values of the total force compared to the propeller thrust are due to the inclusion of the centrifugal force.

In Figure 4.21, a color representation of the Von Mises stresses for the propeller blade is presented. This figure also displays the undeformed configuration of the propeller with the units, as indicated by the color bar in the figure, being $\left[\frac{N}{m^2}\right]$. To make the deformation results more readable, the figure

is presented at a scale of x4. In this figure, we can observe the highest stress values, which appear near the propeller hub.

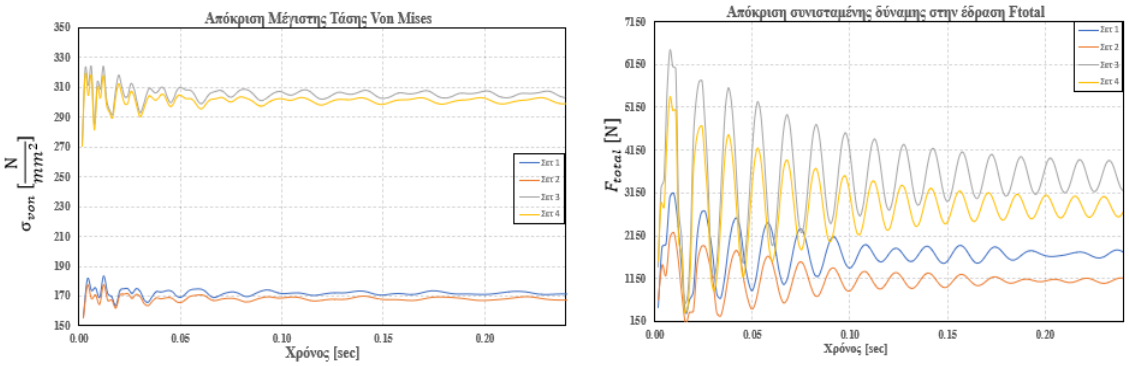

Figure 4. 17 Displacement response for Von Misses stresses and the total force on the support for all 4 set of values.

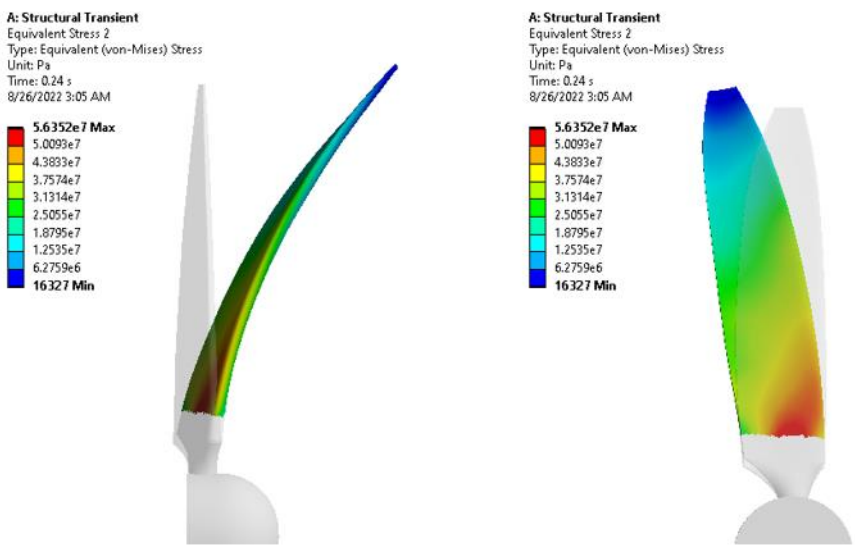

Figure 4. 18 Colored visualization for Von Misses stresses distribution on the propeller's blade at horizontal position.

4.8 Comparison FSI – CFD

In this section, we compare the results of the fluid-structure interaction (FSI) analysis with those of the aerelastic analysis. Specifically, we compare the contents of the harmonic components for the two problems and the distributions of the pressure coefficient for the same cross-sections.

<u>Aerodynamic Load's harmonic components</u>

In Table 4.5, the harmonic components for the loads resulting from the Fourier analysis are presented. In this table, we compare the results from the computational fluid dynamics (CFD) analysis (3rd chapter) with the results from the aeroelastic analysis of the propeller, specifically for the thrust load (T) and the bending loads about the rotation axis (M_z) and the plane of rotation (M_z). Values of interest are marked in yellow on the table.

It's noticeable that the static loads (0P), computed from the CFD analysis, are greater than the loads from the aeroelastic analysis. Specifically, for high rotational speeds, near the resonant region with the structure (2000 rpm - with 1st mode), the bending moment load M_z, although the thrust remains relatively stable, is five times larger in CFD than in the FSI system. The deformation of the structure leads to a more uniform distribution of forces and thus smaller moments.

Even though the static values decrease, the 2P components for the bending loads, which are the most critical for the integrity of the structure, remain of the same order of magnitude as those from CFD. Conversely, the 2P components of the thrust load, for high rotational speeds, are halved. Finally, from the values in this table, we observe a significant reduction (10 to 100 times) in the oscillation ranges of the other harmonic components (1P, 3P).

In general, we can conclude that the deformability of the structure results in the absorption of a certain amount of energy from the aerodynamic loads. Furthermore, with the freedom for the cross-sections to deform and adapt to reduce variations in force distributions (mainly thrust), the resultant moments are reduced.

Table 4. 5. Results comparison from the Fourier analysis for both CFD and FSI models

Set	1o				2o				3o				4o			
Model	CFD	FSI	CFD	FSI	CFD	FSI	CFD	FSI	CFD	FSI	CFD	FSI	CFD	FSI	CFD	FSI
Load	T	T	Mz	Mz	T	T	Mz	Mz	T	T	Mz	Mz	T	T	Mz	Mz
Component																
0P	1720	1720	37.1	41.9	1120	1099	34.9	14	3476	3546	77.8	16.7	2839	2813	77.8	7.97
1P	2.38	2	5.25	2	2.7	1.2	6	0.75	1.9	1.99	10.3	5.3	3.7	2.59	10.3	1.3
2P	28	34	53.6	54.8	33	28	62	59.3	35.8	2.87	99.7	90	39.8	14.55	99.7	101
3P	4.2	0.1	5.7	0.21	1.5	0.06	1	0.0057	4.4	0.247	10	0.25	0.18	0.127	10	0.33

Pressure Coefficient Distribution

In Figure 4.22, the distributions of the Pressure Coefficient are presented for a cross-section of the propeller at a distance of r=0.75R for the 2nd and 4th sets of simulation values (1500-2000 rpm, 30 m/s). The values of the pressure coefficients differ very slightly between them, with an expected small decrease in the coefficient for the deformable structure. The differences in the values are attributed to the change in the Pitch angle of the propeller during deformation. According to the model calculations, the reduction in the angle of attack for the cross-section located at a distance of r=0.75R from the hub is approximately 0.21 degrees. This nose-down rotation of the cross-section may also be due to the fact that the aerodynamic center for this specific cross-section of the propeller is located behind the elastic axis. The aerodynamic center is the point at which the lift and drag forces act on each cross-section.

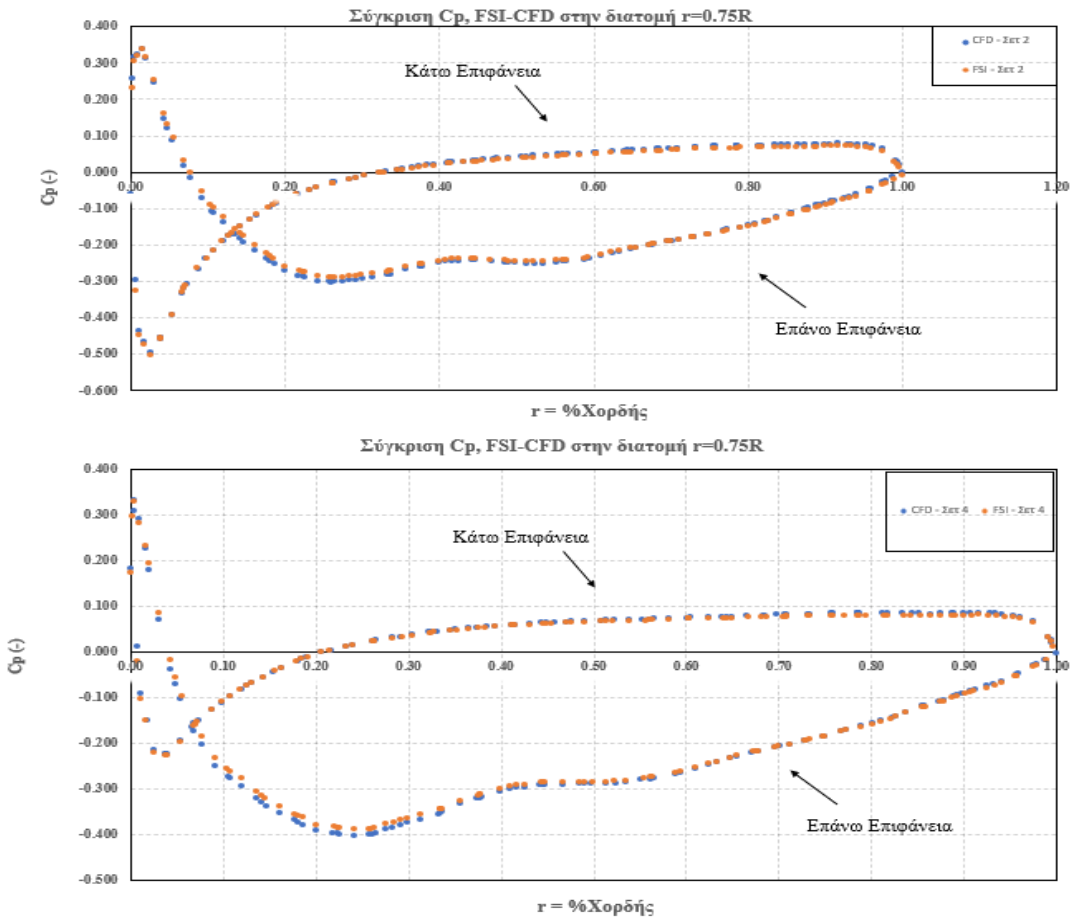

Figure 4. 19. Pressure coefficient distribution comparison for the cross sections at positions θέση $r = 0.75R$, for the 2nd and the 4th simulation value set.

5. PPARAMETRIC STABILITY ANALYSIS - WHIRL FLUTTER

In the previous chapters, we focused on aeroelastic calculations, mainly response-based, using commercial software. In this chapter, we investigate a dynamic aeroelastic phenomenon called whirl flutter and compute our solution using analytical methods. Whirl flutter phenomena are distinct from aeroelastic responses in that they depend on the characteristics of the system rather than the applied load. The phenomenon we study is known as whirl flutter, which can often be catastrophic for aircraft with large rotating masses, potentially leading to engine or even wing failure. For our specific model, we analyze this phenomenon for turboprop engines. The differentiation from other applications (e.g., helicopters, tilt-rotor aircraft) lies in the simplifications introduced in the equations of the phenomenon due to the smaller size of rotating bodies and lower relative velocities.

First, we describe the gyroscopic effects affecting our system. Then, we present a comprehensive analysis of whirl flutter. After providing the theoretical foundations, we proceed with the formulation of the Lagrange equations. Subsequently, using these equations, we derive the system's equations, where aerodynamic forces are analytically calculated based on the 'Strip Theory.' In the final part of the theory, we present the method for solving the system, both for stability boundaries and response computation, concluding with the presentation and discussion of the problem's diagrams. A more detailed presentation of gyroscopic phenomena, Lagrange's equations, and the solution process for the system can be found in reference [1]. Meanwhile, the analysis of the "Whirl Flutter" phenomenon and the "Strip Theory" are presented in reference [9].

5.1 Gyroscopic Phenomena and Analytical Dynamics

In this section, the significance and function of gyroscopic precession are analyzed, and furthermore, the formulation of the Lagrange equations is conducted, which will be necessary for generating the equations of the phenomenon.

<u>Gyroscopic Precession</u>

The presentation of gyroscopic phenomena will be brief, based on the simplified problem of axisymmetric rigid bodies, emphasizing only the aspects that are relevant to the phenomenon under study. We consider a solid body symmetric about one of its axes, let's say the Oz axis. The origin of the coordinate system for the coordinate systems is defined as the center of mass of the solid. With this choice, we decouple the rotational from the translational motion component. The axis of symmetry of the body is also a principal axis of inertia of the solid. Furthermore, we assume that the other two axes (Ox and Oy) are also principal axes of inertia. Thus, the inertia matrix becomes diagonal with moments of inertia $\left(I_{xx}^{O} = I_{yy}^{O}\ \kappa\alpha\iota\ I_{zz}^{O}\right)$. After applying Euler's laws, we obtain the equations of motion for the system in the form :

$$M_x = I_{xx}\dot{\omega}_x + \left(I_{zz} - I_{yy}\right)\omega_y\omega_z$$

$$M_y = I_{yy}\dot{\omega}_y + (I_{xx} - I_{zz})\omega_z\omega_x$$

$$M_z = I_{zz}\dot{\omega}_z + \left(I_{yy} - I_{xx}\right)\omega_x\omega_y = I_{zz}\dot{\omega}_z$$

The above system is a system of nonlinear ordinary differential equations of the first order with respect to angular velocities, which are expressed in the fixed coordinate system attached to the rigid body. In the same coordinate system, the inertia moments are also expressed. This allows us to have constant values throughout the entire motion.

The angular velocities in the above equations are defined based on the Euler angles, which constitute an artificial coordinate system, based on which the orientation of a rigid body is determined and are presented in Figure 5.1. The coordinate systems are all fixed at the center O, and the sequence of rotations follows this order.

1. Rotation of F(OXYZ) around axis OZ magnitude φ (precession) → new position $f'(Oz'y'z')$
2. Rotation of f' around axis Ox' magnitude θ (tilt) → new position $f''(Ox''y''z'')$
3. Rotation of f'' around axis Oz'' magnitude ψ (rotation) → new position $f(Oxyz)$

Based on this sequence and the principle of superposition, the angular velocity of the solid is calculated as follows:

$$\underline{\omega} = \dot{\varphi}\ \underline{e_Z} + \dot{\theta}\ \underline{e_{x'}} + \dot{\psi}\underline{e_{z''}}$$

Next, we project this vector onto the axes of the f system (Oxyz) in order to calculate the components of the angular velocity in the f coordinate system:

$$\omega_x = \underline{\omega} \cdot \underline{e_x}\ , \omega_y = \underline{\omega} \cdot \underline{e_y}\ , \omega_z = \underline{\omega} \cdot \underline{e_z}$$

After performing these operations, the expressions for the components of the angular velocity in the f coordinate system are obtained:

$$\begin{cases} \omega_x = \dot{\theta}\ cos\psi + \dot{\varphi}\ \sin\theta\ sin\psi \\ \omega_y = -\dot{\theta} sin\psi + \dot{\varphi}\ \cos\psi\ sin\theta \\ \omega_z = \dot{\psi} + \dot{\varphi}\ cos\theta \end{cases}$$

Substituting these equations into the Euler equations gives us the system of equations for rotational motion of an axisymmetric solid body rotating about its axis of symmetry :

$$\begin{cases} M_x = I\left(\ddot{\theta} - \dot{\varphi}^2 \sin(\theta)\cos(\theta)\right) + I_{zz}^{O}\dot{\varphi}\left(\dot{\varphi}cos\theta + \dot{\psi}\right)\sin(\theta) \\ M_y = I\left(\ddot{\varphi}\sin(\theta) - 2\dot{\varphi}\dot{\theta}\cos(\theta)\right) - I_{zz}^{O}\dot{\theta}\left(\dot{\varphi}cos\theta + \dot{\psi}\right) \\ M_z = I_{zz}\left(\ddot{\varphi}cos\theta - \dot{\varphi}\dot{\theta}\sin(\theta) + \ddot{\psi}\right) \end{cases} \qquad (III)$$

where $I = I_{xx}^{O} = I_{yy}^{O}$.

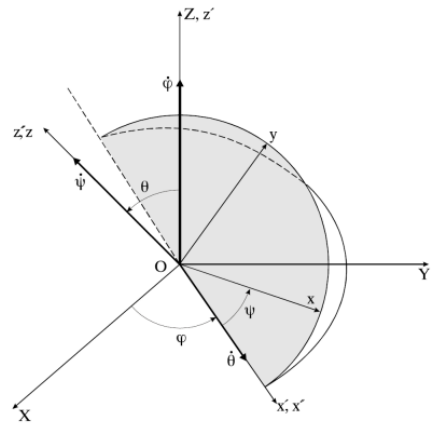

Figure 5. 1 Euler Angles

Solving these equations leads to the calculation of Euler angles and thus determines the orientation of the solid body. Now, let's apply the above equations to the system presented in Figure 5.2. This system is used in aircraft for measuring their rotation and constitutes a permanent gyrostabilization system. For the state of permanent precession (based on the Euler angles), it holds that:

$$\theta = \theta_0 = 90° \,, \varphi = \dot{\varphi}_0 \,, \psi = \dot{\psi}_0$$

That is, the angular velocity with respect to the O'x axis is zero, and with respect to the other two Euler axes, it has a constant magnitude. For the system in Figure 5.2, we have a constant angular velocity with respect to z $(\omega = \dot{\psi}_0)$. The springs on which the cylinder is mounted have the same stiffness k, and the angular velocity about the Z axis is $(\Omega = \dot{\varphi}_0)$. Application of the equations of the system (III) gives us:

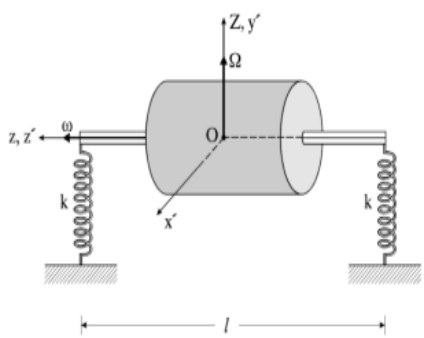

Figure 5. 2 System with gyroscopic precession

$$M_{x''} = I_{zz}^{O}\dot{\varphi}_0 \, \dot{\psi}_0 \underline{e}_{x''} = I_{zz}^{O}\omega \, \Omega \underline{e}_{x''}$$

$$\Rightarrow \Omega = \frac{M_{x''}}{\omega I_{zz}^{O}} \quad (\mathbf{5.1})$$

The result we have obtained for the analysis of whirl flutter is of great significance. Equation (5.1) tells us that when an axisymmetric body (such as a propeller and hub) rotates about its axis of symmetry (the propeller's rotation axis), applying a torque about an axis perpendicular to the axis of symmetry (torque in the planes of propeller rotation) results in the body's precession (rotation φ) about an axis perpendicular to the plane defined by the previous two axes. This behavior is known as the law of gyroscopic precession.Due to this result, as we will see later, there is coupling between the different degrees of freedom of the propeller, resulting in the complex motion of whirl flutter.

Lagrangian Dynamics

In describing our model, as was done in previous chapters, we need to formulate the equations that govern the system. Generally, there are two approaches one can take to formulate the dynamics equations of a mechanical system. The first approach is called vectorial (or Newtonian) dynamics, which uses Newton's and Euler's equations in their vector form to describe the translational and rotational components of a body's motion. The second approach is called analytical dynamics and is constructed using Lagrange's equations. These equations are expressed in terms of the system's dynamics and kinetic energies (scalar quantities).

Both methodologies are equivalent in the final solutions they provide. The choice between them depends on the system under consideration and the results one wants to observe.

In Newtonian dynamics, the equations of motion for complex systems or multi-body systems are generated by analyzing each component separately, often necessitating the calculation of forces resulting from the system's kinematic constraints.

On the other hand, analytical dynamics, utilizing scalar quantities, formulates and solves the equations of motion by considering the system as a whole. This approach eliminates the need to calculate the forces arising from kinematic constraints.

The application of analytical dynamics relies on defining generalized coordinates and the formulation and solution of Lagrange's equations. A detailed breakdown of the equations and principles governing analytical dynamics can be found in reference [1].

Generalized coordinates (q_n) are defined as any set of variables capable of fully defining the position of a body. These coordinates are mathematical concepts. In the general case, the motion of a dynamic system can be subject to k constraints in the form of:

$$f_i(q_1, \dots., q_n, t) = 0 \ , \ \ i = 1,2 \dots k$$

In the context described, constraints of the form:

$$f_i(q_i, \dots., q_n, t) \geq 0 \ \ , \qquad f_i(q_i, \dots, q_n, \dot{q}_i, \dots, \dot{q}_n, t) = 0$$

are referred to as holonomic constraints. These constraints can be further categorized into holonomic, rheonomous (time-dependent), and scleronomic (time-independent) constraints. The distinction between them lies in whether these constraints can be integrated to reduce the degrees of freedom of the system.

Holonomic constraints can be expressed in terms of generalized coordinates and, in some cases, generalized velocities. By taking derivatives of these holonomic constraints, we can represent them in the form:

$$\frac{\partial \underline{f}}{\partial \underline{q}} \, \underline{\dot{q}} = A\left(\underline{q}\right) \underline{\dot{q}} = \underline{0}$$

This representation is known as the Pfaffian form, where A is the Jacobian matrix of the constraints, and it has the form:

$$A\left(\underline{q}\right) = \begin{pmatrix} \frac{\partial f_1}{\partial q_1} & \cdots & \frac{\partial f_1}{\partial q_n} \\ \vdots & \ddots & \vdots \\ \frac{\partial f_k}{\partial q_1} & \cdots & \frac{\partial f_k}{\partial q_n} \end{pmatrix}$$

The equations of motion in analytical dynamics are derived using the principle of virtual work (also known as the principle of possible displacements). This principle considers virtual displacements, which are arbitrary but consistent with the system's constraints at a specific instant in time. The difference between actual displacements ($d\underline{r}$) and virtual displacements ($\delta\underline{r}$) is that actual displacements occur over finite time intervals where the system's constraints and forces may change.

The differentiation between these two types of displacements is essential for deriving the equations of motion and understanding the dynamics of systems with constraints. The principle of virtual work forms the foundation for the Lagrangian method, which is widely used to formulate and solve equations of motion for mechanical systems.

The principle of virtual work begins with the consideration that for a system with N material points, which is in static equilibrium, the work done by the applied forces and the forces arising from constraints is zero :

$$\delta W = \sum_{i=1}^{N} \left(\underline{R}_i' + \underline{f}_i \right) \delta \underline{r}_i \ \ , \ \ where \ \ \underline{R}_i' = 0 \ they \ don't \ do \ work$$

Based on D'Alembert's principle, the concept is extended to dynamic systems by considering that the forces acting on the system are composed of the applied forces (f_i) and the inertial forces ($\mathrm{m}_i \ddot{\underline{r}}_i$). Therefore, we have:

$$\sum_{i=1}^{N} \left(\underline{f}_i - \mathrm{m}_i \ddot{\underline{r}}_i \right) \delta \underline{r}_i = 0 \ \Rightarrow \delta W + \delta W_{in} = 0 \, , \ \ \delta W_{in} = \sum_{i=1}^{N} \left(- \mathrm{m}_i \ddot{\underline{r}}_i \right) \delta \underline{r}_i$$

Using the principle of virtual work (D'Alembert's principle) and a transformation between the coordinates of Newtonian dynamics and the generalized coordinates in the form $\underline{r}_i = \underline{r}_i(q_1, \dots, q_n, t)$, we arrive at the expression:

$$\sum_{j=1}^{n} \left[\frac{d}{dt} \left(\frac{\partial T}{\partial \dot{q}_j} \right) - \frac{\partial T}{\partial q_j} - Q_j \right] \delta q_j = 0 \quad (\mathbf{5.2})$$

where Q_j are the general forces which are calculated from the equation: $Q_j = \sum_{i=1}^{N} f_i \frac{\partial \underline{r}_i}{\partial q_j}$.

Considering our system holonomic and the generalized coordinates q_j independent of each other, we can set the coefficients of the above sum to zero. Thus, we have:

$$\frac{d}{dt} \left(\frac{\partial T}{\partial \dot{q}_j} \right) - \frac{\partial T}{\partial q_j} = Q_j (\mathbf{5.3})$$

These equations are the well-known Equations of Lagrange, with T representing the kinetic energy of the system $and \ Q_j$ as the generalized forces. A different formulation of (5.3) expresses the generalized forces as a sum of viscous and non-viscous forces, taking the form:

$$\frac{d}{dt} \left(\frac{\partial L}{\partial \dot{q}_j} \right) - \frac{\partial L}{\partial q_j} + \frac{\partial D}{\partial \dot{q}_j} = Q_j^{nv} \quad (\mathbf{5.4})$$

In the general case, the Lagrangian function L is defined as:

$$L(q_j, \dot{q}_j, t) = T(q_j, \dot{q}_j, t) - V(q_j, t)$$

where V represents the potential energy of the system. Q_j^{nv} is defined as the non-viscous generalized forces. The viscous forces are introduced into (5.4) through the term $\frac{\partial D}{\partial \dot{q}_j}$,, where D is the Rayleigh dissipation function in the form:

$$D = \frac{1}{2}\sum_{i=1}^{n}\sum_{j=1}^{n} c_{ij}\dot{q}_i\dot{q}_j$$

If we have non-holonomic constraints in the system, the generalized coordinates are not independent of each other. Therefore, we cannot go from equation (5.2) to equation (5.3). However, if these constraints can be expressed in Pfaffian form, as presented earlier, we can address the problem and set the coefficients of (5.2) to zero, resulting in the following form:

$$\frac{d}{dt}\left(\frac{\partial L}{\partial \dot{q}_j}\right) - \frac{\partial L}{\partial q_j} + \frac{\partial D}{\partial \dot{q}_j} = Q_j^{nv} + A^T\left(\underline{q}\right)\underline{\lambda}_{[kx1]} \quad (\mathbf{5.5})$$

Here, λ represents the vector of Lagrange multipliers, which express the magnitude of forces arising from the respective constraints. The system (5.5) constitutes a system of 6xn differential equations (6 degrees of freedom for n bodies) with (6xn+k) unknowns. Along with the constraint equations in their Pfaffian form, it can be solved to calculate the generalized coordinates and Lagrange multipliers. We have now completed the derivation of the Lagrange equations.

In this chapter, we will work with equations in the form of (5.4) since we do not have non-holonomic constraints, and we are not concerned with calculating the forces on the supports. In the next chapter, we will present the phenomenon of Whirl Flutter.

5.2 Whirl Flutter and excited loads

5.2.1 Whirl Flutter Phenomenon

The phenomenon known as Whirl Flutter (WF), also referred to as gyroscopic flutter, as briefly mentioned in Chapter 4, falls into the category of dynamic aeroelastic stability phenomena. It primarily occurs in turboprop engines or, more generally, in rotating systems with significant mass, such as helicopter rotors. Its occurrence is due to the deformable action of the engine on the aircraft's wing. The rotating masses increase the degrees of freedom of the system and generate additional forces (centrifugal forces, Coriolis forces, gyroscopic torques).

The main problem encountered in such systems is the uneven distribution of thrust along the propeller blades, which oscillate flapwise. The classical solution, considered the simplest, is based on the assumption of a rigid propeller and can provide good results for applications in turboprop aircraft where the natural frequencies of the propeller are much higher than the frequencies of the disturbance.

For large turboprop engines, such as large military aircraft or aircraft with tilt-rotor configurations, determining the stability boundaries requires taking into account the deformability of the rotating

bodies. In this analysis, we will address the simplified problem of a rigid propeller and work with the model of classical WF.

For the classical model (or even the two degrees of freedom model), we replace the engine's action on the wing with two torsional springs with constants$K_\psi, K_\theta$for the two additional degrees of freedom, known as Yaw (ψ) and Pitch (θ). This is illustrated in Figure 5.3α. The propeller rotates with an angular velocity Ω with respect to the x-axis, as shown in the figure. If we don't consider the rotation of the propeller and the aerodynamic forces, two independent modes with natural frequencies ω_θ $\kappa\alpha\iota$ ω_ψ, emerge. These are depicted in Figures 5.3β and 5.3γ, with the first one being associated with twisting in the y-direction (Pitch), and the second one with twisting in the z-direction (Yaw).

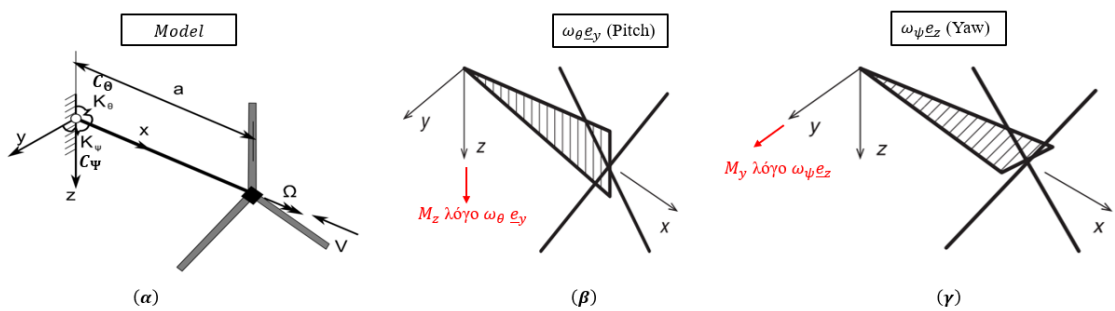

Figure 5. 3 (α) Benchmark model (2 DOF's) whirl flutter, (β) Eigenmode Dof Pitch (γ) Eigenmode Dof Yaw

When we take into account the rotating propeller, the motion of the system becomes the characteristic gyroscopic motion, and the eigenmodes result from the coupling of the independent modes of the previous figure. This coupling leads to the characteristic motion of the Whirl Flutter phenomenon.

This coupling of the two aforementioned motions results in the propeller axis (x) tracing an elliptical trajectory with varying semi-axes in the plane of rotation. The direction of motion for the propeller axis is opposite to the rotation direction (backward whirl mode) for the mode with the lower natural frequency, and it's in the same direction (forward) for the mode with the higher frequency. These motions correspond to the low-speed and high-speed gyroscopic precession of the system and are shown in Figure 5.4. Increasing the rotational speed of the propeller (Ω) increases the difference between the natural frequencies of the system for the two conditions (backward and forward).

The eigenmodes of gyroscopic motion we've described up to this point are quite complex, as the independent modes of the propeller (Figure 5.3) have a 90-degree phase difference between them.

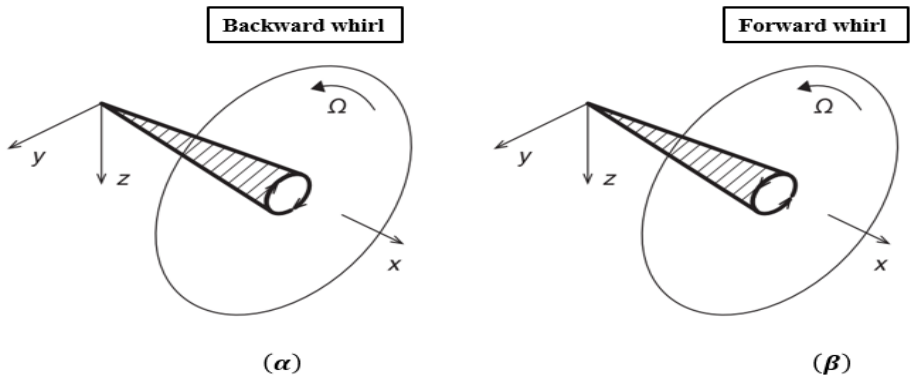

Figure 5. 4 Eigenmodes excited from the gyroscopic motion (α) Anti – phase (β) In – phase

The gyroscopic motion of the propeller causes changes in the angle of attack of its blades. This, in turn, leads to the development of non-uniform aerodynamic forces, which under specific conditions can result in the instability phenomenon known as WF (Whirl Flutter). Generally, instability can occur only during reverse elliptical motion (backward motion). In Figure 5.5, the system under study is presented in a stable state ($V_\infty < V_{FL}$) and an unstable state ($V_\infty > V_{FL}$). V_{FL} is defined as the critical free-stream airspeed at which the WF phenomenon occurs. When we are in the stable speed range, motion is damped out of the system (Figure 5.5α), whereas, conversely, for speeds greater than V_{FL} (Figure 5.5β), the flapping amplitudes increase with time. For the critical condition with $V_\infty = V_{FL}$, the overall damping of the system is zero.

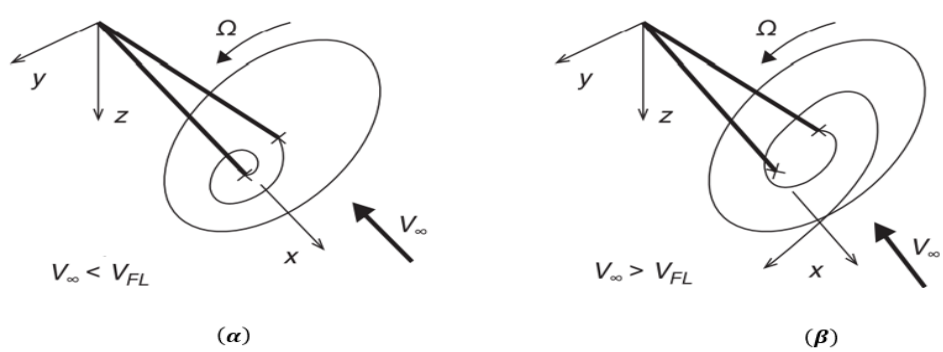

Figure 5.5 (α) Stable and (β) Unstable state of gyroscopic oscillations for the backward flutter mode.

Our model, for finding stability boundaries, can be solved either analytically or through computational methods. When applying computational methods, we need to follow the same steps as we did in Chapter 4, but with the difference that the problem constraints, grids, and solution methods differ. Due to the long computation times for many different parameter sets that we seek to calculate the system's behavior, we resort to analytical procedures with the introduction of some basic simplifications. The advantage of analytical formulation and solution of equations is that we can easily modify the parameters and observe the system's behavior.

5.2.2 Propeller's loads analysis

To describe the characteristics of aerodynamic forces, we rely on the principles of "quasi-steady" theory, assuming that the displacements of the degrees of freedom are small. This allows us to make some simplifications to the model. Since the gyroscopic motions that develop for both degrees of freedom (ψ, θ) have the same character, we will analyze the forces only for the rotation θ (pitch axis).

Considering the propeller with an inclination with respect to the free stream, as shown in Figure 5.6α, we analyze the velocity in components parallel to the free stream velocity and in the plane of propeller rotation (perpendicular to V). By observing Figures 5.6γ and δ, it can be seen that the RHS (Right Hand Side) part of the propeller produces greater lift compared to the LHS (Left Hand Side). This results in the development of the torque $M_z(\Theta)$ (Figure 5.6β), which is called yaw torque due to its direction along the axis where it acts. Additionally, due to the uneven distribution of forces ΔF developed on the airfoils shown in Figures 5.6γ and δ, there is also a vertical force on the same axis, $P_z(\Theta)$.

The torque $M_z(\Theta)$ has the same direction as the angular velocity $\omega_\psi \underline{e_z}$, for backward motion of the propeller. This implies that the nature of this torque tends to destabilize the system.

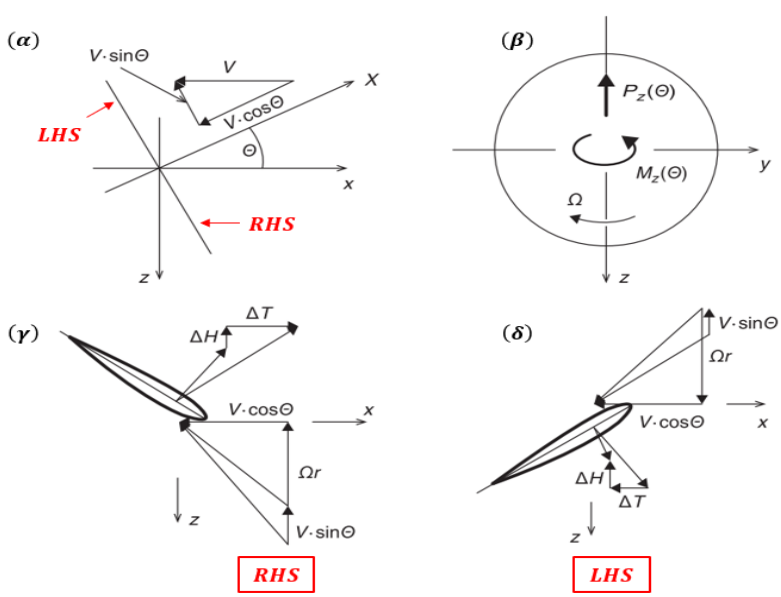

Figure 5. 5 Aerodynamic loads excited from the propeller's displacement θ (pitch).

In addition to the forces generated due to the inclination angle Θ, there are also forces resulting from the rotational velocity $\omega_\theta \underline{e_y} = \dot{\theta}\underline{e_y}$as shown in Figure 5.7. The airfoil cross-sections presented in Figures 5.7γ and δ correspond to a horizontal position of the airfoils.

The angular velocity $\dot{\Theta}$affects the air encountering the propeller, as depicted in Figure 5.7α, resulting in the development of the torque $M_Y(\dot{\Theta})$ (Figure 5.7β) with a direction opposite to the angular velocity $\dot{\Theta}$. Additionally, due to the forces ΔF developed on the airfoils in Figures 5.7γ and δ, a force $P_Y(\dot{\Theta})$ is created, acting in the -y direction. This force is responsible for coupling the motions around the z and y axes.

All the forces presented so far, which are due to changes in the angle Θ, also occur for changes in the angle Ψ with the exact same behavior $\left(M_y(\Psi), P_y(\Psi), M_z(\dot{\Psi}), P_z(\dot{\Psi})\right)$.

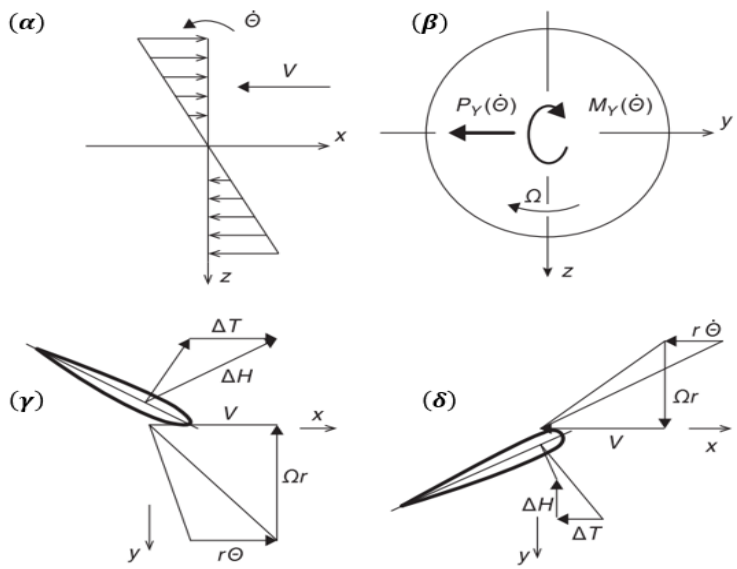

Figure 5.6 Aerodynamic loads caused by the angular velocity $\dot{\Theta}\underline{e}_y$

In general, concerning the aerodynamic forces generated due to the gyroscopic motion of the propeller, we can say that the most significant ones related to the WF phenomenon are the torque due to the deflection of the angle Θ ($M_Z(\Theta)$ yaw torque) and the torque due to the deflection of the angle Ψ ($M_y(\Psi)$ pitch torque). The next section will provide the formulation of the system's equations.

5.3 Formulation of the system's equations

5.3.1 Equations of Motion – Lagrange

To formulate the equations of motion according to the theory of analytical dynamics presented earlier, we need to calculate the kinetic and dynamic energy of the system, after first defining the system of generalized coordinates that will be capable of fully expressing the orientation of our model. Our system consists of the propeller designed in Chapter 2. Additionally, we model the remaining engine components as a cylindrical solid body, with one end supporting the propeller and the other end where the cylinder is connected to the aircraft's wing. The model is shown in Figure 5.8a. Introducing the cylindrical geometry into our model allows us to include the contribution of the remaining engine components to the total moment of inertia. The interaction between the engine and the wing is modeled with two torsional springs, as mentioned previously.

In Figure 5.8b, the kinematic scheme and the forces resulting from the gyroscopic motion are depicted. The subscript "P" for the torques in the figure means that the corresponding torque is located on the plane of rotation of the propeller. Three angles (Θ, Ψ, φ) are defined as generalized coordinates, corresponding to the pitch, yaw, and the propeller's rotational axis, respectively. Two coordinate systems are defined, one rigidly attached to the propeller (OXYZ) and the other attached to the model-wing interaction (f: O'xyz), which is considered the inertial reference frame. The angles Θ and Ψ represent the Euler angles of the system and relate the coordinate system attached to the body to the inertial frame. The sequence of rotations that transforms the inertial system f into the rotating system F is as follows:

1) Rotation pitch (θ) on axis y for the inertial reference frame, which transforms our system to $(O\tilde{x}yZ)$
2) Rotation yaw (ψ) on axis Z for the frame f, which transforms our system to F: $(OXYZ)$

The total angular velocity of the system includes 3 vectors: the rate of change of pitch ($\dot{\theta}$), the rate of change of yaw ($\dot{\psi}$), and the rotational velocity of the propeller $\dot{\varphi} = \Omega$, as shown in Figure 5.8b. The kinetic energy of the system is calculated with respect to the coordinate system attached to the propeller (F: OXYZ) as follows:

$$T = \frac{1}{2}J_X\omega_X^2 + \frac{1}{2}J_Y\omega_Y^2 + \frac{1}{2}J_Z\omega_Z^2 \quad (\mathbf{5.6})$$

Where:

- J_x is the polar moment of inertia of the propeller.

- J_y, J_z are the total mass moments of inertia of the system about the Y and Z axes, respectively.

- $\omega_X, \omega_Y, \omega_Z$ are the angular velocities of the system in the coordinate system of the propeller.

In the above expression for kinetic energy, the kinetic energies of the rotating components of the engine could also be introduced. However, due to their small size compared to the terms mentioned above, they are neglected. The calculation of the moments of inertia is determined by applying Steiner's parallel-axis theorem between the local coordinate systems of each member located at the mass centers and the coordinate system rotating with the propeller. The application of the Steiner theorem yields the moments of inertia :

$$J_x = (I_{xx}^{cm})_1 + (I_{xx}^{cm})_2$$

$$J_y = \left(I_{yy}^{cm}\right)_1 + \left(I_{yy}^{cm}\right)_2 + (m_2 d_2^2)$$

$$J_y = (I_{zz}^{cm})_1 + (I_{zz}^{cm})_2 + (m_2 d_2^2)$$

Where the subscript 1 refers to the propeller, while the subscript 2 refers to the other components of the engine (cylindrical body). Here, \(d_2\) represents the distance between the center of mass of the cylinder and the system located at the center of the propeller, F.

To express angular velocities in the rotating system F with respect to angular velocities in the inertial system f, we will need to define the rotation matrix. This matrix serves as the coordinate transformation between the f and F systems. Our goal is to arrive at a relationship in the form:

$$\underline{\omega} = \begin{bmatrix} \omega_X \\ \omega_Y \\ \omega_Z \end{bmatrix} = T \begin{bmatrix} \dot{\varphi} \\ \dot{\theta} \\ \dot{\psi} \end{bmatrix}$$

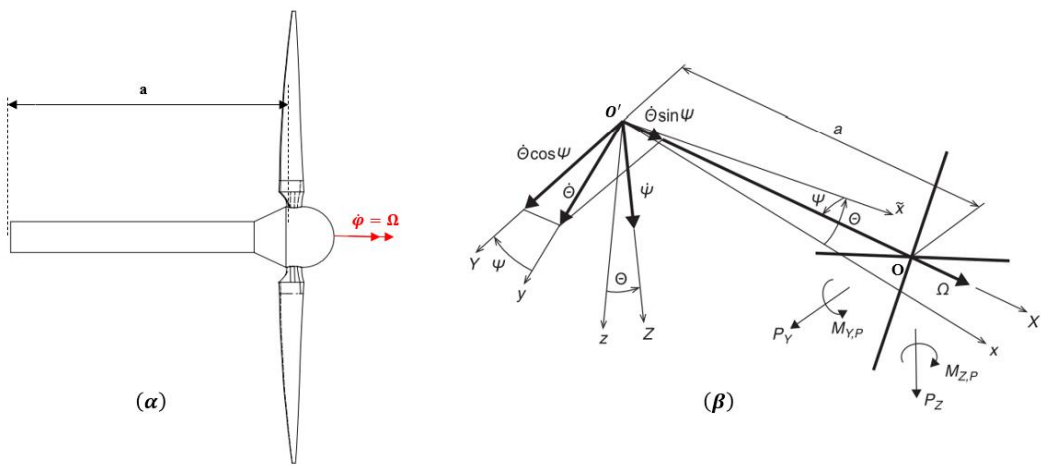

Figure 5. 7 (α) 2D model design for our system (β) Kinematics scheme and aerodynamic loads excited from the gyroscopic motion of the propeller

Based on the order of rotations on the respective axes presented earlier, the angular velocity is given by the equation $\underline{\omega} = \Omega \underline{e}_X + \dot{\Theta} \underline{e}_y + \dot{\Psi} \underline{e}_Z$ To calculate the components of angular velocity in the F coordinate system, we project the above vector onto the respective axes. Thus, with the help of Figure 5.8β, we have:

$$\omega_X = \underline{\omega} \cdot \underline{e}_X = \Omega + \dot{\Theta}\sin(\Psi)\ , \omega_Y = \underline{\omega} \cdot \underline{e}_Y = \dot{\Theta}\cos(\Psi)\ , \omega_Z = \underline{\omega} \cdot \underline{e}_Z = \dot{\Psi}$$

In matrix form :

$$\underline{\omega} = \begin{bmatrix} \omega_X \\ \omega_Y \\ \omega_Z \end{bmatrix} = \begin{bmatrix} 1 & \sin(\Psi) & 0 \\ 0 & \cos(\Psi) & 0 \\ 0 & 0 & 1 \end{bmatrix} \begin{bmatrix} \dot{\varphi} \\ \dot{\theta} \\ \dot{\psi} \end{bmatrix} = T \begin{bmatrix} \dot{\varphi} \\ \dot{\theta} \\ \dot{\psi} \end{bmatrix}$$

Based on quasi – steady theory, the oscillation's amplitudes are small ($\Psi \ll 1$), so the following simplifications apply:

$$\sin(\Psi) \approx \Psi \ \kappa\alpha\iota \cos(\Psi) \approx 1$$

Also, we consider $\dot{\Theta}^2\dot{\Psi}^2 \ll \Omega^2$. Based on the above simplifications and applying the transform T for the Kinetic Energy (5.6), we get :

$$T = \frac{1}{2}J_X\Omega^2 + J_X\Psi\Omega\dot{\Theta} + \frac{1}{2}\left(J_Y\dot{\Theta}^2 + J_Z\dot{\Psi}^2\right) \ (\mathbf{5.7})$$

The dynamic energy of the system arises from the deformations of the torsional springs at the engine mounting, with respect to the directions of the pitch and yaw angles. Thus, we have:

$$V = \frac{1}{2}K_\Theta\Theta^2 + \frac{1}{2}K_\Psi\Psi^2 \ (\mathbf{5.8})$$

At this point, we introduce damping into the structure. Damping in the structure is determined through experiments, but generally, there are many different methodologies for defining approximate damping for a system. In this specific problem, we introduce classical damping, which is used in flutter instability analyses. In this case, the damping force is proportional to the square of the corresponding angular velocities (Θ, Ψ).

$$D = \frac{1}{2}C_\Theta\dot{\Theta}^2 + \frac{1}{2}C_\Psi\dot{\Psi}^2 \ (\mathbf{5.9})$$

Where the damping coefficients for the independent motions of pitch and yaw are C_Θ and C_Ψ, respectively. By introducing equations (5.7), (5.8), and (5.9) into the Lagrange equations (5.4) and applying the equation for calculating generalized forces, we obtain the equations of motion for the system.

$$J_Y\ddot{\Theta} + C_\Theta\dot{\Theta} + J_X\Omega\dot{\Psi} + K_\Theta\Theta = Q_\Theta \ \ (\mathbf{5.10})$$

$$J_Z\ddot{\Psi} + C_\Psi\dot{\Psi} - J_X\Omega\dot{\Theta} + K_\Psi\Psi = Q_\Psi \ \ (\mathbf{5.11})$$

Where the generalized forces:

$$Q_\Theta = M_{Y,P} - aP_z \ \ \kappa\alpha\iota \ Q_\Psi = M_{Z,P} + aP_Y$$

The problem with the above equations is the calculation of the aerodynamic forces. These forces can be expressed using dimensionless aerodynamic coefficients. These coefficients are calculated either analytically or experimentally. Subsequently, we formulate the equations for the aerodynamic forces and compute the aerodynamic coefficients using the "Strip Theory" approach.

5.3.2 Aerodynamic loads - Strip Theory

The two-dimensional formulation of this theory was developed in 1935 and was extended to three-dimensional problems in 1942. The logic behind this method is to divide the structure into workstations (strips) along the wingspan and calculate the aerodynamic forces on each such segment. These forces are calculated based on the two-dimensional aerodynamic coefficients (C_L, C_D) of the discrete segments. Additionally, it assumes that there is no interaction between different stations.

We consider the following variables (system disturbances): the local angle of attack of each station (α_1), the velocity in the plane of propeller rotation ($\dot{s}$), and the velocity out of the plane ($\dot{w}$). Figure 5.9α shows a propeller with 4 blades in arbitrary positions. The correction for the number of blades, for our propeller (2 blades), will be made after formulating the equations. Besides the displacement of the propeller in the z-y plane, we also have the rotations of the propeller in pitch (Θ) and yaw (Ψ) angles. Referring to Figure 5.9α, for blade number 1, the change in the geometric angle of attack will be as follows.

$$a_1 = \Psi \sin(\Omega t) - \Theta \cos(\Omega t) \quad (\mathbf{5.12})$$

The disturbances ($\dot{s}$), ($\dot{w}$) for an arbitrary point on the propeller 1, are derived from the deriviation of the following geometric equations:

$$\begin{cases} y = y_1 + rcos(\Omega t) \\ z = z_1 + rsin(\Omega t) \\ w_1 = -\Psi rcos(\Omega t) - \Theta rsin(\Omega t) \end{cases}$$

$$\Rightarrow \begin{cases} \dot{s}_1 = -\dot{y}_1 \sin(\Omega t) + \dot{z}_1 \cos(\Omega t) \quad (\mathbf{5.13}) \\ \dot{w}_1 = -\dot{\Psi} rcos(\Omega t) + \Psi r\Omega \sin(\Omega t) - \dot{\Theta} rsin(\Omega t) - \Theta r\Omega \cos(\Omega t) \quad (\mathbf{5.14} \end{cases}$$

In Figure 5.9β, the velocities developed at an arbitrary section of blade 1 are depicted. The angle β in this figure represents the angle of attack of the propeller for steady-state operation (without disturbances). Based on this figure, the effective angle of attack of the section, which is the angle at which the aerodynamic forces are ultimately generated, is calculated using the following relationship:

$$\alpha_{eff} = \boldsymbol{\alpha_0} + a_1 - \dot{w}\left(\frac{\Omega r}{U^2}\right) + \dot{s}\left(\frac{V_\infty}{U^2}\right) \quad (\mathbf{5.15})$$

where α_0 is the slope of the lift curve of the section, and the term $\dot{w}\left(\frac{\Omega r}{U^2}\right) + \dot{s}\left(\frac{V_\infty}{U^2}\right)$ arises from the disturbances component in the direction perpendicular to the velocity U, which is the resultant velocity at the section $U = (r^2\Omega^2 + V_\infty^2)$. Similarly, from the component of disturbances parallel to U, we have the effective velocity U_{eff},, which is the velocity from which the aerodynamic forces ultimately depend:

$$U_{eff} = U + \dot{w}\left(\frac{V_\infty}{U}\right) + \dot{s}\left(\frac{\Omega r}{U}\right) \quad (\mathbf{5.16})$$

Using the above equation and application of the aerodynamic equations for the 2D cross section. We calculate the forced lift on this cross section from :

$$L = \frac{1}{2} a_0 \rho c_0 U^2 \left[\boldsymbol{\alpha_0} + \underbrace{a_1 - \frac{\Omega r}{U^2}\left(1 - \frac{2V_\infty}{\Omega r}\boldsymbol{\alpha_0}\right)\dot{w} + \frac{V}{U^2}\left(1 + \frac{2\Omega r}{V_\infty}\boldsymbol{\alpha_0}\right)\dot{s}}_{\textbf{Μη μόνιμοι όροι άντωσης}} \right] \quad (\mathbf{5.17})$$

where c_0 is the section's chord. On the above equation we can observe that the non – steady terms are dependent on the AOA of steady state ($\boldsymbol{\alpha_0}$).

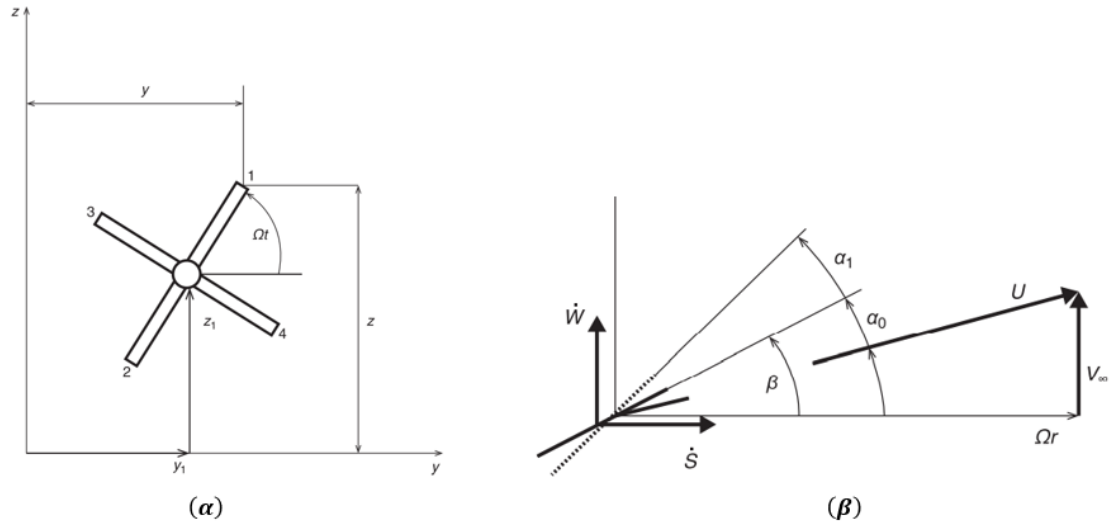

Figure 5. 8 (α) Propeller in arbitrary pose (β) Blade's cross section velocities in arbitrary pose

The terms $\frac{2V_\infty}{\Omega r}\boldsymbol{\alpha_0}$, $\frac{2\Omega r}{V_\infty}\boldsymbol{a_0}$ in equation (5.17) have very small contributions to the thrust and can be neglected. Additionally, for windmilling operation, we have $\boldsymbol{a_0} \approx 0$. In the windmilling state, there is no introduction of any rotational velocity to the propeller; instead, it rotates due to the relative airspeed. Furthermore, we express the resultant velocity at the section as $U = (r^2\Omega^2 + V_\infty^2)$, and we substitute equations (5.12), (5.13), and (5.14). This leads us to equation.

$$L = -\frac{1}{2}a_0\rho c_0\left(V_\infty^2\Theta - V_\infty\dot{z}_1 - \Omega r^2\dot{\Psi}\right)\cos(\Omega t) + \frac{1}{2}a_0\rho c_0\left(V_\infty^2\Psi - V_\infty\dot{y}_1 + \Omega r^2\dot{\Theta}\right)\sin(\Omega t) \Rightarrow$$

$$\Rightarrow L = -f_1\cos(\Omega t) + f_2\sin(\Omega t) \quad (\mathbf{5.18})$$

$$\therefore\ f_1 = \frac{1}{2}a_0\rho c_0\left(V_\infty^2\Theta - V_\infty\dot{z}_1 - \Omega r^2\dot{\Psi}\right),\quad f_2 = \frac{1}{2}a_0\rho c_0\left(V_\infty^2\Psi - V_\infty\dot{y}_1 + \Omega r^2\dot{\Theta}\right)$$

Equation (5.18) calculated the section's Lift (station) for the blade 1 on figure 5.9a. For the rest blades we have:

$\Omega t \rightarrow (\Omega t + \pi)$ blade number 2 $L_2 = f_1\cos(\Omega t) - f_2\sin(\Omega t) = -L_1$ $(\mathbf{5.19})$

$\Omega t \rightarrow \left(\Omega t + \frac{\pi}{2}\right)$ blade number 3 $L_3 = f_1\sin(\Omega t) + f_2\cos(\Omega t)$ $(\mathbf{5.20})$

$\Omega t \rightarrow \left(\Omega t + \frac{3\pi}{2}\right)$ blade number 4 $L_2 = f_1\sin(\Omega t) - f_2\cos(\Omega t) = -L_3$ $(\mathbf{5.21})$

For the calculation of the unsteady aerodynamic forces, we analyze the induction of each blade in the rotational direction of the propeller around the x-axis (thrust term) and in the plane of rotation of the propeller around the y-z axes (torque term). The thrust term results in the development of moments $(\Delta M_y, \Delta M_z)$, and the torque term results in the development of forces $(\Delta L_y, \Delta L_z)$. Based on Figure 5.9β, these terms can be expressed for thrust as $\left(L\left(\frac{\Omega r}{U}\right)\right)$ and for torque as $\left(L\left(\frac{V_\infty}{U}\right)\right)$. These components, for the blade with number 1, are presented in Figure 5.10. The expressions for the calculation of all terms $(\Delta M_y, \Delta M_z, \Delta L_y, \Delta L_z)$ are derived:

$$\begin{cases} \Delta L_y = 2\dfrac{V_\infty}{U}(L_1\sin(\Omega t) + L_3\cos(\Omega t)) \\ \Delta L_z = \dfrac{V_\infty}{U}(-L_1\cos(\Omega t) + L_3\sin(\Omega t)) \\ \Delta M_y = -2\dfrac{\Omega r^2}{U}(L_1\sin(\Omega t) + L_3\cos(\Omega t)) = -\dfrac{\Omega r^2}{V_\infty}\Delta L_y \\ \Delta M_z = 2\dfrac{\Omega r^2}{U}(-L_1\cos(\Omega t) + L_3\sin(\Omega t)) = \dfrac{\Omega r^2}{V_\infty}\Delta L_z \end{cases}$$

Replacing equations (5.18) to (5.21) into the above system yields:

$$\begin{cases} \Delta L_y = 2\dfrac{V_\infty}{U}(-f_1\cos(\Omega t)\sin(\Omega t) + f_2\sin^2(\Omega t) + f_1\sin(\Omega t)\cos(\Omega t) + f_2\cos^2(\Omega t)) = 2\dfrac{V_\infty}{U}f_2 \\ \Delta L_z = \dfrac{V_\infty}{U}(f_1\cos^2(\Omega t) - f_2\sin(\Omega t)\cos(\Omega t) + f_1\sin^2(\Omega t) + f_2\cos(\Omega t)\sin(\Omega t)) = 2\dfrac{V_\infty}{U}f_1 \\ \Delta M_y = -2\dfrac{\Omega r^2}{U}f_2 \\ \Delta M_z = 2\dfrac{\Omega r^2}{U}f_1 \end{cases}$$

$\Rightarrow$

$$\Rightarrow \begin{cases} \Delta L_y = 2\frac{V_\infty}{U}f_2 \\ \Delta L_z = 2\frac{V_\infty}{U}f_1 \\ \Delta M_y = -2\frac{\Omega r^2}{U}f_2 \\ \Delta M_z = 2\frac{\Omega r^2}{U}f_1 \end{cases} \quad (\mathbf{5.22})$$

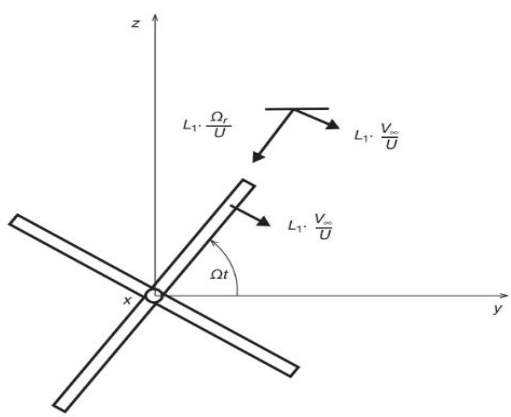

Figure 5. 9 Force components for the blade's (num 1) cross-section.

Now, replacing the expressions for the coefficients f_1 and f_2 from equation (5.18), we obtain the system of forces at an arbitrary section of the blades in a form that will help us continue the analysis.

$$\Rightarrow \begin{cases} \Delta L_y = a_0 \rho c_0 \dfrac{V_\infty}{U}\left(V_\infty^2 \Psi - V_\infty \dot{y}_1 + \Omega r^2 \dot{\Theta}\right) \\ \Delta L_z = a_0 \rho c_0 \dfrac{V_\infty}{U}\left(V_\infty^2 \Theta - V_\infty \dot{z}_1 - \Omega r^2 \dot{\Psi}\right) \\ \Delta M_y = -a_0 \rho c_0 \dfrac{\Omega r^2}{U}\left(V_\infty^2 \Psi - V_\infty \dot{y}_1 + \Omega r^2 \dot{\Theta}\right) \\ \Delta M_z = a_0 \rho c_0 \dfrac{\Omega r^2}{U}\left(V_\infty^2 \Theta - V_\infty \dot{z}_1 - \Omega r^2 \dot{\Psi}\right) \end{cases} \quad (\mathbf{5.23})$$

To calculate the total forces on the propeller acting at its hub, we will need to integrate the equations of the system (5.23) from the hub to the tip of the blades. For this reason, we define the geometric integrals of the blade as follows:

$$\begin{cases} A_1 = \displaystyle\int_0^1 \frac{c_0}{c_r} \frac{\mu^2}{\sqrt{\mu^2 + \eta^2}} d\eta \\ A_2 = \displaystyle\int_0^1 \frac{c_0}{c_r} \frac{\mu \eta^2}{\sqrt{\mu^2 + \eta^2}} d\eta \\ A_3 = \displaystyle\int_0^1 \frac{c_0}{c_r} \frac{\eta^4}{\sqrt{\mu^2 + \eta^2}} d\eta \end{cases} \quad (\mathbf{5.24})$$

Where c_r is the reference chord length of the blade (at the base), μ is the tip speed ratio, defined as $\mu = \frac{V_\infty}{\Omega R} = \frac{J_0}{\pi}$, and η is the dimensionless radius of the blades, defined as $\eta = \frac{r}{R}$. . At this point, it should be noted that the above integrals use the slope of the lift curve $\boldsymbol{\alpha_0} = 2\pi$. This value will be corrected later in the process. When solving the system to calculate stability limits, these integrals, due to their smoothness, are computed as a sum in the form $A_1 = \sum_{i=1}^{N} \frac{\mu^2}{\sqrt{\mu^2+\eta_i^2}} (\eta_i - \eta_{i-1})$, after first dividing the propeller blade into N discrete segments. In Figure 5.11, value diagrams of the integrals from the system (5.24) are presented for a range of μ values, where the smoothness along the length of the propeller blade can be observed.

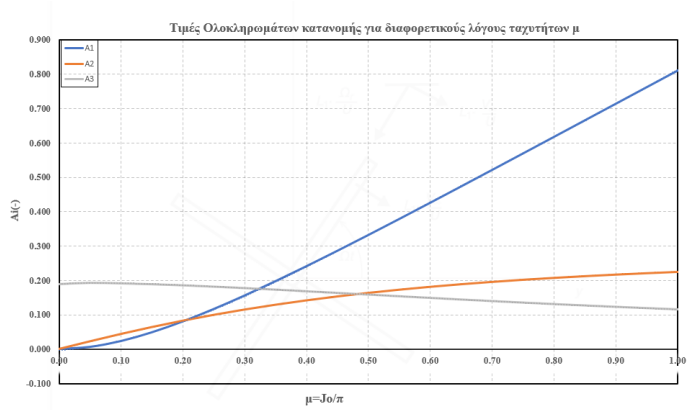

Figure 5. 10 Distribution integral values for different μ.

Integrating equations (5.23) with the integrals (5.24) calculated the total aerodynamic forces and moments which are forces on the propeller's hub, with the following expressions:

$$P_y = q_\infty F_p \left[\frac{4\Omega^2 R c_r}{V_\infty^2}\mu A_1 \Psi - \frac{4\Omega c_r}{V_\infty} A_1 \frac{\dot{y}_1}{V_\infty} + \frac{4\Omega R}{V_\infty} A_2 \frac{\dot{\Theta} c_r}{V_\infty}\right] \quad (\mathbf{5.25})$$

$$P_z = q_\infty F_p \left[\frac{4\Omega^2 R c_r}{V_\infty^2}\mu A_1 \Theta - \frac{4\Omega c_r}{V_\infty} A_1 \frac{\dot{z}_1}{V_\infty} - \frac{4\Omega R}{V_\infty} A_2 \frac{\dot{\Psi} c_r}{V_\infty}\right] \quad (\mathbf{5.26})$$

$$M_{Y,P} = q_\infty F_p R \left[-\frac{4\Omega^2 R c_r}{V_\infty^2}\mu A_2 \Psi + \frac{4\Omega c_r}{V_\infty} A_2 \frac{\dot{y}_1}{V_\infty} - \frac{4\Omega R}{V_\infty} A_3 \frac{\dot{\Theta} c_r}{V_\infty}\right] \quad (\mathbf{5.27})$$

$$M_{Z,P} = q_\infty F_p R \left[\frac{4\Omega^2 R c_r}{V_\infty^2}\mu A_2 \Theta - \frac{4\Omega c_r}{V_\infty} A_2 \frac{\dot{z}_1}{V_\infty} - \frac{4\Omega R}{V_\infty} A_3 \frac{\dot{\Psi} c_r}{V_\infty}\right] \quad (\mathbf{5.28})$$

Where $q_\infty = \frac{1}{2}\rho V_\infty$ the dynamic pressure coefficient for the free flow, $F_p = \frac{D_p^2 \pi}{4}$ surface of the propeller's rotational disk, R propeller's radius. Based on the quasi-steady theory, the magnitude of the oscillations for angles Θ,Ψ are small. So, the effective angles in the directions pitch and yaw are calculated from the following equations:

$$\Theta^* = \Theta - \frac{\dot{z}_1}{V_\infty} = \Theta - \frac{a\dot{\Theta}}{V_\infty} \ \kappa\alpha\iota \ \Psi^* = \Psi - \frac{\dot{y}_1}{V_\infty} = \Psi - \frac{a\dot{\Psi}}{V_\infty}$$

The indices on the velocities z and y are based on the notations in Figure 5.9α. The active angle is defined as the angle that, in reality, due to the rotation and translation of the propeller, will ultimately contribute to the aerodynamic loads. By equating now between them the two different expressions for each one of the active angles, we have:

$$\dot{z}_1 = a\dot{\Theta} \ \ \kappa\alpha\iota \ \ \dot{y}_1 = a\dot{\Psi}$$

Substituting these expressions into equations (5.25) to (5.28) and writing the coefficients of the equations using the aerodynamic coefficients, we get:"

$$\begin{cases} P_y = q_\infty F_p \left[c_{y\Psi}\Psi - c_{y\Psi}\frac{a\dot{\Psi}}{V_\infty} + c_{yq}\frac{\dot{\Theta}R}{V_\infty}\right] \\ P_z = q_\infty F_p \left[c_{z\Theta}\Theta - c_{z\Theta}\frac{a\dot{\Theta}}{V_\infty} + c_{zr}\frac{\dot{\Psi}R}{V_\infty}\right] \\ M_{Y,P} = q_\infty F_p R \left[c_{m\Psi}\Psi - c_{m\Psi}\frac{a\dot{\Psi}}{V_\infty} + c_{mq}\frac{\dot{\Theta}R}{V_\infty}\right] \\ M_{Z,P} = q_\infty F_p R \left[c_{n\Theta}\Theta - c_{n\Theta}\frac{a\dot{\Theta}}{V_\infty} + c_{nr}\frac{\dot{\Psi}R}{V_\infty}\right] \end{cases} \quad (\mathbf{5.29})$$

- $c_{y\Psi} = \frac{4\Omega c_r}{V_\infty} A_1$, $c_{yq} = \frac{4\Omega c_r}{V_\infty} A_2$,
- $c_{z\Theta} = \frac{4\Omega c_r}{V_\infty} A_1$, $c_{zr} = -\frac{4\Omega c_r}{V_\infty} A_2$
- $c_{m\Psi} = -\frac{4\Omega c_r}{V_\infty} A_2$, $c_{mq} = -\frac{4\Omega c_r}{V_\infty} A_3$
- $c_{n\Theta} = \frac{4\Omega c_r}{V_\infty} A_2$, $c_{nr} = -\frac{4\Omega c_r}{V_\infty} A_3$

- $\Lambda_1 = q_\infty F_p R \ , \ \Lambda_2 = q_\infty F_p \alpha$

Substitution of the above relations in the equations of motion (5.10) and (5.11), we get :

$$J_Y \ddot{\Theta} + C_\Theta \dot{\Theta} + J_X \Omega \dot{\Psi} + K_\Theta \Theta = \left(\Lambda_1 \left[c_{m\Psi} \Psi - c_{m\Psi} \frac{a\dot{\Psi}}{V_\infty} + c_{mq} \frac{\dot{\Theta} R}{V_\infty} \right] \right) - \left(\Lambda_2 \left[c_{z\Theta} \Theta - c_{z\Theta} \frac{a\dot{\Theta}}{V_\infty} + c_{zr} \frac{\dot{\Psi} R}{V_\infty} \right] \right)$$

$$J_Z \ddot{\Psi} + C_\Psi \dot{\Psi} - J_X \Omega \dot{\Theta} + K_\Psi \Psi = \left(\Lambda_1 \left[c_{n\Theta} \Theta - c_{n\Theta} \frac{a\dot{\Theta}}{V_\infty} + c_{nr} \frac{\dot{\Psi} R}{V_\infty} \right] \right) + \left(\Lambda_2 \left[c_{y\Psi} \Psi - c_{y\Psi} \frac{a\dot{\Psi}}{V_\infty} + c_{yq} \frac{\dot{\Theta} R}{V_\infty} \right] \right)$$

In a Matrix form:

$$\begin{bmatrix} J_Y & 0 \\ 0 & J_Z \end{bmatrix} \begin{bmatrix} \ddot{\Theta} \\ \ddot{\Psi} \end{bmatrix} + \begin{bmatrix} C_\Theta & 0 \\ 0 & C_\Psi \end{bmatrix} \begin{bmatrix} \dot{\Theta} \\ \dot{\Psi} \end{bmatrix} + \begin{bmatrix} 0 & J_X \Omega \\ -J_X \Omega & 0 \end{bmatrix} \begin{bmatrix} \dot{\Theta} \\ \dot{\Psi} \end{bmatrix} + \begin{bmatrix} K_\Theta & 0 \\ 0 & K_\Psi \end{bmatrix} \begin{bmatrix} \Theta \\ \Psi \end{bmatrix}$$
$$= \begin{bmatrix} \left(\Lambda_1 c_{mq} \frac{R}{V_\infty} + \Lambda_2 c_{z\Theta} \frac{a}{V_\infty} \right) & \left(-\Lambda_1 c_{m\Psi} \frac{a}{V_\infty} - \Lambda_2 c_{zr} \frac{R}{V_\infty} \right) \\ \left(-\Lambda_1 c_{n\Theta} \frac{a}{V_\infty} + \Lambda_2 c_{yq} \frac{R}{V_\infty} \right) & \left(\Lambda_1 c_{nr} \frac{R}{V_\infty} - \Lambda_2 c_{y\Psi} \frac{a}{V_\infty} \right) \end{bmatrix} \begin{bmatrix} \dot{\Theta} \\ \dot{\Psi} \end{bmatrix}$$
$$+ \begin{bmatrix} \Lambda_2 c_{z\Theta} & \Lambda_1 c_{m\Psi} \\ \Lambda_1 c_{n\Theta} & \Lambda_2 c_{y\Psi} \end{bmatrix} \begin{bmatrix} \Theta \\ \Psi \end{bmatrix} \Rightarrow$$

$$\Rightarrow [M] \begin{bmatrix} \ddot{\Theta} \\ \ddot{\Psi} \end{bmatrix} + [D] \begin{bmatrix} \dot{\Theta} \\ \dot{\Psi} \end{bmatrix} + [G] \begin{bmatrix} \dot{\Theta} \\ \dot{\Psi} \end{bmatrix} + [K] \begin{bmatrix} \Theta \\ \Psi \end{bmatrix} = [D^A] \begin{bmatrix} \dot{\Theta} \\ \dot{\Psi} \end{bmatrix} + [K^A] \begin{bmatrix} \Theta \\ \Psi \end{bmatrix}$$

Where :

- Propeller's mass matrix $[M] = \begin{bmatrix} J_Y & 0 \\ 0 & J_Z \end{bmatrix}$
- Propeller's damping matrix $[D] = \begin{bmatrix} C_\Theta & 0 \\ 0 & C_\Psi \end{bmatrix}$
- Gyroscopic matrix $[G] = \begin{bmatrix} 0 & J_X \Omega \\ -J_X \Omega & 0 \end{bmatrix}$
- Stiffness matrix $[K] = \begin{bmatrix} K_\Theta & 0 \\ 0 & K_\Psi \end{bmatrix}$
- Aerodynamic damping matrix $[D^A] = \begin{bmatrix} \left(\Lambda_1 c_{mq} \frac{R}{V_\infty} + \Lambda_2 c_{z\Theta} \frac{a}{V_\infty} \right) & \left(-\Lambda_1 c_{m\Psi} \frac{a}{V_\infty} - \Lambda_2 c_{zr} \frac{R}{V_\infty} \right) \\ \left(-\Lambda_1 c_{n\Theta} \frac{a}{V_\infty} + \Lambda_2 c_{yq} \frac{R}{V_\infty} \right) & \left(\Lambda_1 c_{nr} \frac{R}{V_\infty} - \Lambda_2 c_{y\Psi} \frac{a}{V_\infty} \right) \end{bmatrix}$
- Aerodynamic stiffness matrix $[K^A] = \begin{bmatrix} \Lambda_2 c_{z\Theta} & \Lambda_1 c_{m\Psi} \\ \Lambda_1 c_{n\Theta} & \Lambda_2 c_{y\Psi} \end{bmatrix}$

Μεταφέροντας όλους τους όρους του συστήματος στα αριστερά, έχουμε :

$$[M] \begin{bmatrix} \ddot{\Theta} \\ \ddot{\Psi} \end{bmatrix} + ([D] + [G] - [D^A]) \begin{bmatrix} \dot{\Theta} \\ \dot{\Psi} \end{bmatrix} + ([K] - [K^A]) \begin{bmatrix} \Theta \\ \Psi \end{bmatrix} = [0]_{2x1} \quad (\mathbf{5.30})$$

From the above system of equations, we can observe that the aerodynamic forces contribute to both stability and damping of the system. We will closely monitor this behavior when presenting the diagrams later. Additionally, a particularity of the above damping and stability matrices is that the former is asymmetric, and the latter is antisymmetric. This asymmetry affects both the methodology for calculating stability limits and the dynamic behavior of the system, as we will see below.

At this point, we need to introduce correction factors for the integrals (5.24) with respect to the number of blades (2 for us) and the lift curve slope factor α_0, which we assumed to have a constant

value of 2π. Furthermore, because at some points of our propeller we have high Mach numbers and so far, we have not considered compressibility effects in the analysis, we need to introduce a coefficient that accounts for compressibility effects into the above equations. For the number of blades, we multiply the integrals by the factor $\frac{N_b}{4}$, where $N_b = 2$ is the number of blades. Thus, for us, the integrals take the following form:

$$\begin{cases} A_1 = \dfrac{N_b}{4}\displaystyle\int_0^1 \dfrac{c_0}{c_r}\dfrac{\mu^2}{\sqrt{\mu^2+\eta^2}}d\eta \\ A_2 = \dfrac{N_b}{4}\displaystyle\int_0^1 \dfrac{c_0}{c_r}\dfrac{\mu\eta^2}{\sqrt{\mu^2+\eta^2}}d\eta \\ A_3 = \dfrac{N_b}{4}\displaystyle\int_0^1 \dfrac{c_0}{c_r}\dfrac{\eta^4}{\sqrt{\mu^2+\eta^2}}d\eta \end{cases} \quad (\mathbf{5.31})$$

Compressibility can be introduced into the integrals using two coefficients. Based on the Prantl-Glauert correction for compressibility, using the local Mach number $\left(M_r = \frac{\sqrt{V_\infty^2+\Omega^2 r^2}}{\alpha}\right)$,, we have the first coefficient as $\frac{1}{\sqrt{1-M_r^2}}$.. The second coefficient takes into account the finite dimensions of the blades and is derived from the equation:

$$\frac{A_r\sqrt{1-M_r^2}}{2+A_r\sqrt{1-M_r^2}} \quad , \qquad \mu\varepsilon \;\; A_r = \frac{R}{c_r\int_0^1\left(\frac{c}{c_r}\right)d\eta} = dimensions\; ratio\; for\; the\; blade$$

Based on the above and expressing the coefficients in terms of the Mach number of free flow, $M = \frac{V_\infty}{a}$, we have the following.

$$\frac{1}{\sqrt{1-M_r^2}}\frac{A_r\sqrt{1-M_r^2}}{2+A_r\sqrt{1-M_r^2}} = \frac{A_r}{2+A_r\sqrt{1-M_r^2}} = \frac{A_r}{2+A_r\sqrt{1-M^2\left(1+\frac{\eta^2}{\mu^2}\right)}} \quad (\mathbf{5.32})$$

Introducing the coefficient (5.32) into the integrals (5.31), we get:

$$\begin{cases} I_1 = A_r \dfrac{N_b}{4} \displaystyle\int_0^1 \dfrac{c_0}{c_r} \dfrac{\mu^2}{\sqrt{\mu^2+\eta^2}\left[2 + A_r\sqrt{1 - M^2\left(1+\dfrac{\eta^2}{\mu^2}\right)}\right]} d\eta \\ I_2 = A_r \dfrac{N_b}{4} \displaystyle\int_0^1 \dfrac{c_0}{c_r} \dfrac{\mu\eta^2}{\sqrt{\mu^2+\eta^2}\left[2 + A_r\sqrt{1 - M^2\left(1+\dfrac{\eta^2}{\mu^2}\right)}\right]} d\eta \\ I_3 = A_r \dfrac{N_b}{4} \displaystyle\int_0^1 \dfrac{c_0}{c_r} \dfrac{\eta^4}{\sqrt{\mu^2+\eta^2}\left[2 + A_r\sqrt{1 - M^2\left(1+\dfrac{\eta^2}{\mu^2}\right)}\right]} d\eta \end{cases} \quad (\mathbf{5.33})$$

The equations of the system remain in the same form (5.30), but the aerodynamic coefficients become as follows:

- $c_{y\Psi} = \frac{4\Omega c_r}{V_\infty} I_1$, $c_{yq} = \frac{4\Omega c_r}{V_\infty} I_2$,
- $c_{z\Theta} = \frac{4\Omega c_r}{V_\infty} I_1$, $c_{zr} = -\frac{4\Omega c_r}{V_\infty} I_2$
- $c_{m\Psi} = -\frac{4\Omega c_r}{V_\infty} I_2$, $c_{mq} = -\frac{4\Omega c_r}{V_\infty} I_3$
- $c_{n\Theta} = \frac{4\Omega c_r}{V_\infty} I_2$, $c_{nr} = -\frac{4\Omega c_r}{V_\infty} I_3$

Having formulated the equations of the system, we can proceed to solve them to find the stability boundaries. The following methodology will be applied to determine the stability boundaries and calculate the response of the propeller hub. Before that, we will describe the specific dynamic characteristics of the system of motion equations that were derived.

5.4 Solution – Non-symmetric Matrices

<u>Stability study</u>

We rewrite the system of motion equations for a better understanding of the problem.

$$[M]\begin{bmatrix}\ddot{\Theta}\\ \ddot{\Psi}\end{bmatrix} + ([D] + [G] - [D^A])\begin{bmatrix}\dot{\Theta}\\ \dot{\Psi}\end{bmatrix} + ([K] - [K^A])\begin{bmatrix}\Theta\\ \Psi\end{bmatrix} = [0]_{2x1} \quad (\mathbf{5.30})$$

With the matrices:

$$[M] = \begin{bmatrix} J_Y & 0 \\ 0 & J_Z \end{bmatrix}, [D] = \begin{bmatrix} C_\Theta & 0 \\ 0 & C_\Psi \end{bmatrix}, \ [G] = \begin{bmatrix} 0 & J_X\Omega \\ -J_X\Omega & 0 \end{bmatrix}, [K] = \begin{bmatrix} K_\Theta & 0 \\ 0 & K_\Psi \end{bmatrix},$$

$$[D^A] = \begin{bmatrix} \left(\Lambda_1 c_{mq}\frac{R}{V_\infty} + \Lambda_2 c_{z\Theta}\frac{a}{V_\infty}\right) & \left(-\Lambda_1 c_{m\Psi}\frac{a}{V_\infty} - \Lambda_2 c_{zr}\frac{R}{V_\infty}\right) \\ \left(-\Lambda_1 c_{n\Theta}\frac{a}{V_\infty} + \Lambda_2 c_{yq}\frac{R}{V_\infty}\right) & \left(\Lambda_1 c_{nr}\frac{R}{V_\infty} - \Lambda_2 c_{y\Psi}\frac{a}{V_\infty}\right) \end{bmatrix}, \ [K^A] = \begin{bmatrix} \Lambda_2 c_{z\Theta} & \Lambda_1 c_{m\Psi} \\ \Lambda_1 c_{n\Theta} & \Lambda_2 c_{y\Psi} \end{bmatrix}$$

We can see that the overall damping and stiffness matrices are non-symmetric. This non-symmetry arises from the gyroscopic terms and the aerodynamic damping (which can be considered as a form of internal damping) for the damping matrix, while for the stiffness matrix, it arises from the aerodynamic forces. Due to the dependency of the aerodynamic coefficients on the angular velocity of the propeller, we can anticipate, as we saw in the 4th chapter, that the natural frequencies of the system will be influenced by this velocity. This phenomenon is known as gyroscopic stiffening, and one way to observe it is by using Campbell diagrams. We can apply two methodologies to find the stability boundaries.

The Routh-Hurwitz stability criterion is applied to linear systems and is widely used in control problems. According to this criterion, by following a certain procedure, we can derive inequalities that will give us the stability region. Finally, by visualizing the common regions, we obtain the solution space that leads to a stable system.

The second method, which will be used in this analysis, is the method of eigenvalue analysis. Specifically, for each set of parameters, we will solve the eigenvalue problem repeatedly until we reach a solution with a zero real part of the eigenvalues. At this point, the solution will be stored, and we will proceed with the same process for the next set of parameters. The eigenvalue method is chosen over Routh-Hurwitz due to its algorithmic simplicity.

Due to the asymmetry, the roots (eigenfrequencies) of the characteristic polynomial of the system can be either real or complex conjugate pairs. Furthermore, the corresponding eigenvectors for each eigenvalue can be either real or complex. Because the damping matrix is known, for solving the eigenvalue problem, we define the 2N-dimensional vector, where N is the number of degrees of freedom of the problem (in our case, 2), in the form:

$$\underline{y}(t) = \begin{bmatrix} \underline{\dot{x}}(t) \\ \underline{x}(t) \end{bmatrix}, \mu\varepsilon\ \underline{x}(t) = \begin{bmatrix} \Theta(t) \\ \Psi(t) \end{bmatrix}$$

System (5.30) can be written in the following form:

$$\begin{bmatrix} 0 & M \\ M & D_{total} \end{bmatrix} \underline{\dot{y}}(t) + \begin{bmatrix} -M & 0 \\ 0 & K_{total} \end{bmatrix} \underline{y}(t) = [0]_{4x1} \Rightarrow A\underline{\dot{y}}(t) + B\underline{y}(t) = [0]_{4x1} \quad (\mathbf{5.34})$$

Where:

$$D_{total} = [D] + [G] - [D^A], \quad K_{total} = [K] - [K^A]$$

In the above equation, the matrices A and B are not symmetric. To calculate the eigenfrequencies and eigenvectors, we apply a procedure similar to the method of modal analysis, with some minor differences. We consider a solution to the above system in the form:

$$\underline{y}(t) = \underline{\hat{y}} e^{\lambda t}$$

Substitution of this solution in (5.34), we get :

$$(B + \lambda A)\underline{\hat{y}} = \underline{0} \quad (\mathbf{5.35})$$

To have a nontrivial solution, the determinant of the matrix must be equal to zero $|B + \lambda A| = 0.$, which leads to a polynomial of degree 2N with respect to λ. The eigenvalues of the system will emerge in a complex form:

$$\lambda_n = \mu_n \pm i v_n$$

The eigenvalue with the largest real part corresponds to the backward whirl flutter, while the one with the smallest corresponds to the forward whirl flutter. For our finite bandwidth dynamic system to function, the real part of the eigenvalues must satisfy the condition: $\mu_n \leq 0$ for all n. If the real part is positive, the system is unstable. Specifically, based on linear theory, a positive real part predicts an infinite bandwidth of oscillation, which cancels out the linearity of the problem. In reality, for a positive real part, the system activates nonlinear terms, leading to finite oscillations. If the imaginary part of the eigenvalues is zero v_n = 0 and μ_n > 0, then the bandwidth extends to infinity without oscillation, while for a value other than zero, the approach to infinite bandwidth occurs with oscillatory behavior.

For the aeroelastic problem, considering $v_n \neq 0$ and $\mu_n > 0$, we have dynamic instability of the system (whirl flutter). When $v_n = 0$and $\mu_n > 0$, we have static instability in the system (static divergence), while for $v_n \neq 0$ or $v_n = 0$ and $\mu_n < 0$, the system remains stable. In general, when we are on the boundary of stability, our eigenvalues are either zero (static divergence) or purely imaginary (flutter). Developing the determinant of the system (5.35) will give us a polynomial with both complex and real parts. From the real part, we calculate the natural frequencies of the system $\left(\lambda_{1,2} = \omega_{1,2}^2\right)$ for the two composite modes of the WF.

From a computational perspective, to find the boundaries, we will solve the system while keeping all parameters constant except for the ones under study, which are usually the stiffnesses (K_Θ, K_Ψ) of the actuator. By varying these parameters over a range of values, we calculate the natural frequencies for each pair of these values. When our solution gives a real part of zero for the eigenvalue, we are on the boundary between stability and instability. Then, we check the value of the imaginary part to categorize our solutions as dynamic or static instability.

To better understand the behavior of the WF phenomenon during the presentation of the results, we will calculate the trajectory of the propeller hub. Subsequently, the procedure for computing the response of hub displacements in the y and z directions (rotation plane) will be presented.

<u>Dynamic response</u>

Έχοντας υπολογίσει τις ιδιοτιμές του συστήματος, μπορούμε να υπολογίσουμε την απόκριση των 2 βαθμών ελευθερίας (Θ,Ψ). Η διαφορετική προσέγγιση του ιδιοπροβλήματος ασύμμετρων μητρώων έναντι του κλασικού, έγκειται στο γεγονός ότι θα πρέπει να επιλυθεί το πρόβλημα τόσο για τα μητρώα A, B όσο και για τα ανάστροφα αυτών A^T, B^T. Έτσι οι 2 εξισώσεις που επιλύουμε για την εύρεση των ιδιοδιανυσμάτων (ιδιομορφών) είναι :

Once we have calculated the eigenvalues of the system, we can compute the response of the 2 degrees of freedom (Θ, Ψ). The key difference in approaching the eigenproblem for asymmetric matrices compared to the classical one lies in the fact that we need to solve the problem for both matrices A, B, and their transposes A^T, B^T. Thus, the two equations we solve to find the eigenvectors (eigenmodes) are:

$$(B + \lambda A)\underline{\hat{y}} = \underline{0} \ \ (\mathbf{5.35}) \ \ \ \kappa\alpha\iota \ \ \ \underline{\hat{x}}\,(B^T + \lambda A^T) = \underline{0} \ \ (\mathbf{5.36})$$

The eigenvalues for the above 2 equations are the same, based on the property for transpose matrices $|A|^T = |A^T|$. Reversing equation (5.36), give us:

$$\underline{\hat{x}}(B + \lambda A) = \underline{0} \ \ (\mathbf{5.37})$$

Due to the form of equations (5.35) and (5.36), the eigenvectors $\underline{\hat{x}}$ are called left eigenvectors, and the $\underline{\hat{y}}$ are called right eigenvectors. For these eigenvectors, the orthonormality conditions apply, and by using them, we diagonalize the initial matrices of the system so that we end up with a system of decoupled equations. These conditions are formulated in the form:

$$Y^T MX = \begin{bmatrix} a_1 & \cdots & 0 \\ \vdots & \ddots & \vdots \\ 0 & \cdots & a_{2N} \end{bmatrix} kai\ Y^T BX = \begin{bmatrix} \lambda_1 \alpha_1 & \cdots & 0 \\ \vdots & \ddots & \vdots \\ 0 & \cdots & \lambda_{2N} \alpha_{2N} \end{bmatrix}$$

With N being the number of initial generalized coordinates and the columns of matrices X and Y consisting of left and right eigenvectors, respectively. These vectors are linearly independent. Therefore, we can express the system's response as a linear combination of the eigenvectors in the form:

$$\underline{y}(t) = \sum_{n=1}^{2N} \left(\underline{\hat{y}}_n a_n(t) \right) = Y \underline{a}(t) \quad (\mathbf{5.38})$$

Substituting this relation into the system (5.34), multiplying from the left by the transpose of matrix X^T and from the right by Y, and applying the orthonormality conditions, we obtain a system of 2N decoupled first-order differential equations, expressed with respect to the coordinates $a_n(t)$ in the form:

$$\dot{a}_n - \lambda_n a_n = \underline{h}(t) \ (\mathbf{5.39})$$

Since we don't have excitation in equations (5.34), the vector h(t) is equal to zero $\underline{\mathrm{h}}(\mathrm{t}) = 0$ In order for equation (5.39) to be fully defined, we also calculate the initial conditions for the new coordinates a(t) using the system's eigenvectors in the form:

$$\underline{\mathrm{a}}(0) = \hat{\mathrm{A}}^{-1} \mathrm{Y}^{\mathrm{T}} \mathrm{A} \begin{bmatrix} \underline{\mathrm{V}}_0 \\ \underline{\mathrm{X}}_0 \end{bmatrix} \quad (\mathbf{5.40})$$

After solving the system of differential equations (5.39) using the initial conditions (5.40), we calculate the displacements and velocities of our degrees of freedom from equation (5.38).

A more detailed procedure for computing the response in systems with non-symmetric matrices can be found in reference [2].

Having now calculated the responses of the degrees of freedom (Θ, Ψ), we can compute the displacements z and y for the propeller hub, with the aim of visualizing the trajectory in the rotation plane, using the geometric relationships.

$$z = \sin(\Theta)\, \alpha \quad , \qquad y = \sin(\Psi)\, \alpha$$

After all the above analysis we can eventually proceed to the presentation of our results.

5.5 Results

For the generation of the diagrams presented below, code was written in the **MATLAB** programming language. Initially, the stability boundary diagrams are presented, followed by the system's responses for different parameter sets. It is assumed that the pitch angle (Θ) has an initial value of zero during the solution. Furthermore, the other parameters and properties, for which stability analysis is conducted, are presented in Table 5.1. The moments of inertia of the propeller are calculated from the model implemented in the **ANSYS** Mechanical software in Chapter 4. For the rest of the engine, these values are omitted because, as mentioned earlier, since we model it as a cylinder, its moments of inertia depend on the distance of the propeller action point (a), which is a quantity that will vary during the solution. Specifically, the values for the cylinder, with respect to its center of mass, are derived from the equations:

$$I_{xx}^{cm} = \frac{1}{2} m_2 d_2^2 \ , \ \ I_{yy}^{cm} = I_{zz}^{cm} = \frac{1}{4} m_2 d_2^2 + \frac{1}{12} m_2 a^2 \ , m_2 = \frac{\rho \pi d_2^2}{4} a$$

Table 5. 1 Parameters and Properties for the system

Rotational velocity	$n = 2500\ [rpm]$	Moment of inertia y	$\mathrm{I}_{yy}^{cm} = 8.1\ [kg\ m^2]$
Propeller's distance	$a = 0.55$	Moment of inertia z	$\mathrm{I}_{zz}^{cm} = 8.1\ [kg\ m^2]$
Stiffness coefficient Pitch	$K_\Theta = 70\ [kNm \cdot rad^{-1}]$	Reference chord	$c_r = 0.22\ [m]$
Stiffness coefficient Yaw	$K_\Psi = 70\ [kNm \cdot rad^{-1}]$	Air density	$\rho = 1.225\ \left[\frac{kg}{m^3}\right]$
Viscosity coefficient Pitch	$C_\theta = 0.01\ [Nm \cdot s\ rad^{-1}]$	Material density	$\rho = \ 2770\ \left[\frac{kg}{m^3}\right]$
Viscosity coefficient Yaw	$C_\Psi = 0.01\ [Nm \cdot s\ rad^{-1}]$	Sound velocity	$\alpha \approx 340\ \left[\frac{m}{s}\right]$
Moment of inertia x	$\mathrm{I}_{xx}^{cm} = 0.4\ [kg\ m^2]$	Propeller's mass	$58.472\ [kg]$

From the above table we can observe that the units, for the stiffness and damping coefficient, include the unit $\left(\frac{1}{rad}\right)$ because we are referring to torsional springs.

<u>Stability Diagrams</u>

In Figure 5.12, the stability boundaries are presented for different values of stiffness at the mounting for the rotational springs. The diagrams shown correspond to three different airspeeds in free flow. The axes of the diagram are expressed in terms of the independent natural frequencies (of the decoupled problem) of the structure for yaw and pitch rotations. These parameters are the most significant for the phenomenon under study.

The values on the diagram are derived from the equation :

$$\omega_\Theta = \frac{1}{2\pi}\sqrt{\frac{K_\Theta}{I_Y}} \ \ \kappa\alpha\iota \ \ \omega_\Psi = \frac{1}{2\pi}\sqrt{\frac{K_\Psi}{I_Z}}$$

All the diagrams presented in this section have the same format as Figure 5.12. The curve represents the stability boundary, and the points on the curve correspond to marginally stable solutions, while the whirl flutter (WF) phenomenon develops in the interior region of the peculiar segment at the lower-left part. Additionally, we mark the regions where we have static divergence for the system

(v_n=0), which is observed at points on the diagram with low stiffness regarding one of the two degrees of freedom.

From Figure 5.12, it can be observed that as the airspeed increases (with Ω being constant), meaning an increase in the speed ratio (J=V/nD), the whirl flutter stability region increases. To maintain the stability of our system, an increase in structural stiffness is required. Furthermore, it is important to note that the most critical condition arises when $K_\Theta = K_\Psi$, meaning symmetric stiffness in the mounting. This behavior is because we have symmetric stiffness, $\omega_\Theta = \omega_\Psi$, and therefore, the interaction between the two independent motions is maximum.

The fundamental rule to avoid WF, which is clearly evident in this diagram, is to have "large stiffness for stable behavior." Additionally, a construction error in the engine mounting can lead to a significant reduction in stiffness and thus make our system more vulnerable to WF.

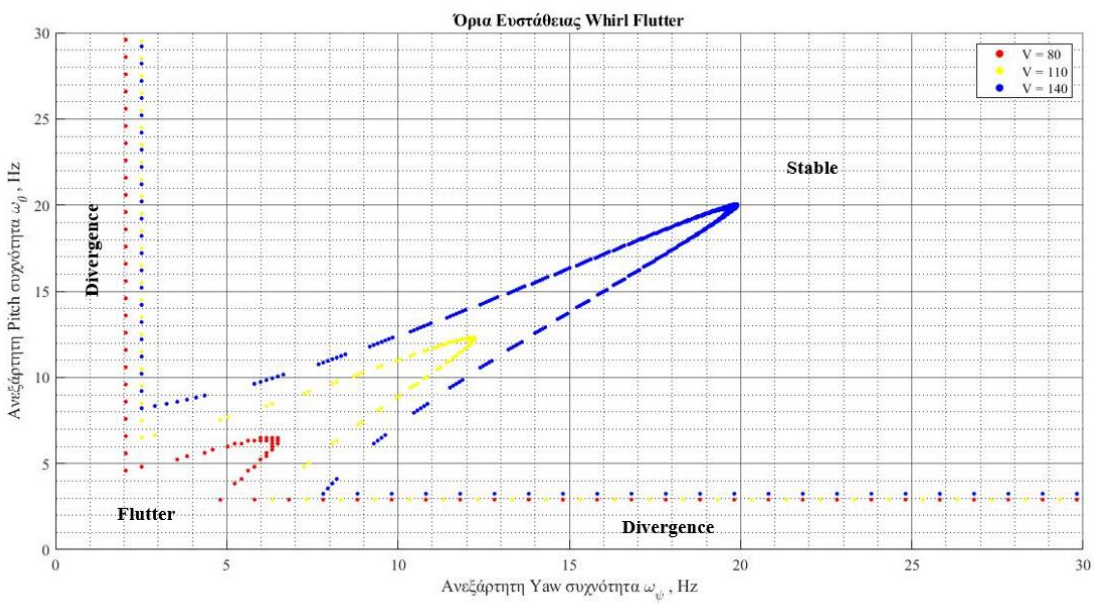

Figure 5. 11. Stability boundaries for different support stiffnesses and for 3 different flight velocities.

In Figure 5.13, the stability boundaries for our system are presented for three different rotational speeds of the propeller, with different stiffness values of the mounting in the two rotational directions. We can observe that the behavior is opposite to the previous figure. As the rotational speed increases, which corresponds to a decrease in J (the non-dimensional rotational inertia), the stability region of the system increases. Additionally, once again, the critical condition is defined for symmetric stiffness. Diagrams like these are crucial during the design of engines and aircraft in the initial stages to correctly and safely determine the operating speed range for the system. During product development, all specifications are based on these values.

In Figure 5.14, we see how the distance of the propeller from the mounting affects the system's stability. It's apparent that the farther the propeller is from the mounting, the larger the values of K_Θ *and* K_Ψ are required for symmetric stiffness. However, for asymmetric stiffness, we can achieve a stable system with a simple adjustment of the parameters without a significant increase. Furthermore, increasing the distance reduces the regions of static deviation. Generally, modern aircraft are designed to eliminate the possibility of static divergence phenomena. The characteristic

and straightforward shape of the static deviation regions observed in the above diagrams allows us to entirely avoid such phenomena.

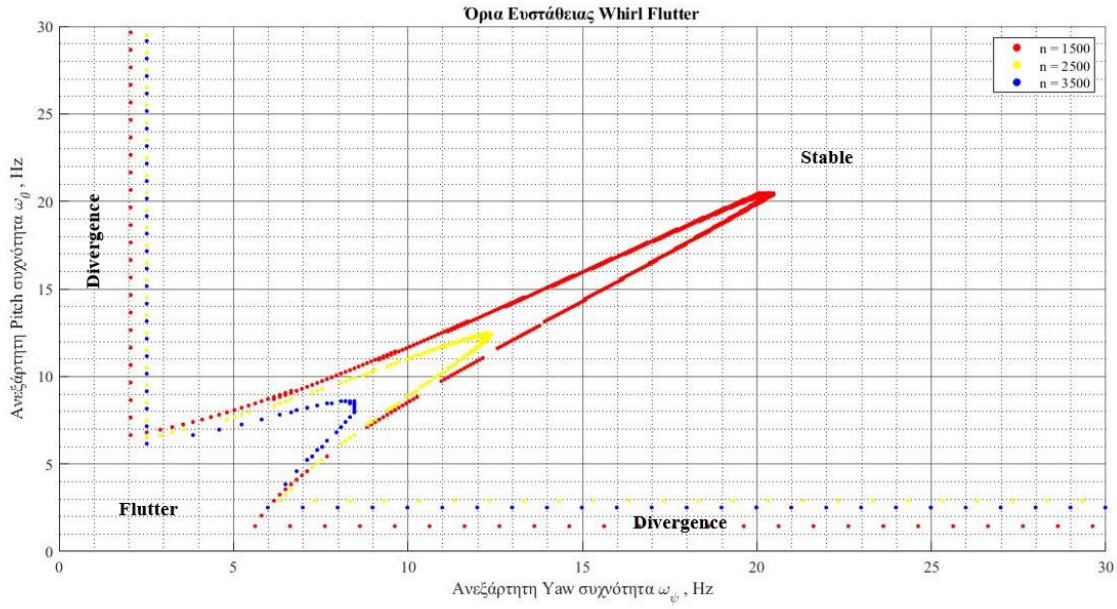

Figure 5. 12. Stability boundaries for different support stiffnesses for 3 different rotational velocities.

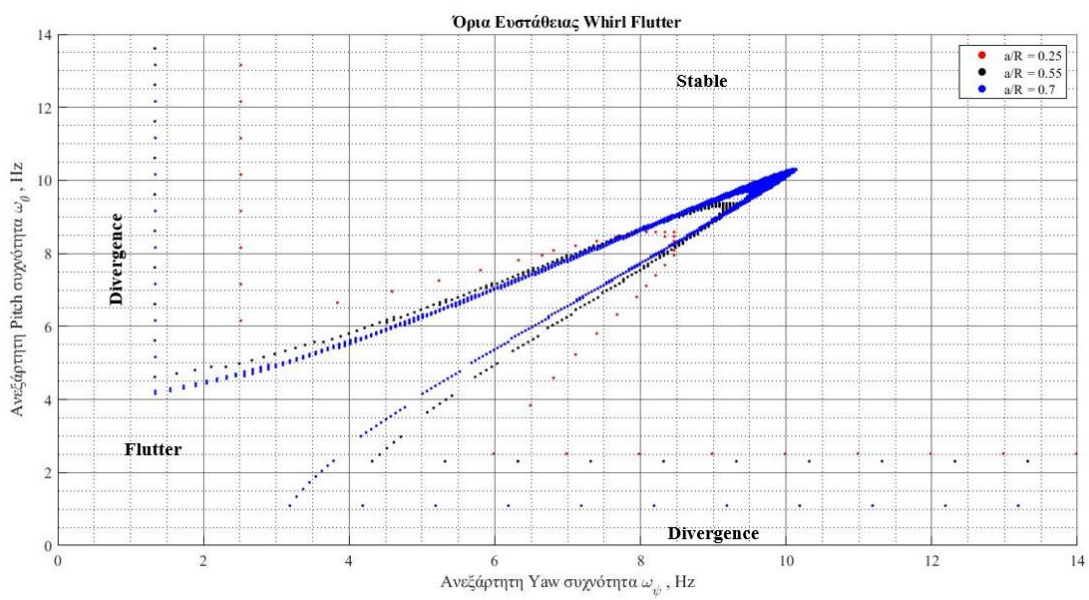

Figure 5. 13. Stability boundaries for different support stiffnesses for 3 different lengths between propeller – support.

In Figure 5.15, we observe the influence of the damping coefficient on the stability boundaries. The diagram is presented in terms of dimensionless frequency for symmetric stiffness about the y-axis as a function of the distance-to-diameter ratio for the propeller. Symmetric stiffness is chosen due to its higher criticality compared to other conditions. For this diagram, we consider symmetric

damping ($C_\Theta = C_\Psi$) in both directions. We can see that structural damping provides larger stability regions in the system for the same reasons a/R.

In Figure 5.16, stability regions are presented for a constant rotational speed of the propeller, assuming symmetric stiffness. We can see that for lower flight speeds, the stability limit is determined by the system's behavior in flutter, while for higher speeds, the critical factor is the static deviation. Diagrams of this form find significant application in engines that use constant-speed propellers.

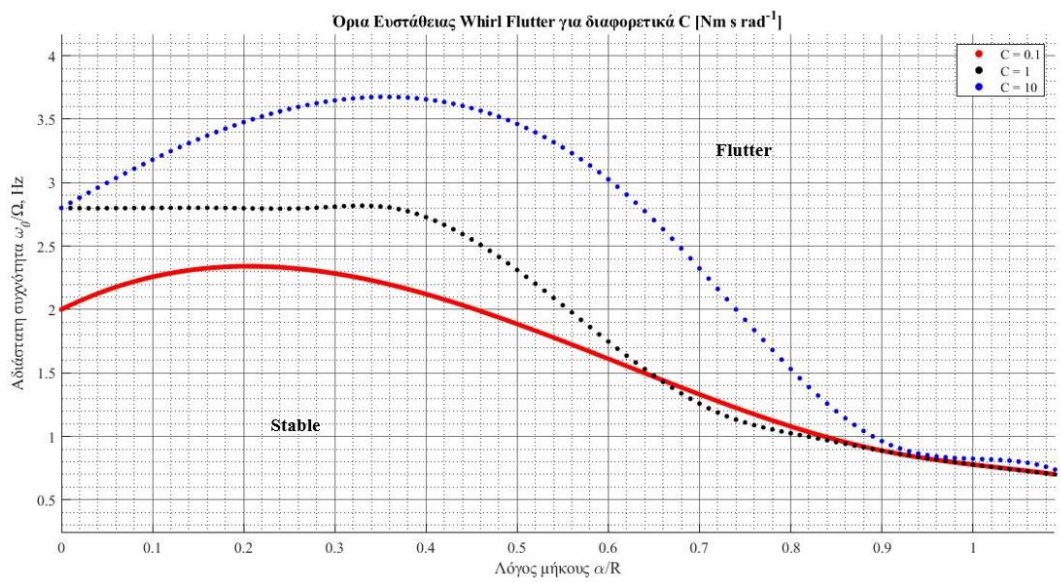

Figure 5. 14. Structural damping impact on the stability boundaries.

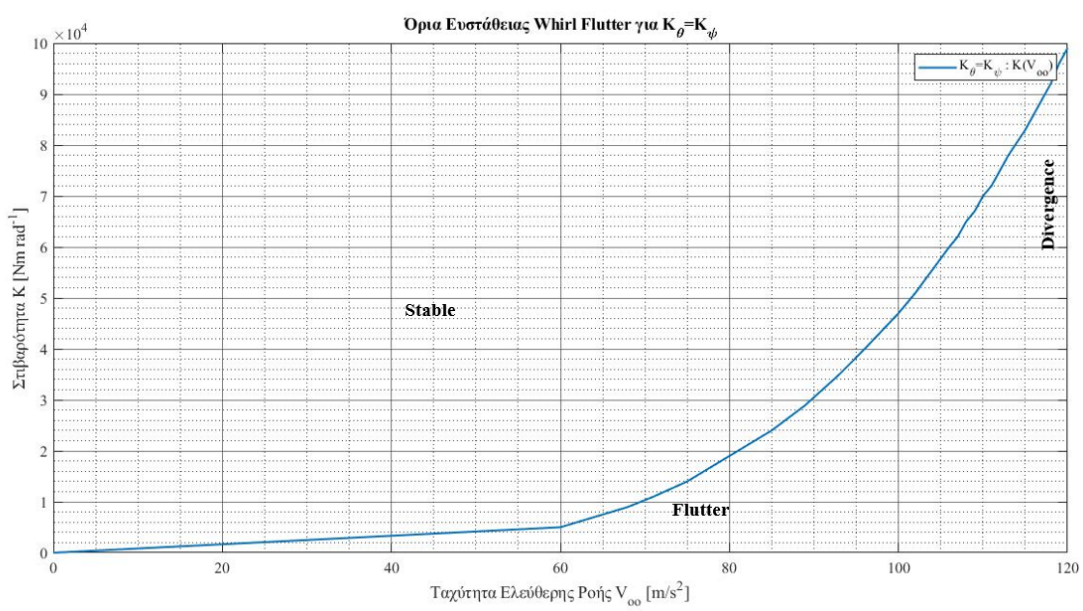

Figure 5. 15. Stability boundaries for $K_\Theta = K_\Psi$ and $\Omega = constant$.

Response

Up to this point, we have observed the behavior of the system for different parameter values. In reality, it is challenging to grasp the significance of these regions without observing the motion in a real structure. As mentioned in the theory, the oscillation ranges of the system in the flutter state are theoretically infinite, and the coupled motions of the forward and backward whirl of the propeller are extremely complex. To provide insight into these concepts and the phenomenon we are studying, we present trajectory response diagrams for the operation of the system in different stability regions.

Specifically, we use parameter values from the stability diagrams 5.12 to 5.16, keeping all system values the same as in Table 5.1 and varying the system's stiffness (choosing ω_Θ and ω_Ψ) to move from one region to another and along the boundary.

The times for which we calculate the response differ from diagram to diagram to clearly highlight the stability characteristics we are investigating. To extract stability behavior, we introduce a disturbance into the system and observe how it propagates. Specifically, we introduce a 5-degree disturbance in the pitch angle. In Figure 5.17, we see the trajectory of the pedestal of the propeller with values for the independent natural frequencies in the stable region.

$$\omega_\Theta = \omega_\Psi = 162.8\, Hz \ , (K_\Theta = K_\Psi = 1050\ [kNm\, rad^{-1}])$$

We observe that initially, the system performs a complex elliptical motion, but over time, the position of the pedestal tends towards the center (0,0). For this reason, the system is characterized as stable. Of greater interest is the trajectory in Figure 5.18, for which our system is marginally stable. The stiffness values for the actuator are chosen on the stability boundary.

$$\omega_\Theta = 10\, Hz\,,\ \ \omega_\Psi = 32.61\, Hz\ , (K_\Theta = 167\ [kNm\, rad^{-1}]\,, K_\Psi = 1050\ [kNm\, rad^{-1}])$$

The motion could be characterized as a rotating elliptical trajectory with variations in the lengths of its sides. We observe that the oscillation amplitudes in both directions are smaller than the initial values of the stable solution. From the theory of marginally stable conditions, we calculate a continuously periodic motion. However, in reality, if this motion is not damped due to structural fatigue, mainly that of the hub (structural imperfections), we may experience a reduction in stability, leading the system to instability.

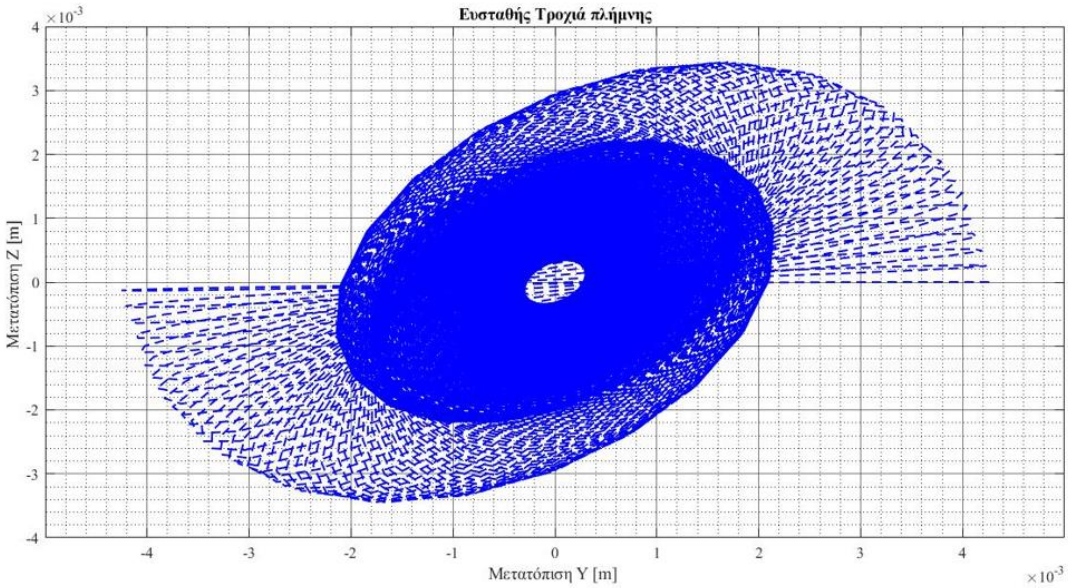

Σχήμα 5. 16. Stable trajectory for the propeller's hub on the rotation plane y-z for $\omega_\Theta = \omega_\Psi = 162.8\ Hz$

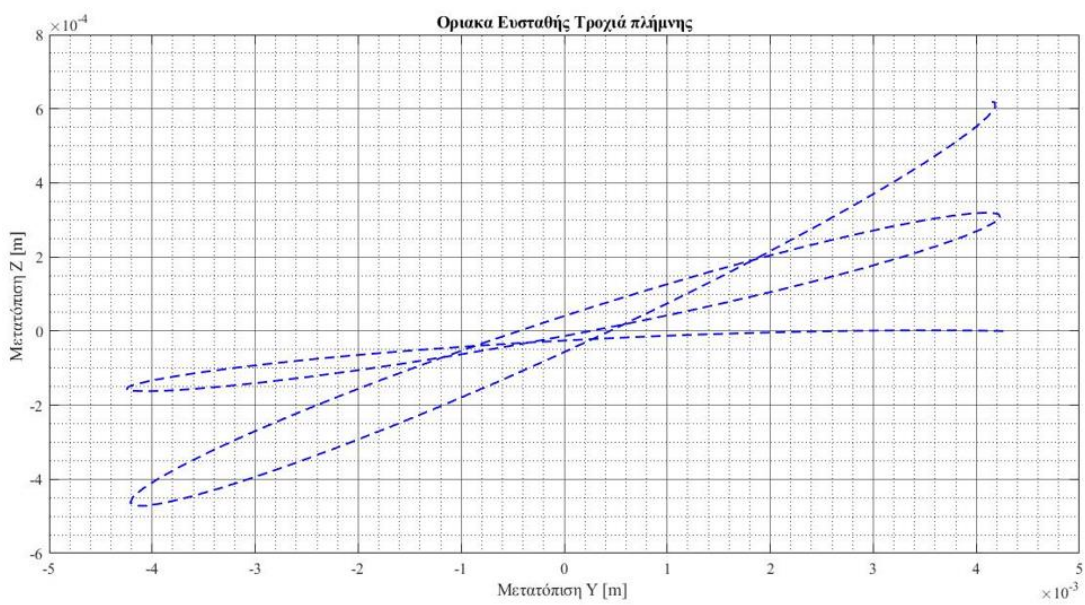

Figure 5. 17 Neutral stable trajectory for the propeller's hub on the rotation plane y-z for $\omega_\Theta = 10\ Hz$, $\omega_\Psi = 32.61\ Hz$

In Figure 5.19, the trajectory of the hub is depicted in a whirl flutter state. The parameters are chosen in the flutter instability region, with values :

$$\omega_\Theta = \omega_\Psi = 32.61\ Hz\ , (K_\Theta = K_\Psi = 42\ [kNm\ rad^{-1}])$$

From the coordinate system depicted in the lower left corner of the diagram, we can discern that the trajectory followed by the propeller is opposite to its rotation (backward). The motion starts from the disturbance position (1) and proceeds to position (2) with rapidly increasing oscillation amplitude. Specifically, this diagram was obtained for a simulation time of t=1 sec. Furthermore, we can see that in such a short time interval, the oscillation amplitudes are an order of magnitude larger than in the previous two states. The trajectory depicted in this figure has the characteristic shape described in the theory.

In Figure 5.20, we observe the trajectory of the hub in a state of static deviation. The stiffness of the action is selected.

$$\omega_\Theta = 96.2\ Hz, \omega_\Psi = 11.25\ Hz\ , (K_\Theta = 365\ [kNm\, rad^{-1}]\ , K_\Psi = 5[kNm\, rad^{-1}])$$

We observe that the oscillation amplitude in the y-direction remains constant during the motion, and the system is dominated by the component in the z-direction (Theta). In the Theta direction, as expected from the theory described, the system moves toward large response ranges without oscillation. The simulation for these two instability charts was conducted for the same time, t=1 sec. We can see that up to this time, the static deviation exhibits smaller ranges. However, due to motion without oscillation, we expect that for longer times, the displacement in the z-direction will be greater compared to whirl flutter.

In summary, in this chapter, we observed that aeroelastic instability phenomena significantly contribute to the integrity of the structure. It is important to be aware of these characteristics during preliminary design so that we can avoid or even harness (FSI - harvesting energy) phenomena with such pronounced behavior. Furthermore, through the charts, we observed the behavior of the system for various parameters and the complex motion it performs for all regions within the stability spectrum.

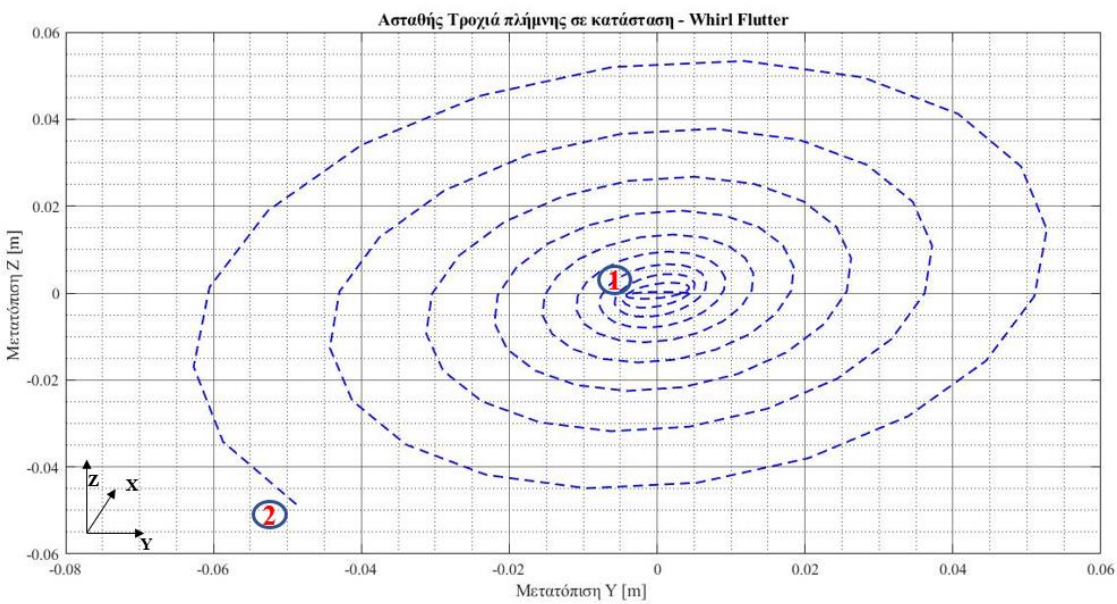

Figure 5. 18. Backward whirl flutter – Unstable trajectory for $\omega_\Theta = \omega_\Psi = 32.61\ Hz$

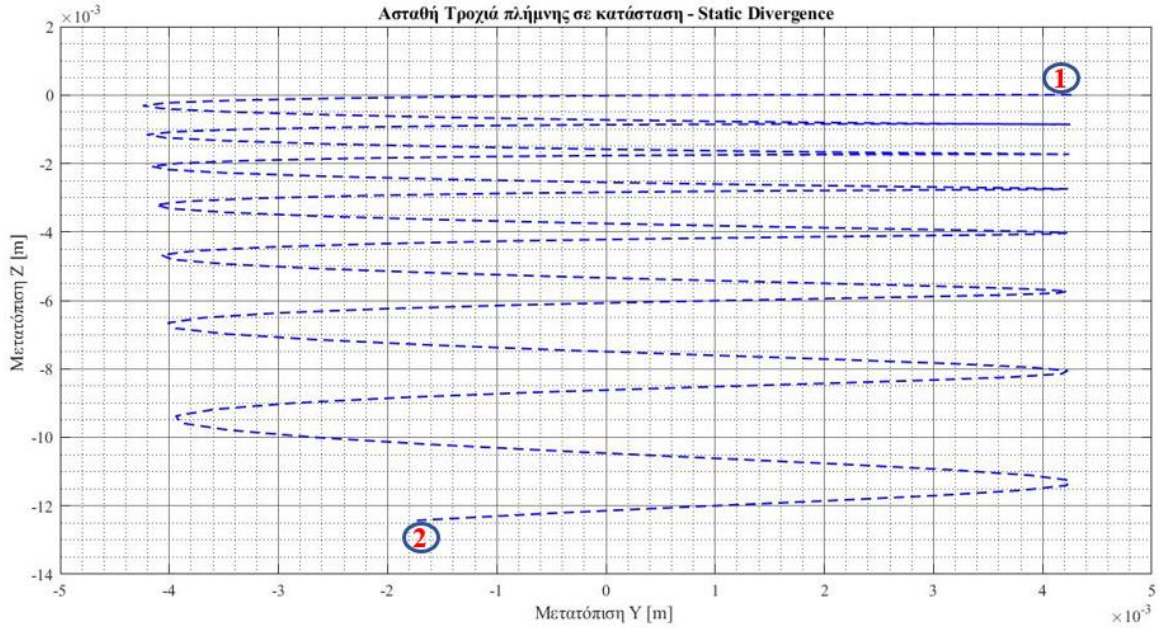

Figure 5. 19. Static Divergence – Unstable trajectory for $\omega_\Theta = 96.2\ Hz, \omega_\Psi = 11.25\ Hz$

6. CONCLUSIONS

In the last chapter of this thesis, we summarize the conclusions we have reached from our analysis of the different models. The most significant result from the analysis so far can be said to be the observation and friction with the various steps of the study, which are required in real-world applications:

$$\boldsymbol{Design \rightarrow Fluid\ Mechanics\ Analysis \rightarrow Dynamic\ Analysis + Stability\ Analysis}$$

"Now, we recognize the importance of each step, the difficulties that may arise, and the critical points that require greater attention. All of the above lead to the definition of a 'comprehensive study,' as presented in the 1st chapter.

Specifically, in the 2nd chapter, we saw that for the proper design of the model, it is initially necessary to define the goals we want to achieve, the design criteria, and the path we will follow. As we observed, both from the results and from the equations we used to interpret them, the geometric characteristics of the propeller play a significant role in the developing loads and the phenomena that occur within it. Furthermore, in this chapter, we emphasized the importance of harmonic components of forces. Harmonic components, as demonstrated in the analyses of chapters 3 and 4, are of great importance for the integrity of the construction and constitute the primary source of errors. It's worth noting that in most large companies, the design phase of a construction project is conducted in parallel with simulations (fluid dynamics and dynamics), with the aim of producing the optimal design with the best characteristics, as well as preventing deviations that could arise if the different stages were conducted sequentially."

In the 3rd chapter, you constructed and solved a three-dimensional fluid dynamics model, considering your propeller as a solid object. From this analysis, you gained insights into the challenges of modeling real-world applications in commercial software. Additionally, you worked with the concept of proper grid discretization. Concerning the grid, you concluded that it's crucial to have a grid that adequately covers the regions of interest while minimizing distortion of its elements.

You also observed the periodically varying behavior of aerodynamic forces and the different pressures developing on the blades under various simulation conditions. The most significant among these forces are the 2P harmonic components, which must be considered in all phases of design and analysis. Another important conclusion drawn from fluid dynamics simulation, although not explicitly presented in the work, is the long solution times. Fluid dynamics problems, due to the large number of elements, complex equations, and the requirement for small time steps, often demand significantly extended solution times. Specifically, for the propeller studied in your work, the average time required for obtaining a solution was approximately 3 hours. Therefore, it's crucial to seek ways to reduce the number of elements or construct the optimal grid discretization because for larger models of real-world applications, the solution times can become prohibitive, as the modern saying goes: "Time is money."

In the 4th chapter, we introduced deformability into the model and solved the aeroelastic problem (FSI - Fluid-Structure Interaction). From the theoretical part of the chapter, we learned about the differences between deformable bodies and solid bodies. Additionally, we presented the most significant static and dynamic aeroelastic phenomena and the mechanisms behind them, with Flutter being the dominant one. By solving the simplified problem of the rotating beam, we

observed additional terms in the stiffness matrix of the equations, which ultimately lead to gyroscopic stiffening. This behavior should be taken into account to avoid operating in resonance regions.

Regarding modeling in commercial software, as in the previous chapter, the importance of proper discretization was evident, aiming to reduce solution times and increase result accuracy. Specifically, for the FSI problem, the average time required was approximately 36 hours. We can see that compared to the fluid dynamics model, the time is approximately 12 times longer, making the goal of reduced solution times even more critical.

By constructing the Campbell diagram, we observed significant variations in the natural frequencies of the structure as a function of rotational speed and identified points where the risk of resonance exists. From the results, we found that our solutions, for all parameter sets, remained periodic for both loads and elastic quantities (displacements, deformations, stresses, etc.). However, these responses exhibited greater complexity. Using Fourier analysis, we saw that this increased complexity is due to the significant differences between the natural frequencies of the two problems (CFD - FSI). Additionally, we observed the aerodynamic damping introduced by the rotating field on the structure and the reduction in vibration ranges due to it. Aerodynamic loads act as periodic excitation forces on the structure, and as we noticed, their removal leads to a permanent static deformation.

From the different parameter sets for which our system was solved, it became apparent that operation around resonance regions, according to the Campbell diagram, leads to larger responses (increased risk of destruction). As a final conclusion regarding the aeroelastic problem of the propeller, we can say that co-simulation, in real-world applications, is necessary either to increase the accuracy of the solution or to observe significant phenomena that would not be apparent in a decoupled study of the subsystems. Of course, when conducting such studies, the required time should be considered in the initial programming.

In the 5th and final chapter, we conducted a parametric study on the stability of the aeroelastic dynamic phenomenon known as Whirl Flutter. Initially, we familiarized ourselves with the phenomenon of whirl flutter, which, in rotating structures with large masses, exhibits complex motions and additional phenomena. Subsequently, by presenting the principles governing Whirl Flutter, we understood the significant implications it can have on our structure due to the deformable action. In this chapter, due to the detailed derivation of equations, we learned about the various difficulties that arise during analytical solving and code development. The most significant challenge in this regard is the proper selection of all model parameters (damping and stiffness coefficients), quantities that are typically determined experimentally in the professional world.

From the results of this chapter, we can generally conclude that greater stability leads to increased safety. Furthermore, the choice of asymmetric characteristics can maintain our structure, even for low stability, within safe operating regions. Additionally, increasing the rotational speed or decreasing flight speed leads to a reduction in stability margins due to increased aerodynamic loads. Stability charts, such as those generated in Chapter 5, are used for selecting characteristics (material, design, etc.) for aircraft propellers to avoid instability and vehicle destruction. The response diagrams presented at the end of this chapter emphasize the importance of different stability and instability conditions.

In summary, for this thesis, we can say that the use of commercial software or programming languages in real-world applications is the only solution. However, for the correct use of these tools

and a proper understanding of the problem, as engineers, we must be familiar with the fundamental physical principles upon which the software relies. Otherwise, inaccuracies in solutions or incorrect approximations could go unnoticed. Furthermore, the interpretation of results requires a good knowledge of the problem and the theory behind it, even though, in practice, we simply utilize the environment of the respective software or programming language.

Additionally, studies like the one conducted in this thesis are essential in today's professional world. Considering that in the past, such analyses were conducted experimentally, it is worth noting that such simulations are cost-effective and provide greater flexibility. They are critical for the safety and improvement of structures, and their applications can extend beyond the field of aeroelasticity to other technological sectors. Specifically, systems like Fluid-Structure Interaction (FSI) are currently advancing, especially in regions lacking access to renewable energy sources. This represents a new and entirely different way of obtaining energy in many countries.

The above may appear quite different from the subject of this thesis, but the principles and modeling procedures involved are based on the same foundations.

BIBLIOGRAPHY

[1] S. Natsiavas, Applied Dynamics, Thessaloniki: ZITI, 1999.

[2] S. Natsiavas, Vibrations of Mechanical Systems, Thessaloniki: ZITI, 2001.

[3] S. Natsiavas, Vibrations of Dynamic Systems with Nonlinear Characteristics, Thessaloniki: ZITI, 2000.

[4] N. Aravas, Mechanics of Materials, Thessaloniki: TZIOLA, 2014.

[5] O.A. Bauchau, Flexible Multibody Dynamics, New York: Springer, 2011.

[6] R. Bielawa, Rotary Wing Structural Dynamics and Aeroelasticity, 2nd edition, Reston, Virginia: American Institute of Aeronautics and Astronautics, 2006.

[7] John D. Anderson, Jr., Fundamentals Of Aerodynamics, 5th edition, New York: McGraw-Hill, 2011.

[8] John D. Anderson, Jr., COMPUTATIONAL FLUID DYNAMICS, New York: McGraw-Hill, 1995.

[9] J. Cercrdle, Whirl Flutter of Turboprop Aircraft Structures, Cambridge: ELSEVIER, 2015.

[10] S. Gudmundsson, General Aviation Aircraft Design: Applied Methods and Procedures, Oxford: ELSEVIER, 2014.

[11] G. Alvin Pierce, Dewey H. Hodges, Introduction to Structural Dynamics and Aeroelasticity, 2nd edition, New York: CAMBRIDGE UNIVERSITY PRESS, 2011.

[12] [L. P. Ruiz-Calavera, D. Perdones-Diaz, "CFD Based Aeroelastic Calculation of Propeller Loads," 28TH INTERNATIONAL CONGRESS OF THE AERONAUTICAL SCIENCES, Airbus Military, Spain, 2012.

[13] Jay E. Turnberg, John A. Violette, W.E. Sullivan, "Large-Scale Advanced Prop-Fan," NASA, Lewis Research Center, 1988.

[14] Yanchu YANG, Zhengyu QU, "Aeroelastic Analysis for the High Altitude Propeller by Using Fluid-Structure Interaction Method," Chinese Academy of Science, Beijing, 2017.

[15] [ANSYS, "Mechanical APDL Theory Guide."

[16] ANSYS, "Fluent 12.0 Theory Guide."